AN INVESTIGATION OF THE STRUCTURAL AND MAGNETIC TRANSITIONS IN Ni-Fe-Ga FERROMAGNETIC SHAPE MEMORY ALLOYS

Todd M. Heil

Dissertation submitted to the faculty of the Virginia Polytechnic Institute and State University in partial fulfillment of the requirements for the degree of

Doctor of Philosophy
In
Materials Science & Engineering

Dr. William Reynolds, Jr., Committee Chair
Dr. Alex Aning
Dr. Sean Corcoran
Dr. Stephen Kampe
Dr. Yu Wang

December 12, 2005
Blacksburg, Virginia

Keywords: Ferromagnetic Shape Memory Alloys, Ferromagnetic Shape Memory Effect, Ni-Fe-Ga, Martensite Transformation, Phase-Field Computational Model

AN INVESTIGATION OF THE STRUCTURAL AND MAGNETIC TRANSITIONS IN Ni-Fe-Ga FERROMAGNETIC SHAPE MEMORY ALLOYS

Todd M. Heil

Abstract

The martensite and magnetic transformations in Ni-Fe-Ga ferromagnetic shape memory alloys are very sensitive to both alloy chemistry and thermal history. A series of Ni-Fe-Ga alloys near the prototype Heusler composition (X_2YZ) were fabricated and homogenized at 1423 K, and a $Ni_{53}Fe_{19}Ga_{28}$ alloy was subsequently annealed at various temperatures below and above the $B2/L2_1$ ordering temperature. Calorimetry and magnetometry were employed to measure the martensite transformation temperatures and Curie temperatures. Compositional variations of only a few atomic percent result in martensite start temperatures and Curie temperatures that differ by about 230 K degrees and 35 K degrees, respectively. Various one-hour anneals of the $Ni_{53}Fe_{19}Ga_{28}$ alloy shift the martensite start temperature and the Curie temperature by almost 70 K degrees. Transmission electron microscopy investigations were conducted on the annealed $Ni_{53}Fe_{19}Ga_{28}$ alloy. The considerable variations in the martensite and magnetic transformations in these alloys are discussed in terms of microstructural differences resulting from alloy chemistry and heat treatments.

The phase-field method has been successfully employed during the past ten years to simulate a wide variety of microstructural evolution in materials. Phase-field computational models describe the microstructure of a material by using a set of field variables whose evolution is governed by thermodynamic functionals and kinetic continuum equations. A two dimensional phase-field model that demonstrates the ferromagnetic shape memory effect in Ni_2MnGa is presented. Free energy functionals are based on the phase-field microelasticity and micromagnetic theories; they account for energy contributions from martensite variant boundaries, elastic strain, applied stress, magnetocrystalline anisotropy, magnetic domain walls, magnetostatic potential, and applied magnetic fields. The time-dependent Ginzburg-Landau and Landau-Lifshitz kinetic continuum equations are employed to track the microstructural and magnetic

responses in ferromagnetic shape memory alloys to applied stress and magnetic fields. The model results show expected microstructural responses to these applied fields and could be potentially utilized to generate quantitative predictions of the ferromagnetic shape memory effect in these alloys.

Acknowledgements

I would like to take this opportunity to acknowledge NASA Langley Research Center for funding this research, as well as the Virginia Space Grant Consortium for granting me a graduate fellowship for the 2003-2004 and 2004-2005 academic years. I have the utmost appreciation for Dr. Bill Reynolds, for not only being an excellent mentor, but also a great friend. Thanks are also due to Bill's wife, Mariko, and daughter, Jenny, for their continued support and friendship over my graduate years.

Thanks, as well, to my advisory committee for their helpful discussions and stimulating classes. Special thanks to Dr. Yu Wang, for without your expertise I would have never gotten the phase-field program running smoothly. To Dave Berry, for infinite help with the equipment in Holden Hall; your skill with wrench is unequalled, and you never fail to impart me with a good chuckle. To my fellow graduate students in the MSE department, especially Oak and Dave, for all the helpful discussions and all the fun that we have shared together.

To Dr. Matt Willard, at the Naval Research Laboratory, for offering tremendous help with magnetic experiments and discussions: I look forward to working closely with you in the near future. For transmission electron microscopy sample preparation and microscope operation, thanks to Steve McCartney at Virginia Tech, Ramasis Goswami at the Naval Research Laboratory, and Vladimir Oleshko at the University of Virginia. Thanks, as well, to Matt Sullivan, Mark Huntington, and Harsh Deep Chopra at SUNY-Buffalo for performing temperature dependent optical microscopy on selected alloys.

Finally, my family is unrivalled in the support and love they have given me over the years, and I truly appreciate having you all. To my father, Bud, my mother, Ann, my brother, Dave, and especially to my wonderful wife, Tara: I couldn't have done this without you, and you all make me a better person, and for that I am grateful.

Table of Contents

List of Figures

List of Tables

Chapter 1 Introduction

This work was first undertaken with the intent to develop ferromagnetic shape memory alloys (FSMAs) for sensing, actuating, and shape morphing applications. A candidate alloy system, Ni-Fe-Ga, was targeted because of a unique combination of properties: a thermoelastic martensitic transformation (a necessary component of the shape memory effect), ferromagnetism, and the ability to introduce a second phase to improve alloy ductility [1]. Upon delving into the project, it became apparent that the phase transformations and magnetic transitions in these specialized alloys are complex and relatively unpredictable. We recognized the opportunity to contribute to a better understanding of the martensitic and magnetic transitions in this relatively fledgling alloy system. In addition to experimental work, a phase-field computer simulation was developed with the intended use as a "virtual" alloy design tool. During the past ten years, many phase-field computational models have been developed and proven to accurately simulate a wide variety of microstructural evolution in materials [2]. However, they are computationally intensive and due to the large lengths of time needed to run the simulations on a personal computer, the crux of the modeling work was revised to simply demonstrate that magnetic and martensitic microstructural evolution can be coupled with such a model.

Chapter 2 is devoted to background material that helps to set a context for that work that was done during this project. Chapters 3 and 4 contain the results of our experimental work on Ni-Fe-Ga FSMAs. Chapter 3 focuses on a series of seven alloys with compositions that have not been explored in the existing literature; their martensitic and magnetic transitions were characterized and correlated to their microstructural features. In particular, the effects of alloy composition, room temperature aging, and high temperature aging on the atomic order in these alloys were explored. Chapter 4 is a focused study of the effects of annealing on the phase transformations and magnetic behavior of a $Ni_{53}Fe_{19}Ga_{28}$ alloy. Chapter 5 shows the results of the phase-field computational model, and the insights it provides on the ferromagnetic shape memory effect in Ni_2MnGa, another widely studied FSMA.

Each chapter is a self contained entity, with an Introduction, Experimental or Model Parameters section, Results and Discussion, Summary or Conclusion, and References section. The work from Chapter 3 will be presented at the Phase Transformations in Magnetic Materials symposium during the 2006 TMS Annual Meeting in San Antonio, Texas (March 12-16, 2006). The symposium proceedings will be published in Metallurgical and Materials Transactions A. The proceedings paper is a collaborative effort with W.T. Reynolds, Jr. (Virginia Tech), M.A. Willard (Naval Research Laboratory), M.R. Sullivan, M.D. Huntington, and H.D. Chopra (State University of New York-Buffalo) as co-authors.

The contents of Chapter 4 were presented during the Displacive Transformations: Shape Memory Alloys symposium at the International Conference on Solid-Solid Phase Transformations in Inorganic Materials 2005 (May 29-June 3, 2005). The corresponding paper has been accepted for publication in the conference proceedings that will become available in January 2006. The co-authors on this paper are the same as those mentioned above for Chapter 3.

Preliminary results of the phase-field modeling work in Chapter 5 were presented during the Computational Thermodynamics and Phase Transformations: Phase Field Models and Related Methods symposium at the 2005 TMS Annual Meeting in San Francisco (February 13-17, 2005). We intend to publish a paper concerning this phase-field model in Applied Physics Letters or Scripta Materialia in 2006. The co-author will be W.T. Reynolds, Jr. from Virginia Tech.

Two appendices are included in this document. Appendix 1 contains the *Mathematica 5.2* [3] code used to run the phase field model, and Appendix 2 contains calorimetry, magnetometry, and optical microscopy results not contained in the body of the document.

[1] K. Oikawa, T. Ota, T. Ohmori, Y. Tanaka, H. Morito, A. Fujita, R. Kainuma, K. Fukamichi and K. Ishida, App. Phys. Lett., **81**, 5201 (2002).

[2] L.Q. Chen, Annu. Rev. Mater. Res., **32**, 113 (2002).

[3] www.wolfram.com

Chapter 2 Background

2.1 Shape Memory Effect

The shape memory effect is a special property possessed by certain metallic alloys that allows them to recover their original shape after a large deformation by way of a reversible martensitic phase transformation. The shape memory effect was first observed in 1951 by Chang and Read in a Au-47.5 at% Cd alloy [1]. Since the discovery of the shape memory effect, a considerable number of shape memory alloys (SMAs) have been developed. The most widely researched, as well as the most prominent SMA currently used in applications, is Ni-Ti (near 50:50 atomic ratio), which was discovered by Buehler et al. in 1963 [2]. Because of their unique properties, SMAs can be utilized as "multi-functional" materials in structural, sensing, and actuating applications.

The shape memory effect is present only in alloys that have a high temperature phase (generally called austenite) that can reversibly and martensitically transform to a low temperature phase. The deformation behavior of a SMA depends on the temperature at which a deformation is introduced.

Suppose a SMA is plastically deformed at a temperature *below* the reversible martensitic transformation temperature (i.e. the alloy is in the martensitic state). If the alloy is subsequently heated above the reversible martensitic transformation temperature, the martensite phase reverts back to the austenite phase, resulting in the recovery of the original shape of the material.

Now suppose a SMA is at a temperature *above* the reversible martensitic transformation temperature (i.e. the alloy is in the austenitic state). An applied stress can induce the formation of the martensite phase, and large nonlinear strains (of up to 18%) can be achieved without causing plastic deformation in the alloy [3]. Once the applied stress is removed, the stress-induced martensite reverts back to the more stable austenite phase, thus recovering the original shape. This behavior is known as superelasticity.

Both the shape memory effect and the superelastic properties of SMAs are currently being utilized in applications that require structural, sensing, and actuating materials [4]. The shape memory effect is well-suited for tube couplings, electrical

connectors, air flow controls for air conditioners, thermostatic mixing valves, robotic limbs, and bone plates. Superelastic applications include headphone headbands, eyeglass frames, reinforcing wire in shoe heels, and orthodontic arch wires.

In 1996, Ullakko, et al. were able to measure a large magnetic field induced strain in a Ni_2MnGa single crystal [5]. Ni_2MnGa is a SMA that is also ferromagnetic; Ni_2MnGa and other SMAs that exhibit both the shape memory effect and ferromagnetism are called ferromagnetic shape memory alloys (FSMAs). They are more promising candidates for actuating and sensing materials than traditional SMAs, since their reversible martensitic phase transformations can be controlled by an applied magnetic field, as well as by applied stress and temperature. Since Ullakko's results were published in 1996, there has been an explosion of research on Ni-Mn-Ga alloys and developmental efforts towards new FSMAs. The FSMAs that have since been developed include Fe-Pd [6], Fe-Pt [7], Ni-Mn-Al [8], Co-Ni-Ga [9, 10], Co-Ni-Al [11], and Ni-Fe-Ga [12].

2.2 Reversible Martensitic Transformation

The martensitic phase transformation is a diffusionless, cooperative shear-like motion of atoms from a (usually) high symmetry phase to a lower symmetry phase [3]. If the structural change from austenite to martensite is reversible, then the martensite is able to revert back to the austenite in its original orientation, thus recovering the original shape. It is this austenite-martensite reversibility that makes the shape memory effect possible.

For a reversible martensitic transformation to occur, these conditions must be satisfied: 1) the driving force for transformation is very small; 2) the interface between the martensite and the austenite is very mobile upon heating and cooling; and 3) the transformation is crystallographically reversible, i.e. the martensite reverts back to the austenite in its original orientation rather than renucleating austenite in different orientations [3]. Martensitic transformations that satisfy these conditions are also known as thermoelastic martensitic transformations.

In alloys with non-reversible martensitic transformations, a large driving force is needed to overcome the plastic strain generated during martensitic transformation or to

move low mobility austenite-martensite interfaces. The interface between the austenite and the martensite is an invariant plane, which means it is undistorted and unrotated. The invariant plane strain can be resolved into two components, a dilatational component and a shear component. Shape memory martensites have a very low dilatational component, so the invariant plane strain can be achieved by a simple shear. It is the low dilatational component in shape memory martensites that results in a relatively low driving force for transformation.

Furthermore, the low symmetry martensite can form multiple correspondence variants, i.e. regions of the martensite that have the same crystal structure but different orientations with respect to the austenite. Particular arrangements of these correspondence variants, which are twin related, allow for the phase transformation strain to be self-accommodating. Self-accommodation of variants creates low localized strain energy and no net deformation in the material.

Crystallographic reversibility in SMAs is achieved by particular conditions of the lattice parameters of the austenite and the martensite, as well as the existence of many mobile twins [13]. The special lattice parameter conditions are 1) lattice parameters that allow many "rank-one connections" between energy wells of the martensite, i.e. there are many possible energy minimizing martensite morphologies; and 2) lattice parameters that allow exact compatibility between the austenite and martensite, eliminating bulk energy stored in the austenite-martensite interface. In addition to the lattice parameter requirements, the existence of many mobile twins avoids slip in the crystal, which would destroy the crystallographic correspondence between the austenite and the martensite. Generally, atomically ordered alloys are good candidates for a thermoelastic martensitic transformation because they have a higher critical stress for slip than in their atomically disordered states.

2.3 Ferromagnetic Shape Memory Effect

Large thermoelastic strains can be generated in certain alloys that are ferromagnetic and exhibit the shape memory effect by the application of a magnetic field. An applied magnetic field is not only an additional means to control the shape memory effect, but is also attractive because it is a much faster method of actuation than heating

and cooling a SMA. The ferromagnetic shape memory effect is possible because of particular properties of the ferromagnetic martensite phase in FSMAs.

To be a useful FSMA, the martensite phase must have a high uniaxial magnetocrystalline anisotropy. Magnetocrystalline anisotropy simply means that the magnetic properties of a crystal are dependent on the direction in which they are measured [14]. In Ni_2MnGa, for instance, the martensite phase has a tetragonal crystal structure, which undergoes a c-axis contraction and an a-axis and b-axis expansion when transforming from the cubic austenite phase [5]. The magnetic easy axis, the direction along which the magnetization tends to align, is the c-axis of the martensite. The microstructure of the martensite in Ni_2MnGa consists of many variants that have their c-axes oriented in different directions. The magnetocrystalline anisotropy causes the magnetization vector of each variant to prefer to be aligned with its c-axis.

When a magnetic field is applied to a crystal in a direction that is different from its easy magnetic axis, the magnetization direction can be rotated to align with the direction of the applied magnetic field. However, the energy required to rotate the magnetization against the anisotropy force is relatively high, and it can characterized by the magnetocrystalline anisotropy constant, K, which is a material-specific constant that describes the strength of its magnetic anisotropy. The applied magnetic field also produces a driving force for twin boundary motion, called the Zeeman energy difference, across the twin boundaries [15]. The Zeeman energy difference creates a pressure on the twin boundaries, and since their mobility in FSMAs is very high, the energy required to move them is lower than the magnetocrystalline anisotropy energy associated with rotating the magnetization vector within a martensite variant. As a result, twin boundaries can move through the material to increase the volume fraction of the favorably oriented martensite variants and decrease the volume fraction of the unfavorably oriented variants, which lowers the total energy of the system.

An interesting and advantageous result of this variant rearrangement is that a macroscopic strain can be induced in a FSMA by applying a magnetic field. Since the low symmetry martensite phase has lattice constants that differ along the a-, b-, and c-axes, when one particular variant is favored over the others, the self-accommodation strain is eliminated, and there is a net deformation in the FSMA. If the applied magnetic

field is reversed, the twin boundaries can move back to their original positions, recovering the magnetic field induced strain. In this manner, FSMAs can be utilized as actuating or shape morphing materials while in the martensitic state.

The ferromagnetic shape memory effect can also be utilized in a way that is analogous to superelasticity in traditional SMAs. The superelastic effect occurs when a SMA that is in the austenitic state is stressed, resulting in the formation of a metastable martensite phase. The martensite forms because the applied stress lowers its total energy, which stabilizes the martensite even though the temperature is above the unstressed martensite-austenite transformation temperature. Analogous to stress-induced martensite, an applied magnetic field can also induce the formation of martensite. If a FSMA is in the austenitic state and an applied magnetic field lowers the total energy of the martensite, a metastable martensite can form. The next section contains a thermodynamic assessment of stress-induced and magnetic field-induced martensite transformations, reported by Jeong, et al [16].

2.4 Thermodynamic Description

The Gibbs free energy change as a function of temperature that occurs during an austenite-to-martensite phase transformation can be expressed in the following form:

$$\Delta G(T)_{total} = \Delta G(T)_{ch} + \left\{\Delta G_{el} + \Delta E_{fr}\right\} \tag{2.1}$$

where $\Delta G(T)_{total}$ is the total Gibbs free energy change per unit volume for an austenite-to-martensite phase transformation, $\Delta G(T)_{ch}$ is the chemical energy change per unit volume associated with the transformation. ΔG_{el} is the elastic strain energy per unit volume generated during the transformation, and ΔE_{fr} is the frictional energy per unit volume dissipated by moving the austenite-martensite interface during the martensite growth. The chemical free energy change is a negative quantity, while the elastic energy and the frictional energy are both positive quantities. This expression shows that the elastic and frictional free energies resist the transformation to martensite. In SMAs, though, the elastic energy of transformation is small, and the austenite-martensite

interface is very mobile, so the frictional energy is also small. As a result, the total chemical driving force (which is a function of temperature) is not required to be large, so a relatively small undercooling is needed to drive the martensite transformation. This is a characteristic of a thermoelastic martensitic transformation.

If a stress is applied to a SMA, it adds an additional term to the change in Gibbs free energy expression, making it a function of both temperature and applied stress:

$$\Delta G(T,\sigma_{app})_{total} = \Delta G(T)_{ch} + \left\{\Delta G_{el} + \Delta E_{fr}\right\} - \int \sigma_{app} d\varepsilon \tag{2.2}$$

where σ_{app} is the applied stress, ε is the resulting strain, and $-\int \sigma_{app} d\varepsilon$ is the elastic strain energy density. Depending on the particular crystallographic relationships between the austenite and the martensite, a hydrostatic compressive stress can either help or hinder the martensitic transformation [3].

Furthermore, an applied magnetic field will also alter the change in Gibbs free energy expression in a FSMA if there is a difference in the saturation magnetization of the martensite and austenite phases. The Gibbs free energy change then becomes a function of temperature, applied stress, and applied magnetic field:

$$\Delta G(T,\sigma_{app},H_{app})_{total} = \Delta G(T)_{ch} + \left\{\Delta G_{el} + \Delta E_{fr}\right\} - \int \sigma_{app} d\varepsilon - \int H_{app} dM_s \tag{2.3}$$

where H_{app} is the applied magnetic field and dM_s is the difference in saturation magnetization between the austenite and the martensite. An applied magnetic field will encourage the formation of martensitic variants that have their easy axes parallel to the applied field, but hinder the formation of variants that have easy axes that are not parallel to the applied field.

It can then be concluded, after examining Equation (2.3), that the temperature at which ΔG_{total} becomes negative can be altered by applying a stress and/or a magnetic field to the FSMA. Application of these fields is one way to harness the ferromagnetic shape memory effect for use in engineering applications.

2.5 Classification of FSMA behavior

There are five temperatures that are needed to adequately describe the transformations that occur in FSMAs. Four of these temperatures describe the reversible martensitic transformation, and the fifth one, the Curie temperature (T_c), is the temperature at which there is a transition from ferromagnetic to paramagnetic behavior.

The reversible martensitic phase transformation in FSMAs does not occur at a single temperature, but rather through a temperature range. As a result, it is necessary to define two temperatures describing each phase transformation. Upon cooling, the martensite start (M_s) and martensite finish (M_f) temperatures define the beginning and end of the martensitic transformation. Similarly, upon heating through the reverse martensite transformation, A_s and A_f temperatures are defined, representing the austenite start and austenite finish temperatures.

In order to classify FSMAs according to their combined martensitic and magnetic behaviors, Oikawa et al. grouped them into three different types [11]. These behaviors are termed Type I, Type II, and Type III. They are defined by the progression of the magnetic and martensitic transitions that occur when cooling from a high temperature to a low temperature. In a Type I FSMA, paramagnetic austenite undergoes a magnetic transition to ferromagnetic austenite, then martensitically transforms to ferromagnetic martensite. For Type II FSMAs, paramagnetic austenite martensitically and magnetically transforms simultaneously to ferromagnetic martensite. Type III FSMAs possess paramagnetic austenite that martensitically transforms to paramagnetic martensite, then undergoes a magnetic transition to ferromagnetic martensite. Figure 2.1 is a schematic phase diagram showing the martensitic and magnetic transitions of each type of FSMA behavior.

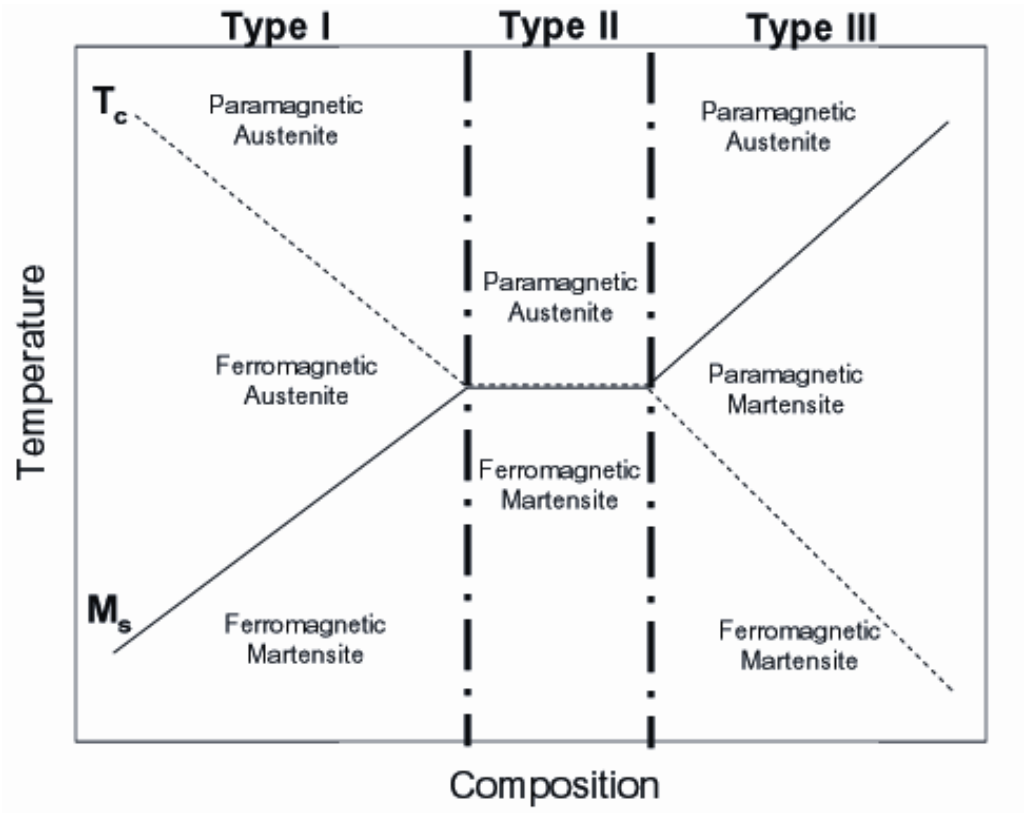

Figure 2.1: Schematic phase diagram illustrating the three types of FSMA behavior

Type II behavior is best suited for strain sensing applications, since a ferromagnetic martensite can be stress-induced from a paramagnetic austenite [11]. The stress-induced martensite has a magnetization that can be measured relative to the paramagnetic austenite. Since the magnetization of the austenite and martensite phase are significantly different, a strain versus magnetization relationship can be devised so that a Type II FSMA can be used as a strain sensor. Ferromagnetic shape memory alloys that show Type I or II behaviors are well suited for actuating and shape morphing applications [16]. As long as the saturation magnetization in the austenite and martensite phases are suitably different (Type II maximizes this difference), an applied magnetic field can induce martensite formation to cause a shape change. Additionally, in Type I FSMAs, the rearrangement of variants in the ferromagnetic martensite due to an applied magnetic field can result in an overall shape change.

2.6 References

[1] L.C. Chang and T.A. Read, Trans AIME, **189**, 47 (1951).

[2] W.J. Buehler, J.W. Gilfrich and R.C. Wiley, J. Appl. Phys., **34,** 1475 (1963).

[3] K. Otsuka and C.M. Wayman, in *Shape Memory Materials* (edited by K. Otsuka and C.M. Wayman) (Cambridge University Press, Cambridge, U.K., 1998).

[4] K.N. Melton, in Shape Memory Materials (edited by K. Otsuka and C.M. Wayman) (Cambridge University Press, Cambridge, U.K., 1998).

[5] K. Ullakko, J.K. Huang, C. Katner, R.C. O'Handley and V.V. Kokorin, Appl. Phys. Lett., **69**, 1966 (1996).

[6] R.D. James and M. Wuttig, Philos. Mag. A, **77**, 1273 (1998).

[7] T. Kakeshita, T. Takeuchi, T. Fukuda, T. Saburi, R. Oshima, S. Muto and K. Kishio, Mater. Trans., JIM, **41**, 882 (2000).

[8] F. Gejima, Y. Sutou, R. Kainuma and K. Ishida, Metall. Mater. Trans. A, **30**, 2721 (1999).

[9] K. Oikawa, T. Ota, F. Gejima, T. Ohmori, R. Kainuma and K. Ishida, Appl. Phys. Lett., **77**, 3054 (2001).

[10] M. Wuttig, J. Li and C. Craciunescu, Scr. Mater., **44**, 2393 (2001).

[11] K. Oikawa, L. Wulff, T. Iijima, F. Gejima, T. Ohmori, A. Fujita, K. Fukamichi, R. Kainuma and K. Ishida, Appl. Phys. Lett., **79**, 3290 (2001).

[12] K. Oikawa, T. Ota, Y. Sutou, T. Ohmori, R. Kainuma and K. Ishida, Mater. Trans., **43**, 2360 (2002).

[13] M. Wuttig, L. Liu, K. Tsuchiya and R.D. James, J. Appl. Phys., **87**, 4707 (2000).

[14] B.D. Cullity, Introduction to Magnetic Materials (Addison-Wesley Publishing Company, Reading, Massachusetts, 1972).

[15] R.C. O'Handley, J. Appl. Phys., **83**, 3263 (1998).

[16] S. Jeong, K. Inoue, S. Inoue, K. Koterazawa, M. Taya and K. Inoue, Mat. Eng. A, **359**, 253 (2003).

Chapter 3 The effects of composition, atomic order, and aging on the martensite and magnetic transformations in Ni-Fe-Ga ferromagnetic shape memory alloys

3.1 Introduction

During the past ten years, studies of Ni-Mn-Ga and other ferromagnetic shape memory alloys (FSMAs) have intensified with the impetus for the development of multifunctional materials. Utilization of the ferromagnetic shape memory effect is envisioned for sensing and actuating applications in aerospace and other fields. While considerable attention has been paid to FSMAs, understanding the wide varieties of structural and magnetic transitions is still a challenge. The intricacies of the phase transformations and magnetic behavior in these alloys need to be uncovered and explained to enable efficient tailoring of FSMA properties for practical applications.

The prominent challenges facing the design and utilization of these specialized alloys are a limited range of operating temperatures, phase transformations that have high sensitivity to variations in composition, brittleness of the alloys, and changes in transformation temperatures due to aging effects.

In 2002, Oikawa et al. published the first results from studies of Ni-Fe-Ga FSMAs [1, 2]. Analogous to Ni-Mn-Ga FSMAs, the ferromagnetic shape memory effect has been demonstrated in Ni-Fe-Ga alloys with compositions near the prototype Heusler stoichiometry (X_2YZ). Ni-Fe-Ga FSMAs have since emerged as promising alloys for sensing and actuating applications because 1) they have the same crystal structures as Ni-Mn-Ga alloys that have shown up to a 9.5% recoverable magnetic field induced strain [3]; 2) they have magnetocrystalline anisotropy constants that are similar in magnitude to Ni-Mn-Ga alloys ($K \sim 1.5 \times 10^5$ J/m^3) [3-5]; 3) at certain compositions they contain a ductile second phase that increases room temperature ductility and facilitates processing [1]; 4) they are easier to fabricate than Mn containing FSMAs because Mn vaporizes at relatively low temperatures; and 5) their elemental metals are more inexpensive than Co containing FSMAs.

The ferromagnetic shape memory effect exists in Ni-Fe-Ga alloys within a relatively small composition range near the Heusler composition, but several different crystal structures have been observed in the austenite and the martensite phases. The austenite is cubic, but has B2 order at temperatures higher than ~973 K [2, 6], while $L2_1$ order is favorable below 973 K. Three different martensite crystal structures have been identified. The first two structures are monoclinic structures (14M and 10M) that have a long period stacking order [6]. These types of complex martensites commonly occur in atomically ordered alloys because the atomic order results in more possible stacking positions of the close packed planes [7]. The 14M and 10M structures have also been seen in Ni-Mn-Al [8], Ni-Mn-Ga [9], and Ni-37at% Al alloys [10]. A tetragonal $L1_0$ martensite has been observed in a $Ni_{54}Fe_{19}Ga_{27}$ single crystal, but only as a stress-induced martensite phase [11]. The appearance and phase fraction of these martensites in Ni-Fe-Ga alloys depends on their composition, processing, and thermal history [6].

The objective of this research was to characterize the magnetic and structural transformations in Ni-Fe-Ga FSMAs with previously unstudied compositions, and to correlate those behaviors to microstructural differences resulting from alloy chemistry and aging effects. Differential scanning calorimetry (DSC), vibrating sample magnetometry (VSM), optical microscopy, and transmission electron microscopy (TEM) were used to characterize the structural and magnetic transformations in this series of alloys.

3.2 Experimental

Seven polycrystalline Ni-Fe-Ga alloys, each weighing 10 g with chemistries near the prototypical Heusler composition (X_2YZ), were made by arc-melting high purity elemental metals (≥99.99%) in an argon atmosphere multiple times. The weight loss after arc-melting was ≤0.4wt% for all alloys. For the worst case scenario, i.e. the alloy with the highest measured weight loss (0.4wt%) with the assumption that the entirety of the weight loss was attributable to Fe, the differences from the nominal composition are Ni = +0.3at%, Fe = -0.4at%, and Ga = +0.1at%. Pieces (weighing approximately 3 g) were cut from each of the as-cast ingots and encapsulated in quartz ampoules filled with an argon atmosphere. The specimens were homogenized at 1423 K for 144000 s to

reduce compositional segregation from solidification in the arc-melting furnace. At the end of the homogenization heat treatment, the quartz ampoules were plunged into iced brine and immediately broken to expose the specimens directly to the quenching medium. Additional isothermal annealing experiments were conducted on one alloy to investigate the sensitivity of the structural transformation temperatures and magnetic Curie temperature (T_c) to aging conditions.

Aging samples were made by cutting small pieces (~3 mm x 3 mm x 1 mm) from the as-cast ingot and homogenizing in the same manner as explained above. After homogenization, the specimens were again encapsulated in separate quartz ampoules for 3600 s isothermal annealing treatments at T_{anneal} = 473 K, 573 K, 673 K, 773 K, 873 K, 973 K, and 1073 K. At the conclusion of their annealing treatments, all specimens were quenched in iced brine and immediately exposed to the quenching medium by breaking the quartz ampoules.

Differential scanning calorimetry was done with a Perkin Elmer Pyris-1 thermal analyzer in cryogenic mode for low temperature measurements and a Perkin Elmer DSC-7 thermal analyzer for high temperature measurements. An ADE Model 4 HF vibrating sample magnetometer was used for thermomagnetization measurements. *In situ* temperature dependent optical microscopy using a Nomarski interferometer, and interference-contrast-colloidal magnetic imaging was conducted using a commercially available heating and cooling stage as described in detail elsewhere [12]. Specimens for TEM were prepared by manually grinding small pieces to about 20 μm thick, gluing the pieces to a copper grid, and ion milling to electron transparency. Transmission electron microscopy experiments were done on a Phillips CM30 operating at 300 kV, and a JEOL JEM-2000FX II operating at 200 kV.

3.3 Results and Discussion

Table 3.1 shows the martensite transformation temperatures measured with differential scanning calorimetry and Curie temperatures determined with vibrating sample magnetometry for the seven alloys. The exothermic DSC peak associated with martensite formation during cooling is bounded by the martensite start (M_s) temperature and the martensite finish (M_f) temperature. The endothermic peak associated with the

reversion of martensite to austenite during heating is bounded by the austenite start (A_s) temperature and austenite finish (A_f) temperature. These temperatures were established by determining a baseline in the vicinity of each phase transformation peak (during either heating or cooling), calculating the integrated area of the peak, and selecting the temperatures corresponding to 5% and 95% of the total peak area. This procedure for identifying transformation temperatures was employed because the DSC peaks for the alloys were irregular with multiple maxima. This method made it possible to make reliable comparisons among the transformation temperatures of alloys with very different DSC peak shapes. For the $Ni_{52}Fe_{20}Ga_{28}$ specimen, there were two distinct peaks on both heating and cooling separated by about 20 K degrees. The values listed below are for the larger low-temperature peak, which had about an order of magnitude greater peak area than the high-temperature, smaller peak. The Curie temperature was taken to be the temperature of the minimum dM/dT value of the thermomagnetization curve under an applied magnetic field of 500 Oe.

Table 3.1: Alloy compositions, martensite transformation temperatures, and Curie temperatures for alloys characterized in this study. All temperatures are in Kelvin.

Alloy	M_s	M_f	A_s	A_f	T_c
$Ni_{54}Fe_{20}Ga_{26}$	310	290	297	316	295
$Ni_{55}Fe_{19}Ga_{26}$	335	316	326	347	287
$Ni_{56}Fe_{18}Ga_{26}$	375	357	369	384	273
$Ni_{53.5}Fe_{19.5}Ga_{27}$	270	250	255	273	271
$Ni_{52}Fe_{20}Ga_{28}$	142	134	138	148	279
$Ni_{53}Fe_{19}Ga_{28}$	203	190	194	207	281
$Ni_{54}Fe_{18}Ga_{28}$	256	239	245	263	259

3.3.1 Composition Effects on Transformation Temperatures

Figure 3.1a shows the M_s temperature of different Ni-Fe-Ga alloys (including the data from this work as well as data reported by other authors) plotted as a function of electron/atom (e/a) ratio [1, 2, 6, 11, 13-16]. All values were determined using single crystalline or polycrystalline specimens that were homogenized at a temperature above the $B2/L2_1$ ordering temperature and water quenched. In general, as the e/a ratio

increases, the M_s temperature increases. The apparent scatter in the data is consistent with results previously reported for Ni-Mn-Ga FSMAs [17]. If the M_s temperatures, however, are considered in the context of the e/a ratio *and* the Ga concentration, tighter trends emerge (see Figure 3.1b). At fixed Ga concentrations, nearly linear increases in M_s temperature become apparent with increasing e/a ratio. These two trends indicate that both e/a ratio and Ga concentration affect the structural transformation.

First principles electronic structure calculations to determine softening of the c_{11}-c_{12} elastic constant (a predictor of the M_s temperature) in Ni-Mn-Ga FSMAs, indicate the M_s temperature generally increases with increasing e/a ratio [18]. However, when the calculations were performed for a Ni-Mn-Ga alloy with a high Ga concentration, and thus lower e/a ratio compared to stoichiometric Ni_2MnGa, the expected M_s temperature was found to *increase*. This intriguing result was attributed to the intricacies of the electronic density of states configuration, which depends not simply on the e/a ratio, but rather on the particular atomic configuration of the crystal. The experimental data in Figure 3.1b supports these calculations because in the same regions of e/a ratios, compositions with higher Ga concentration have a higher M_s temperature.

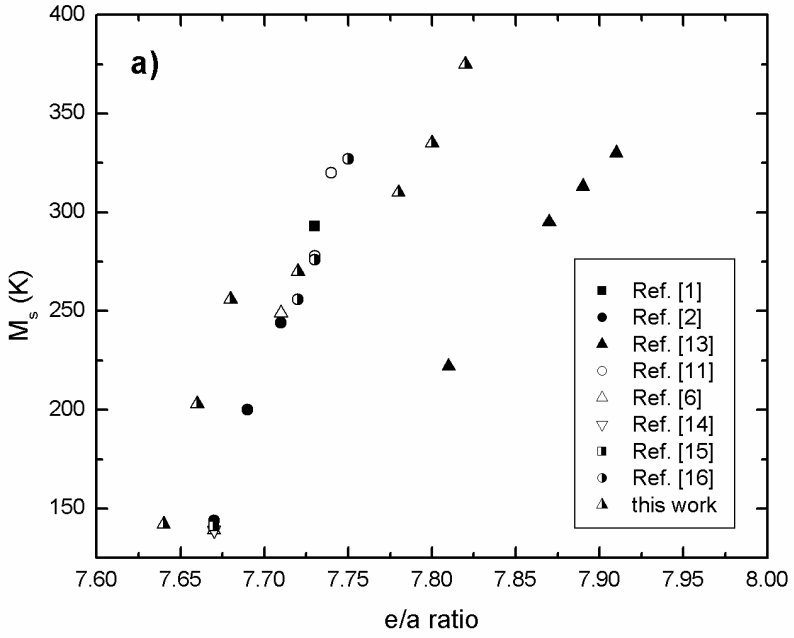

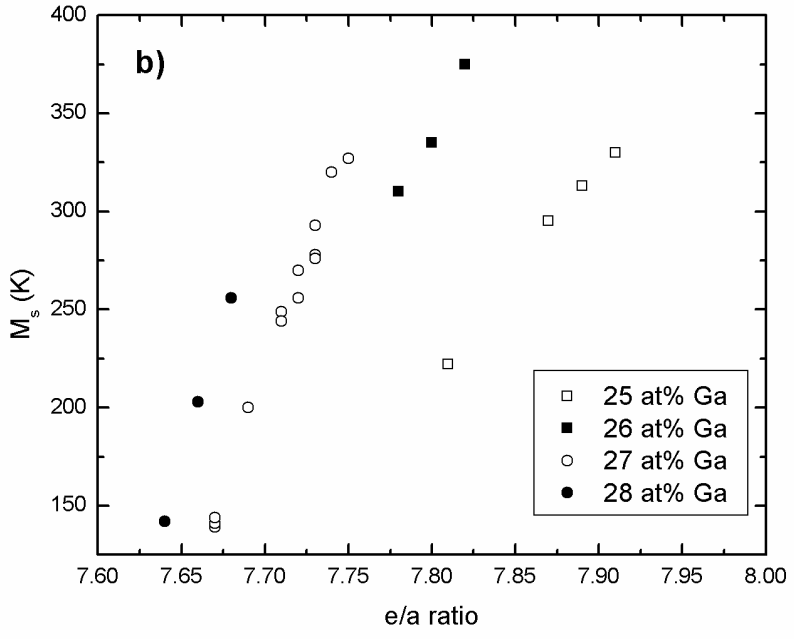

Figure 3.1: Martensite start temperature (M_s) as function of electron/atom (e/a) ratio for (a) Ni-Fe-Ga alloys from this work and those reported in the literature, and (b) the same data with Ga concentrations indicated.

Figure 3.2a shows the variation of the Curie temperature of Ni-Fe-Ga alloys studied in this work and previously reported in the literature as a function of e/a ratio [1, 2, 6, 13-16]. Like the data shown in Figure 3.1, all of these specimens are single crystalline or polycrystalline and homogenized at a temperature higher than the $B2/L2_1$ ordering temperature before quenching in water. The general trend is opposite that of the M_s temperature data, i.e. the T_c decreases with increasing e/a ratio, except for those values reported for a high range of e/a ratios by Li et al. [13]. The T_c for these alloys are considerably higher than those of alloys with low e/a ratios. The substantial difference between the data of Li et al. and other investigators may be attributable to the fact that they used a different experimental technique to determine T_c than those used by the rest of the researchers.

Figure 3.2b replots the T_c data and groups alloys of common Ga concentrations. For constant Ga concentrations, the T_c values decrease with increasing e/a ratio, but the data have more scatter from a linear relationship than the M_s temperature data. There is a general decrease in the T_c with increasing Ga concentration. This effect can be explained by considering that as the Ga concentration is increased, the atomic fraction of the magnetic elements, Ni and Fe, decreases. If the Ga concentration is held constant, an increase in the e/a ratio is achieved by raising the concentration of Ni while simultaneously decreasing the Fe concentration. Chakrabarti et al. have demonstrated by first principles calculations that increasing the Ni concentration in Ni-Mn-Ga FSMAs decreases the difference in total energy between paramagnetic austenite and ferromagnetic austenite, which in turn decreases T_c [19]. The data in Figure 3.2b indicate, to some extent, that the same effect is present in Ni-Fe-Ga alloys.

The scatter in the values in Figure 3.2b may be a result of minor variations from laboratory to laboratory in the quenching procedure and conditions at the end of the homogenization heat treatment. Slower quenching rates allow for a more complete conversion from the B2 order stable at high temperatures to the $L2_1$ order stable at lower temperatures. These factors could include the specimen mass, the quenching medium, and whether or not quartz ampoules were manually broken during the quench.

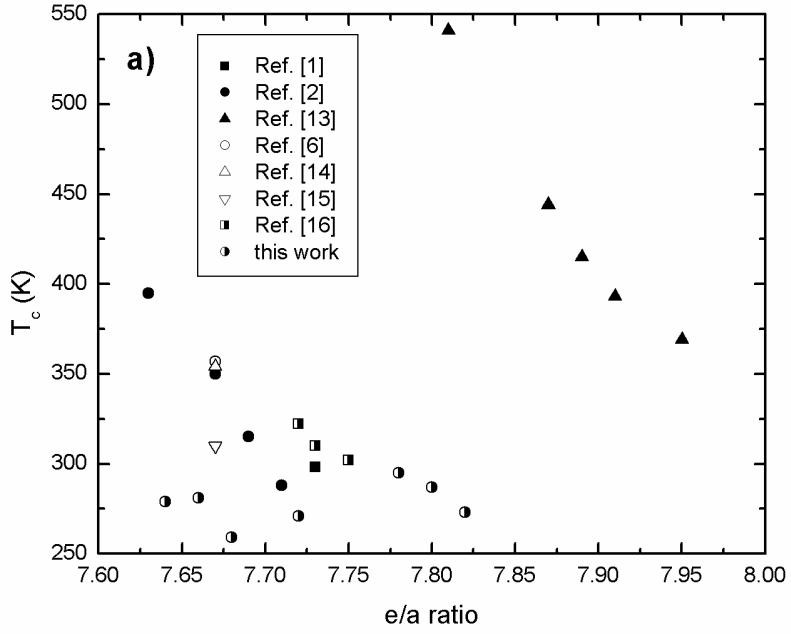

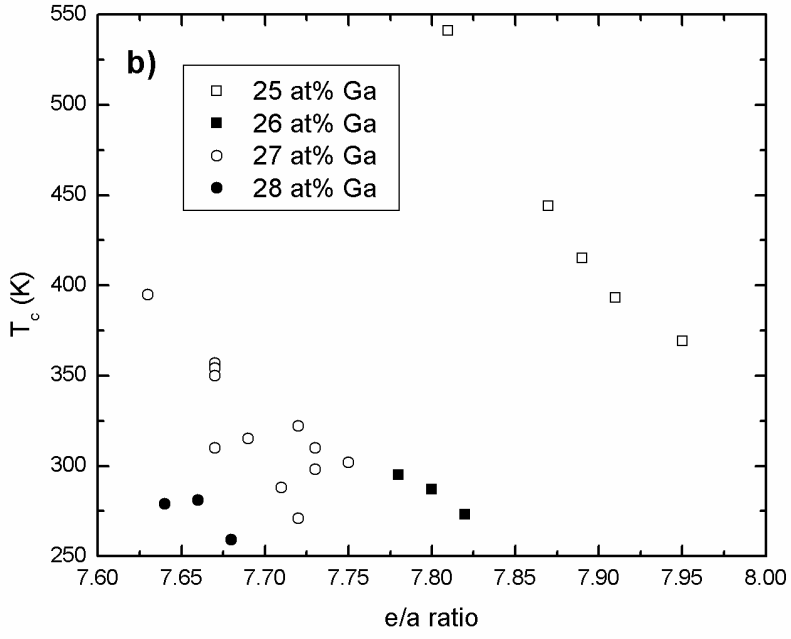

Figure 3.2: Curie temperature (T_c) as a function of electron/atom (e/a) ratio for (a) Ni-Fe-Ga alloys from this work and those reported in the literature, and (b) the same data with Ga concentrations indicated.

3.3.2 Effects of Isothermal Aging

The effects of isothermal aging on T_c of $Ni_{53}Fe_{19}Ga_{28}$ are shown in Figure 3.3. As a point of reference, the T_c of the alloy as-quenched from 1423 K (and stored for several days at room temperature) is 215 K. With higher annealing temperatures, the T_c first rises to 295 K for T_{anneal} = 573 K, then decreases to 219 K at the highest annealing temperature, T_{anneal} = 1073 K. Oikawa, et al. have shown with electron diffraction that the degree of $L2_1$ long-range order in austenite decreases with increasing annealing temperature in a similar alloy [14]. They concluded that the T_c increases with increasing degree of $L2_1$ order. The trend in the T_c data in Figure 3.3 agrees with their observations, except that the T_c of the specimen annealed at T_{anneal} = 473 K is considerably lower than the specimen annealed at T_{anneal} = 573 K. At T_{anneal} = 473 K, it is probable that only partial $L2_1$ ordering occurs during the 3600 s anneal, because of low atomic mobilities at this temperature. Kainuma, et al. have also observed sluggish $L2_1$ atomic ordering at low annealing temperatures in a Ni-Mn-Al FSMA [20]. Partial $L2_1$ ordering at T_{anneal} = 473 K in this $Ni_{53}Fe_{19}Ga_{28}$ alloy is a likely explanation for the low T_c.

The annealing treatment at T_{anneal} = 573 K for $Ni_{53}Fe_{19}Ga_{28}$ results in the maximum T_c in this set of annealing experiments. This annealing temperature and duration increases the T_c by 80 K degrees from the as-quenched state. From a practical standpoint, annealing treatments such as this one could likely be extended to similar FSMAs to increase the maximum operating temperature at which the ferromagnetic shape memory effect can be utilized.

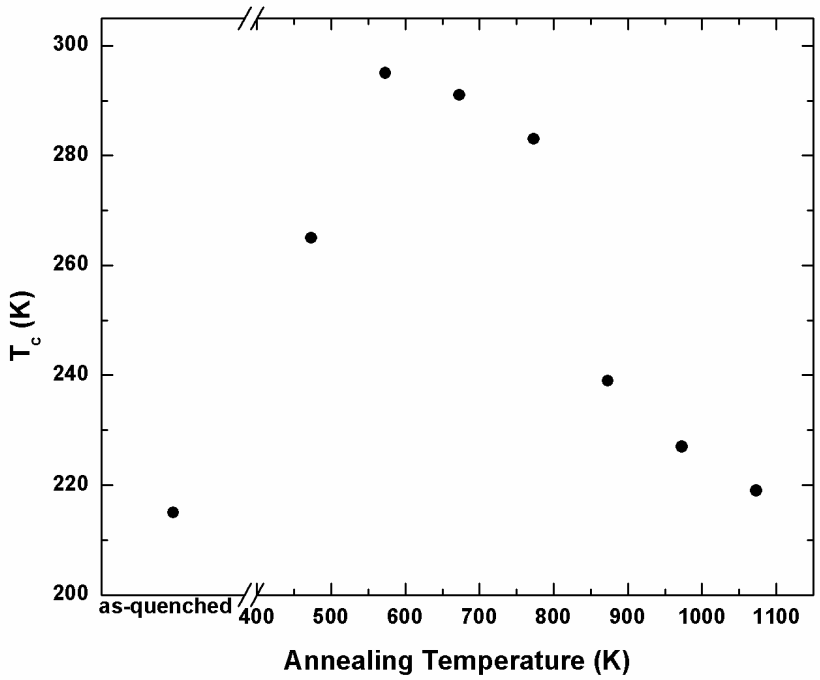

Figure 3.3: The T_c versus T_{anneal} for $Ni_{53}Fe_{19}Ga_{28}$ subjected to annealing treatments for 3600 s.

After annealing the $Ni_{53}Fe_{19}Ga_{28}$ alloy at 573 K for 3600 s (the annealing condition with the highest T_c) it has the cubic $L2_1$ structure. Figure 3.4a is a room temperature diffraction pattern with the electron beam aligned along the [001] zone axis, showing the cubic symmetry of the austenite. The diffuse scattering along the <110> directions suggest that a structural modulation, or premartensitic effect, may be present in the austenite even at a temperature nearly 100 K degrees higher than the M_s temperature. Figure 3.4b is a room temperature diffraction pattern taken along the [-101] zone axis in the austenite, showing {111} diffraction spots, thus indicating that the austenite possesses $L2_1$ order. These diffraction spots show very pronounced streaking along a direction close to (but not exactly along) the <211> directions. This phenomemon has been observed only one other time, to the author's knowledge, in Ni-Fe-Ga FSMAs [21]. The streaking along <211> may associated with the premartensitic phenomenon but it is not well understood at this time.

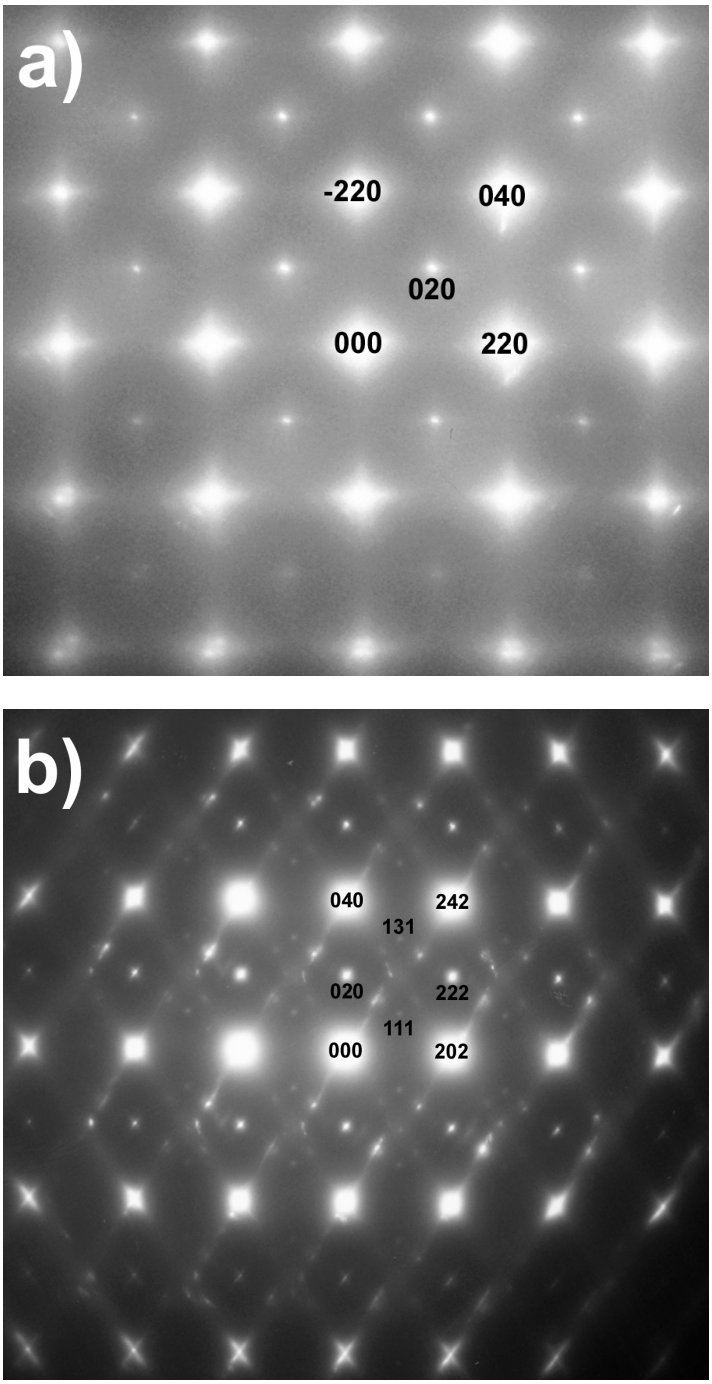

Figure 3.4: Electron diffraction patterns taken at room temperature for $Ni_{53}Fe_{19}Ga_{28}$ annealed at T_{anneal} = 573 K for 3600 s. (a) is along the [100] zone axis and shows streaking along the <110> directions and (b) is along the [-101] zone axis and shows (111) type diffraction spots indicating $L2_1$ order, as well as streaking nearly along the <211> directions.

Figure 3.5 shows an electron diffraction pattern (part a) and the corresponding bright field image (part b), at 140 K, of the $Ni_{53}Fe_{19}Ga_{28}$ alloy annealed at T_{anneal} = 1073 K for 3600 s. The bright field image shows precipitates that formed during the annealing treatment embedded within a martensite matrix. These precipitates were also observed at room temperature. The diffraction pattern is indexed as the [-110] zone of a face-centered cubic crystal. The extra spots on the pattern are from the twinned martensitic structure that is evident in the bright field image. According to work done by Omori, et al. on a similar Ni-Fe-Ga alloy, these precipitates are likely the face centered cubic γ-phase that forms during the higher temperature anneals, but their work only considers anneal at temperatures equal to or higher than 1173 K [6]. They show evidence that the γ-phase draws Ga out of the austenitic matrix, which would, according to Figure 3.2b, tend to increase the T_c of the austenite. Since there is a significant decrease in the T_c from T_{anneal} = 573 K to T_{anneal} = 1073 K, however, it appears that the degree of $L2_1$ order present in the austenite has a greater effect on T_c than small changes in composition resulting from γ-phase formation.

The emergence of the γ-phase during high temperature anneals may have a more prominent effect on the behavior of the M_s temperature with increasing T_{anneal}. Figure 3.6 shows the M_s temperature plotted as a function of annealing temperature for $Ni_{53}Fe_{19}Ga_{28}$. The lowest annealing temperature, T_{anneal} = 473 K, results in a M_s temperature of 178 K. With progressively higher annealing temperatures, the M_s temperature increases to a peak of 237 K at T_{anneal} = 873 K, then decreases up to T_{anneal} = 1073 K. It has been suggested that this trend results from a combination of two effects: the degree of $L2_1$ atomic order and the antiphase domain structure in the austensite [6, 22]. The decrease in M_s temperature at annealing temperatures above T_{anneal} = 873 K has been attributed to the decrease in $L2_1$ order in the vicinity of and higher than the $B2/L2_1$ ordering temperature. Interestingly, the $Ni_{53}Fe_{19}Ga_{28}$ alloy annealed at T_{anneal} = 573 K does not show evidence of the γ-phase, but the high temperature anneal at T_{anneal} = 1073 K results in γ-phase formation. The γ-phase depletes the austenite matrix of Ga, and in accordance with the M_s temperature data in Figure 3.1b, lower Ga concentrations result in lower M_s temperatures. So, for this alloy, the data indicate that the γ-phase may be a

third factor causing the decrease of the M_s temperature at annealing temperatures greater than T_{anneal} = 873 K.

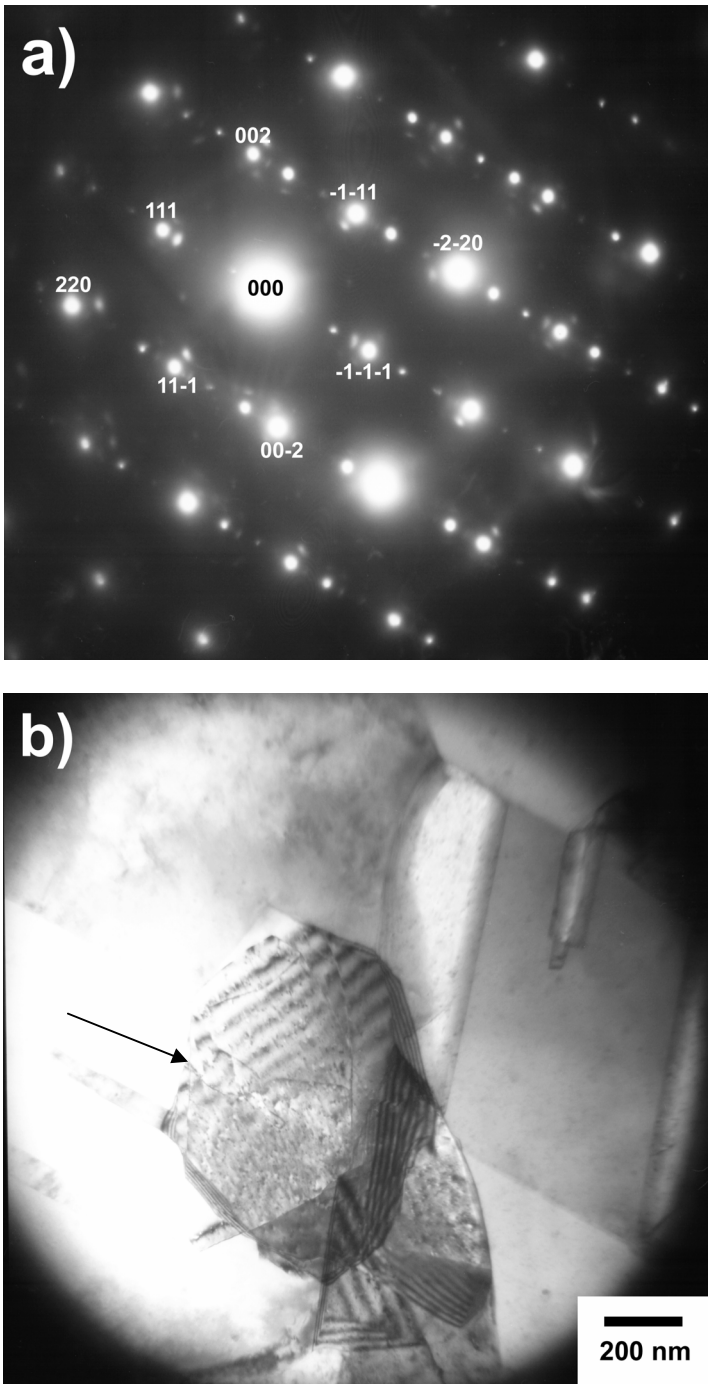

Figure 3.5: For $Ni_{53}Fe_{19}Ga_{28}$ annealed at T_{anneal} = 1073 K for 3600 s, (a) is an electron diffraction pattern taken at 140 K along the [-110] zone axis of the γ-phase and (b) the corresponding bright field image at 140 K showing the martensitic matrix and γ-phase precipitate (denoted by the arrow) that formed during the annealing treatment.

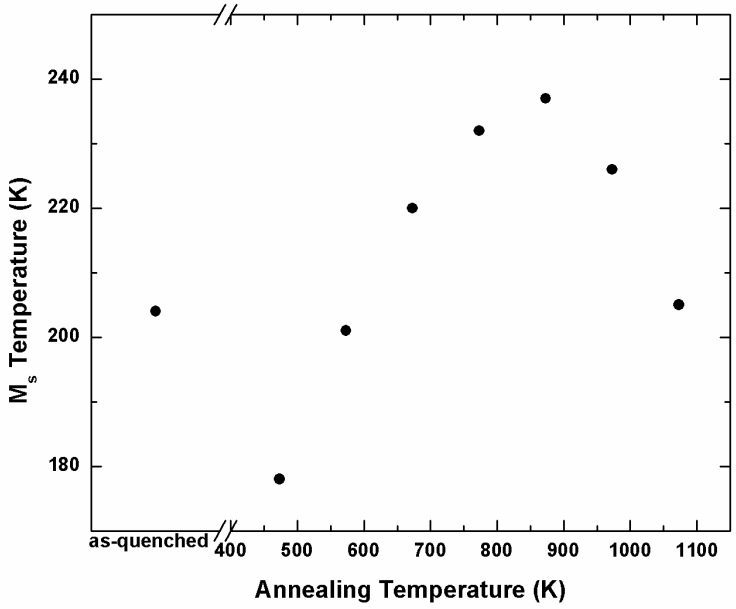

Figure 3.6: M_s temperature as a function of T_{anneal} for $Ni_{53}Fe_{19}Ga_{28}$ alloy.

3.3.3 Room Temperature Aging

Significant room temperature aging effects were observed in $Ni_{53}Fe_{19}Ga_{28}$ and $Ni_{52}Fe_{20}Ga_{28}$ alloys. Figure 3.7 shows calorimetry curves for those alloys shortly after the homogenization treatments and also curves after aging at room temperature for 20 months. The M_s, M_f, A_s and A_f temperatures decreased by ~15 K degrees in both alloys while the calorimetry curves maintained the same shape. The melting temperature (T_{melt}) of the $Ni_{53.5}Fe_{19.5}Ga_{27}$ alloy is 1483 K according to differential thermal analysis measurements. Using the assumption that this value of T_{melt} is the same for the two aged alloys, the ratio of the aging temperature ($T_{RT} \approx 298$ K) to melting temperature is $T_{RT}/T_{melt} \approx 0.2$. Even at this relatively low T_{RT}/T_{melt} ratio, the detectable shift in the martensite transformation temperatures over a long period of time suggests there is sufficient atomic mobility to change the long-range order in the austenite. We suggest that quenched-in B2 phase (austenite) develops some degree of $L2_1$ ordering during

prolonged times at room temperature. The increase in $L2_1$ order over time shifts the martensite transformation to lower temperatures.

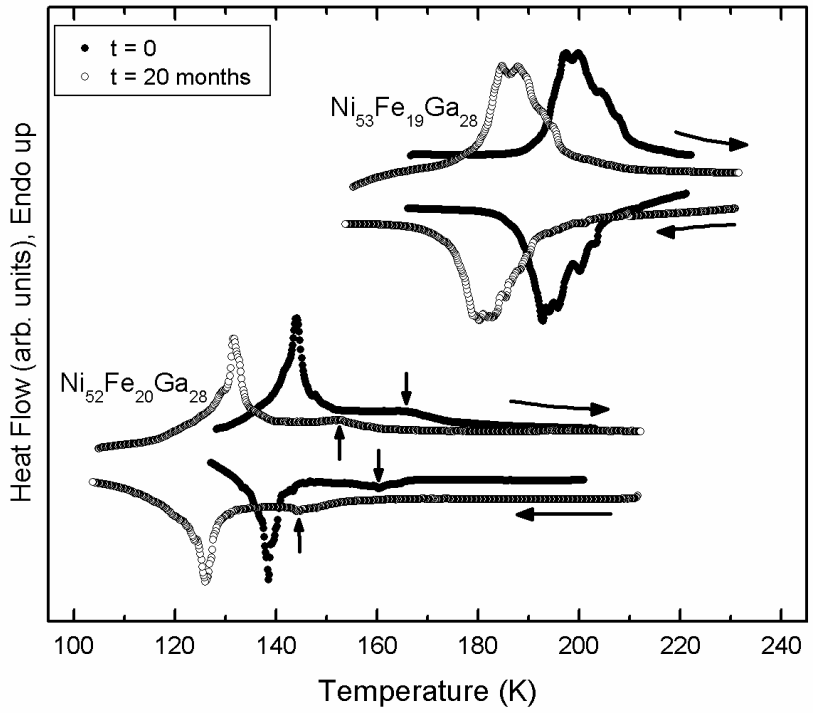

Figure 3.7: Differential scanning calorimetry curves for $Ni_{53}Fe_{19}Ga_{28}$ and $Ni_{52}Fe_{20}Ga_{28}$ before and after aging at room temperature for 20 months. Heating and cooling rates were 0.167 K/s.

3.3.4 Intermartensitic Transformation

Upon close inspection of the calorimetry curves of the $Ni_{52}Fe_{20}Ga_{28}$ alloy, a second peak (indicated by the arrows in Figure 3.7) at a temperature above the prominent martensite peak can be seen on both the heating and cooling curves and for both the un-aged and aged states. The presence of two peaks suggests there is both a martensitic and intermartensitic transformation. The small peaks (about 20 K degrees higher than the large peaks and marked by the vertical arrows in Figure 3.7) appear to correspond to the

martensite transformation. The large peaks likely indicate an intermartensitic transformation to a martensite with a considerably different morphology. Figure 3.8 shows optical micrographs of the aged $Ni_{52}Fe_{20}Ga_{28}$ alloy taken *in situ* during cooling. At high temperature (318.2 K), the sample is in the fully austenitic state. At 130.1 K, a temperature in between the large and small calorimetry peaks, a martensitic microstructure is evident from the appearance of surface relief consisting of fine twins less than 5 μm in width. At 100.9 K, a temperature below the large calorimetry peak, the intermartensitic phase transformation has occurred, resulting in coarse twins greater than 10 μm in width. Both the martensitic and intermartensitic transformations have characteristics of thermoelastic martensitic transformations. Intermartensitic transformations during cooling have been reported to occur in Ni-Mn-Ga FSMAs, but during heating they revert directly to the austenite [23]. In the case of our $Ni_{52}Fe_{20}Ga_{28}$ alloy, the intermartensitic transformation is present on both heating and cooling. Similarly, an intermartensitic transformation on both heating and cooling has been observed in a $Ni_{58}Fe_{17.5}Ga_{27.5}$ alloy [24], but the enthalpy of transformation of the martensite transformation is higher than that of the intermartensitic transformation in their case. More detailed investigations are required to identify the crystal structures of the martensite and proposed intermartensite phases in this alloy.

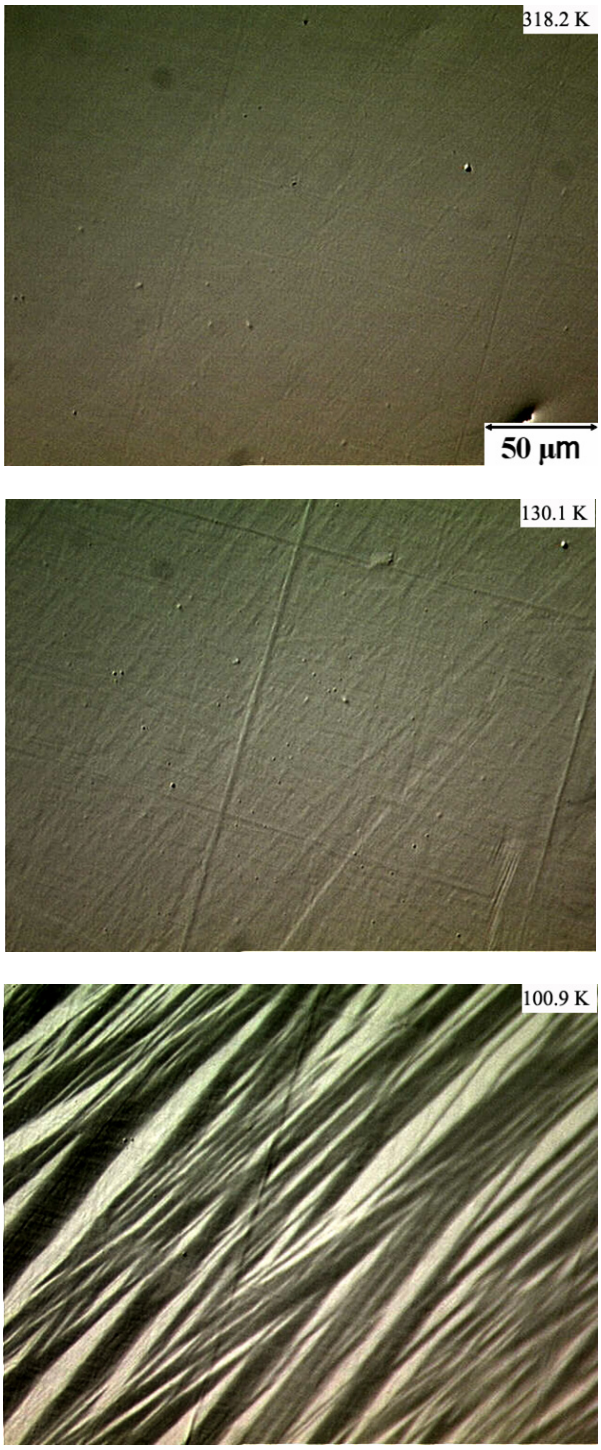

Figure 3.8: Optical micrographs of aged $Ni_{52}Fe_{20}Ga_{28}$ alloy illustrating the progression of phase transformations during cooling: austenite at 318.2 K, high-temperature martensite at 130.1 K, and low-temperature martensite at 100.9 K.

3.3.5 Ordering During Testing

Figure 3.9 shows a series of three heating and cooling cycles (Run 1, Run 2, and Run 3) for $Ni_{56}Fe_{18}Ga_{26}$ and $Ni_{55}Fe_{19}Ga_{26}$. During the first heating of $Ni_{56}Fe_{18}Ga_{26}$ the maximum temperature reached in the calorimeter was 473 K. The A_s temperature is 385 K for the first heating, but on subsequent heatings the A_s temperature drops to 370 K and remains nearly constant, a difference of 15 K degrees. Similarly, during the first heating of $Ni_{55}Fe_{19}Ga_{26}$ the maximum temperature reached in the calorimeter was 573 K. The A_s temperature is 345 K, but on subsequent heatings the A_s temperature drops to 317 K and remains nearly constant, a difference of 28 K degrees. The M_s and M_f temperatures are nearly constant during all three cooling runs for each alloy.

Segui et al. have reported a similar shift in the reverse transformation temperatures after aging Ni-Mn-Ga alloys at elevated temperatures with the alloys in the martensitic state [25]. In these particular experiments, however, the alloys were not subjected to any aging heat treatments before the calorimetry was performed. It is likely, though, that the temperature excursions in the DSC were high enough and for sufficient duration to cause considerable changes in the degree of order in the austenite. The austenite is likely to have changed from B2 to $L2_1$ order, which lowers the martensite transformation temperatures and reverse transformation temperatures. Support of this statement comes from the fact that for the alloy subjected to 573 K, the A_s temperature decreased by 28 K degrees, while the alloy subjected to 473 K only had a A_s temperature decrease of 15 K degrees. Since the alloy raised to 473 K experienced a lower temperature, and also less time at elevated temperatures, lower atomic mobility for a shorter period of time resulted in less $L2_1$ order compared to the alloy heated to 573 K. The sensitivity of these Ni-Fe-Ga alloys to exposure to elevated temperatures suggests that care should be taken in interpreting high temperature calorimetry data for Heusler-type FSMAs, as changes evidently occur in the austenite during sample testing.

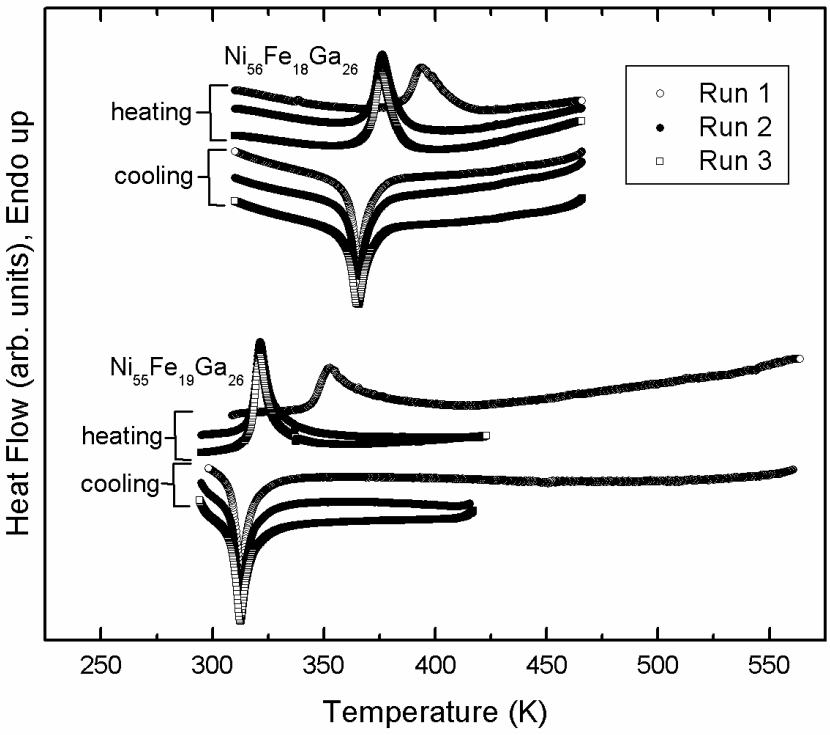

Figure 3.9: Differential scanning calorimetry curves for $Ni_{56}Fe_{18}Ga_{26}$ and $Ni_{55}Fe_{19}Ga_{26}$ alloys showing sensitivity of phase transformations to elevated temperatures. Heating and cooling rates were 0.167 K/s.

3.3.6 Martensite Transformations and Magnetization

Figure 3.10 is a thermomagnetization curve showing the temperature dependence of magnetization in the $Ni_{52}Fe_{20}Ga_{28}$ alloy in an applied magnetic field of 500 Oe. This curve was measured during heating, but the features of the curve are essentially the same when it was measured during cooling.

The arrow labeled (1) in Figure 3.10 is the temperature at which the low temperature martensite transforms to the high temperature martensite. There is a very small depression in the magnetization at this temperature. It has been shown that martensite variants usually contain several plate-like magnetic domains with magnetization directions tied to the magnetic easy directions of each variant, because the

martensite has a high magnetocrystalline anisotropy along a particular crystallographic axis [12]. When an applied magnetic field is absent, the magnetic domains arrange themselves in such a way to avoid the formation of surface or interior poles that would increase the magnetostatic energy, and these arrangements tend to cancel out any net magnetization. It can be rationalized, in this case, that during the structural transformation to the finer scale martensite, the magnetic domains divide and rearrange themselves to satisfy the new, finer scale crystallographic variants in the martensite. At a relatively low applied field of 500 Oe, the magnetic domains can grow or shrink within each variant, since it is easier for the magnetic domain walls to move within a particular variant rather than jump across twin boundaries or result in the ferromagnetic shape memory effect. Since there is only a small depression in the magnetization during the intermartensitic transformation, it seems that the magnetic domains are still able to grow or shrink in both length scales of martensite variants, and that both kinds of martensite have similar saturation magnetizations and hysteretic behavior at low applied magnetic fields.

The second arrow indicates the structural transformation from the high temperature martensite to the austenite. Usually in FSMAs, there is an increase in the magnetization during this transformation, since the disappearance of martensite means there are no longer twin boundaries present to impede the motion of magnetic domain walls [2]. The magnetocrystalline anisotropy constant is lower in the austenite, so it is easier for the magnetic domains to rotate their magnetization directions parallel to the applied field. In this case, however, the magnetization is depressed in the austenite between 200 K and 260 K. At temperatures higher than 260 K, the magnetization decreases as the material approaches the Curie temperature. The magnetization depression in the austenite has been reported elsewhere for Ni-Fe-Ga FSMAs, and has been attributed to pinning of magnetic domain walls at antiphase domain boundaries (APBs) in the austenite [2, 15, 26].

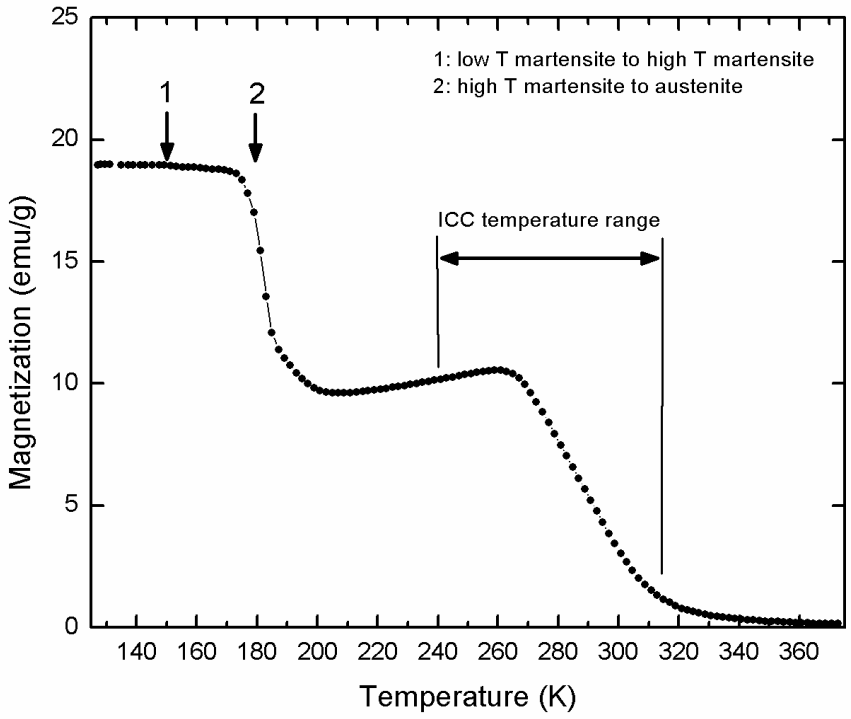

Figure 3.10: Thermomagnetization curve (H=500 Oe) during heating of $Ni_{52}Fe_{20}Ga_{28}$ alloy. Arrows indicate the temperatures at which phase transformations occur.

Using the interference-contrast-colloidal technique (ICC) explained in Reference [12], we show evidence of small circular magnetic domains on the order of 5 μm in diameter contained within much larger magnetic domains (see Figure 3.11). These circular domains exist in the temperature range of the depressed magnetization shown in Figure 3.10, and Figure 3.11 shows the disappearance of the circular magnetic domains during heating of the alloy above the Curie temperature. These magnetic domains have the morphology of surface spike domains, and although spike domains are normally encountered in thick uniaxial crystals, they may form in the cubic austenite of $Ni_{52}Fe_{20}Ga_{28}$ because of surface roughness, surface strain, or inclusions [27]. The circular domains are at a larger length scale than the APBs discussed in the above papers. Between 240 K and 260 K, these domains are well defined and when a low applied magnetic field is applied, they may be magnetized along the crystallographically favorable direction – not necessarily the direction of the applied magnetic field. This

circumstance would yield a lower net magnetization. While a direct correlation between the circular domains and the depressed magnetization region in the thermomagnetization curve for $Ni_{52}Fe_{20}Ga_{28}$ cannot be made at this time, these circular domains could, in addition to pinning of magnetic domain walls at APBs, play a role in the depressed magnetization in the austenite.

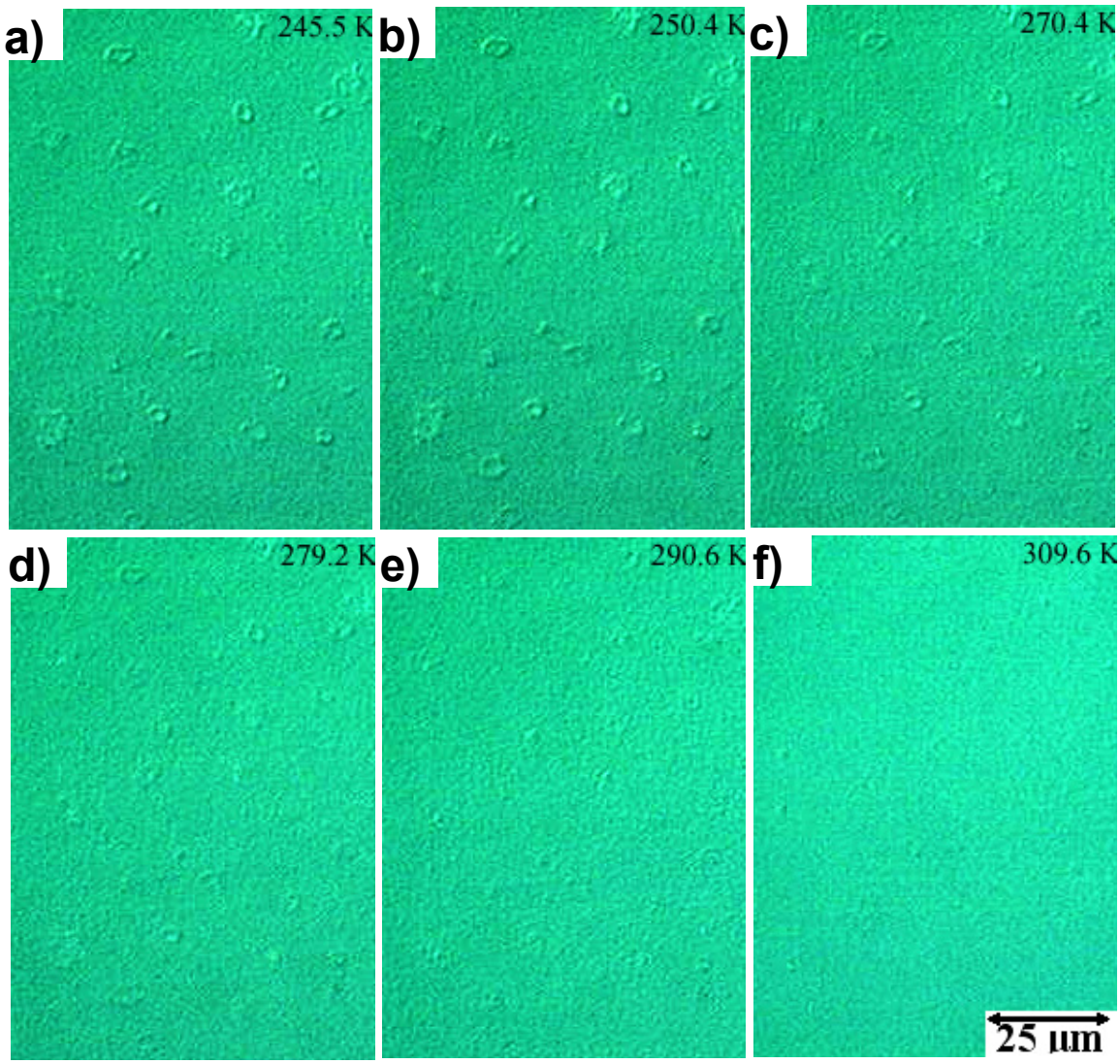

Figure 3.11: Optical micrographs using the ICC technique of aged $Ni_{52}Fe_{20}Ga_{28}$ alloy showing the disappearance of circular magnetic domains during heating.

3.4 Conclusions

The martensite transformation temperatures and Curie temperature of Ni-Fe-Ga FSMAs are sensitive to the e/a ratio, as well as to the particular atomic configuration in the austenite. At fixed Ga concentration, the M_s temperature linearly increases with increasing e/a ratio. In similar e/a ratio regions, alloys with higher Ga concentrations tend to have higher M_s temperatures. The Curie temperature decreases with increasing e/a ratio, and also decreases with increasing Ga concentration. Deviation from Heusler stoichiometry plays a considerable role, in addition to strictly the e/a ratio, in influencing the structural and magnetic transformation temperatures. The conclusions made from first principles calculations on Ni-Mn-Ga alloys appear to extend to Ni-Fe-Ga FSMAs, and are supported by the data presented in this work.

Annealing experiments were conducted on the $Ni_{53}Fe_{19}Ga_{28}$ alloy, and thermomagnetization and TEM show that the Curie temperature is sensitive to the degree of $L2_1$ order in the austenite. As the degree of $L2_1$ order in the austenite increases, the Curie temperature increases. High temperature annealing promotes the formation of the γ-phase in $Ni_{53}Fe_{19}Ga_{28}$, which depletes the austenitic matrix of Ga, and thus further enhances the depression of the M_s temperature at high annealing temperatures.

Results suggest that an intermartensitic transformation was observed in $Ni_{52}Fe_{20}Ga_{28}$ alloy, as evidenced by calorimetry data and *in situ* optical microscopy. It was shown that the martensite transformation causes a large increase in magnetization in a low applied magnetic field, but the magnetization remains nearly unchanged during the intermartensitic transformation. Circular magnetic domains present on the surface of the $Ni_{52}Fe_{20}Ga_{28}$ alloy could possibly play a role in the magnetization depression in the temperature range between the Curie temperature and the martensite transformation.

Room temperature aging for 20 months of $Ni_{52}Fe_{20}Ga_{28}$ and $Ni_{53}Fe_{19}Ga_{28}$ alloys results in the martensite transformation temperatures decreasing by about 15 K degrees. Diffusional processes are still operative at room temperature, and ordering of the austenite to the $L2_1$ structure develops over time. Also, evidence of austenite aging during calorimetry experiments, and a concomitant decrease in martensite transformation

temperatures highlights the complexity involved in interpreting calorimetric results for Ni-Fe-Ga FSMAs.

3.5 References

[1] K. Oikawa, T. Ota, Y. Sutou, T. Ohmori, R. Kainuma and K. Ishida, Mater. Trans., **43**, 2360 (2002).

[2] K. Oikawa, T. Ota, T. Ohmori, Y. Tanaka, H. Morito, A. Fujita, R. Kainuma, K. Fukamichi and K. Ishida, App. Phys. Lett., **81**, 5201 (2002).

[3] A. Sozinov, A.A. Likhachev, N. Lanska and K. Ullakko, Appl. Phys. Lett., **80**, 1746 (2002).

[4] H. Morito, A. Fujita, K. Fukamichi, T. Ota, R. Kainuma, K. Ishida and K. Oikawa, Mat. Trans., **44**, 661 (2003).

[5] H. Morito, A. Fujita, K. Fukamichi, R. Kainuma, K. Ishida and K. Oikawa, Appl. Phys. Lett., **83**, 4993 (2003).

[6] T. Omori, N. Kamiya, Y. Sutou, K. Oikawa, R. Kainuma and K. Ishida, Mat. Sci. Eng. A, **378**, 403 (2004).

[7] K. Otsuka and C.M. Wayman, in *Shape Memory Materials* (edited by K. Otsuka and C.M. Wayman) (Cambridge University Press, Cambridge, U.K., 1998).

[8] R. Kainuma, H. Nakano and K. Ishida, Met. Mat. Trans. A., **27A**, 4153 (1996).

[9] J. Pons, V.A. Chernenko, R. Santamarta and E. Cesari, Acta Mater., **48**, 3027 (2000).

[10] Y. Murakami, K. Otsuka, S. Hanada and S. Watanabe, Mat. Sci. Engr. A, **189**, 191 (1994).

[11] Y. Sutou, N. Kamiya, T. Omori, R. Kainuma, K. Ishida and K. Oikawa, Appl. Phys. Lett., **84**, 1275 (2004).

[12] M.R. Sullivan and H.D. Chopra, Phys. Rev. B, **70**, 094427 (2004).

[13] Y. Li, C. Jiang, T. Liang, Y. Ma and H. Xu, Scr. Mat., **48**, 1255 (2003).

[14] K. Oikawa, T. Omori, R. Kainuma and K. Ishida, J. Magn. Magn. Mater., **272-276**, 2043 (2004).

[15] Y. Murakmi, D. Shindo, K. Oikawa, R. Kainuma, and K. Ishida, Appl. Phys. Lett., **85**, 6170 (2004).

[16] F. Masdeu, J. Pons, C. Segui, E. Cesari, and J. Dutkiewicz, J. Magn. Magn. Mater., **290-291**, 816 (2005).

[17] X. Jin, M. Marioni, D. Bono, S.M. Allen, R.C. O'Handley, and T.Y. Hsu, J. Appl. Phys., **91**, 8222 (2002).

[18] J. MacLaren, J. Appl. Phys., **91**, 7801, (2002).

[19] A. Chakrabarti, C. Biswas, S. Banik, R.S. Dhaka, A.K. Shukla, and S.R. Barman, Phys. Rev. B, **72**, 073103 (2005).

[20] R. Kainuma, F. Gejima, Y. Sutou, I. Ohnuma, and K. Ishida, Mat. Trans. JIM, **41**, 943-949 (2000).

[21] J.Q. Li, Z.H. Liu, H.C. Yu, M. Zhang, Y.Q. Zhou and G.H. Wu, Solid State Commun., **126**, 323 (2003).

[22] T.M. Heil, W.T. Reynolds, Jr., M.A. Willard, M.R. Sullivan, M.D. Huntington, and H.D. Chopra, Proceedings of the International Conference on Solid-Solid Phase Transformations in Inorganic Materials 2005, to be published January 2006.

[23] V.A. Chernenko, V.A. L'vov, J. Pons and E. Cesari, J. Appl. Phys. **93** 2394 (2003).

[24] H.X. Zheng, M.X. Xia, J. Liu, and J.G. Li, J. of Alloys and Compounds, **385** 144 (2004).

[25] C. Segui, E. Cesari, J. Font, J. Muntasell, and V.A. Chernenko, Scr. Mat., **53**, 315 (2005).

[26] Y. Murakami, D. Shindo, K. Oikawa, R. Kainuma, and K. Ishida, App. Phys. Lett., **82**, 3695 (2001).

[27] B.D. Cullity, *Introduction to Magnetic Materials*, (Addison-Wesley Publishing Company, Reading, Massachusetts, 1972).

Chapter 4 Effects of annealing on the martensite and magnetic transformations in a Ni-Fe-Ga ferromagnetic shape memory alloy

4.1 Introduction

Previous studies of ferromagnetic shape memory alloys (FSMAs) in the Ni-Mn-Ga system have shown that martensite transformation temperatures and magnetic transitions are highly sensitive to composition and thermal history [1]. Recently, FSMAs have been developed in the Ni-Fe-Ga ternary system, with alloy chemistries near the prototype Heusler composition (X_2YZ) [2]. Further studies have shown that just as in Ni-Mn-Ga alloys, the martensite transformations and magnetic transitions in Ni-Fe-Ga FSMAs are sensitive to small compositional variations and especially to thermal history [3,4].

In this study, the effects of annealing heat treatments on the martensite transformation in a $Ni_{53}Fe_{19}Ga_{28}$ FSMA were investigated using differential scanning calorimetry and temperature dependent optical microscopy. The magnetic transitions were studied with vibrating sample magnetometry. Understanding the complex microstructural response to thermal history in these FSMAs is of paramount importance towards utilizing annealing heat treatments that tailor martensitic and magnetic transformations for applications involving strain sensing and magnetic actuation.

4.2 Experimental

A polycrystalline $Ni_{53}Fe_{19}Ga_{28}$ alloy was made by arc-melting high purity elemental metals (≥99.99%) in an argon atmosphere multiple times. Small pieces (~3 mm x 3 mm x 1 mm) were cut from the as-cast ingot and encapsulated in a quartz ampoule filled with an argon atmosphere. These specimens were homogenized at 1423 K for 144000 s to reduce compositional segregation from solidification in the arc-melting furnace. At the end of the homogenization heat treatment, the quartz ampoule was

plunged into iced brine and immediately broken to expose the specimens directly to the quenching medium. Specimens were again encapsulated in separate quartz ampoules for 3600 s isothermal annealing treatments at T_{anneal} = 473 K, 573 K, 673 K, 773 K, 873 K, 973 K, and 1073 K. Additionally, specimens were annealed at 573 K for times that ranged from 60 s to 360000 s to investigate time dependent annealing effects. All annealed specimens were quenched in iced brine at the conclusion of their annealing treatments.

Differential scanning calorimetry was done with a Perkin Elmer Pyris-1 thermal analyzer in cryogenic mode. An ADE Model 4 HF vibrating sample magnetometer was used for thermomagnetization and isothermal magnetization (M vs. H) measurements. Temperature dependent optical microscopy was conducted using a commercially available heating and cooling stage with a precision of ±0.1 K, as described in detail elsewhere [5].

4.3 Results and Discussion

The B2/$L2_1$ ordering temperature has been reported as a first order transformation at 973 K for a Ni-Fe-Ga alloy with a composition similar to $Ni_{53}Fe_{19}Ga_{28}$ [4]. These annealing experiments incorporate temperatures both above and below the B2/$L2_1$ ordering temperature. Calorimetry data were collected using heating and cooling rates of 0.167 K/s to reveal the martensite phase transformations. All specimens showed symmetric peaks on heating and cooling with a thermal hysteresis ≤10 K degrees, indicating the presence of a reversible thermoelastic martensite transformation, and thus the shape memory effect. The Curie temperature (T_c) was taken to be the temperature of the minimum dM/dT value of the thermomagnetization curve under an applied magnetic field of 500 Oe. Figure 4.1 shows how martensite start (M_s) temperatures and Curie temperatures depend on annealing temperature.

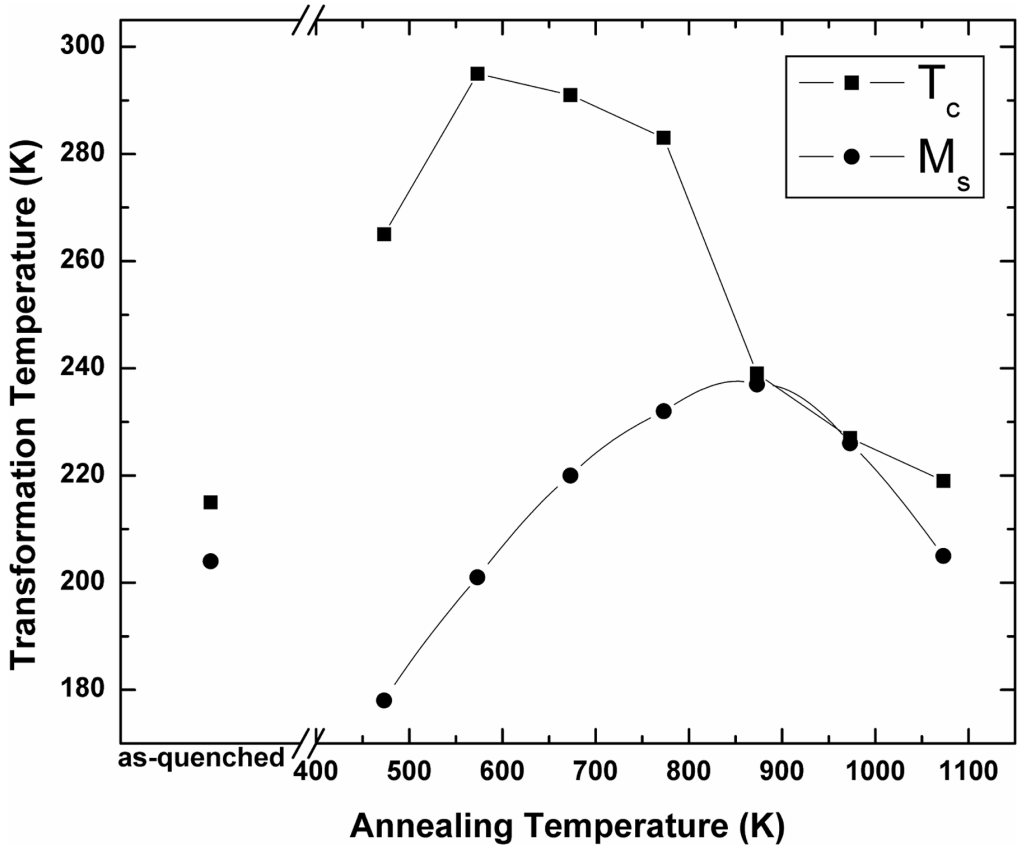

Figure 4.1: T_c and M_s temperatures vs. T_{anneal} for $Ni_{53}Fe_{19}Ga_{28}$ specimens annealed for 3600 s.

These annealing treatments shift the Curie temperature by almost 70 K degrees, from a minimum of 219 K to a maximum of 297 K, for the specimens annealed at T_{anneal} = 1073 K and T_{anneal} = 573 K, respectively. At annealing temperatures higher than T_{anneal} = 573 K, the Curie temperature decreases with increasing annealing temperature. Oikawa, et al. have shown with electron diffraction that the degree of $L2_1$ atomic order in the austenite decreases with increasing annealing temperature in $Ni_{51}Fe_{22}Ga_{27}$ [4]. They concluded that the Curie temperature increases with increasing $L2_1$ order. The trend in the Curie temperature data in Figure 4.1 agrees with their observations, except that the Curie temperature of the specimen annealed at T_{anneal} = 473 K is considerably lower than the specimen annealed at T_{anneal} = 573 K. At T_{anneal} = 473 K, it is probable that only partial $L2_1$ ordering occurs during the 3600 s anneal, due to low atomic diffusivities at this temperature. Kainuma, et. al. have also observed sluggish $L2_1$ atomic ordering at

low annealing temperatures in a Ni-Mn-Al FSMA [6]. Partial $L2_1$ ordering at T_{anneal} = 473 K in our $Ni_{53}Fe_{19}Ga_{28}$ alloy is a likely explanation for the low Curie temperature.

The annealing treatments also shift the martensite start temperature by almost 70 K degrees. The lowest annealing temperature, T_{anneal} = 473 K, results in a M_s temperature of 178 K, the M_s temperature steadily increases to a peak of 237 K at T_{anneal} = 873 K, then decreases up to T_{anneal} = 1073 K. We suggest that this trend results from a combination of two effects: the degree of $L2_1$ atomic order and the antiphase domain structure in the austensite. The increasing M_s temperature at $T_{anneal} < 873$ K may be due to an increase in the antiphase boundary area. $L2_1$ order in the austenite is stable at all temperatures below 973 K, but the antiphase domains are expected to increase in size with increasing T_{anneal}. Antiphase boundaries act as pinning sites for magnetic domain wall motion [7], and Omori, et. al. have suggested that an interplay between the antiphase boundaries and magnetic domains may suppress the M_s temperature [8]. However, further investigations are necessary to clarify the link between antiphase boundaries, magnetic domains, and the martensite transformation. At $T_{anneal} \geq 973$ K, the temperature is at or above the $L2_1$/B2 ordering temperature, so the austenite is expected to predominately have B2 order. The B2 order lowers the M_s temperature relative to the T_{anneal} = 873 K, where $L2_1$ order with large antiphase domains are favored. Figure 4.2 shows a schematic diagram illustrating how the long-range atomic order and antiphase domain structure in the austenite influences the M_s temperature.

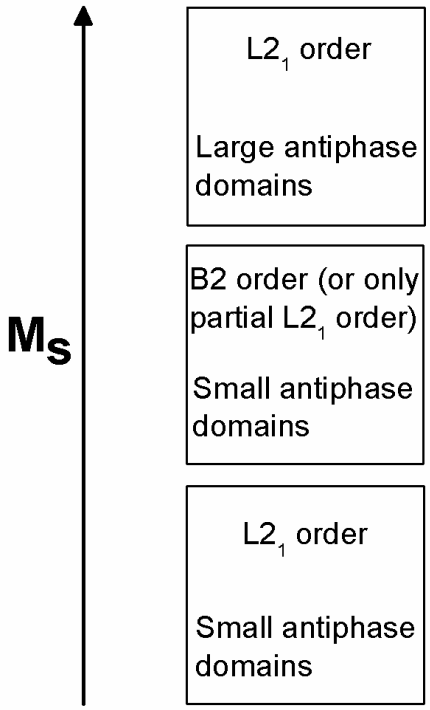

Figure 4.2: Schematic diagram illustrating how microstructural conditions in the austenite effect the M_s temperature.

To determine the effect of annealing time on the martensite transformation, isothermal annealing treatments at T_{anneal} = 573 K for 60 s, 600 s, 3600 s, 36000 s, and 360000 s were conducted. Figure 4.3 shows the dependence of the M_s temperature on annealing time. Starting with the as-quenched (from 1423 K) condition, the M_s temperature first decreases with increasing time to M_s = 192 K at 600 s, then remains nearly constant at $M_s \approx$ 192 K for 3600 s and 36000 s. However, for the 360000 s annealing time, the M_s temperature increases to M_s = 207 K. This behavior can be explained as follows: with increasing annealing time up to 36000 s, the austenite orders from B2 to $L2_1$ (since T_{anneal} = 573 K is below the B2/$L2_1$ ordering temperature) but maintains a small antiphase domain structure. Longer annealing times allow the antiphase domains to coarsen. Using a similar rationale as outlined above, i.e. antiphase

domains coarsen with increasing T_{anneal}, the coarsening of antiphase domains with increasing time at T_{anneal} = 573 K also raises the M_s temperature.

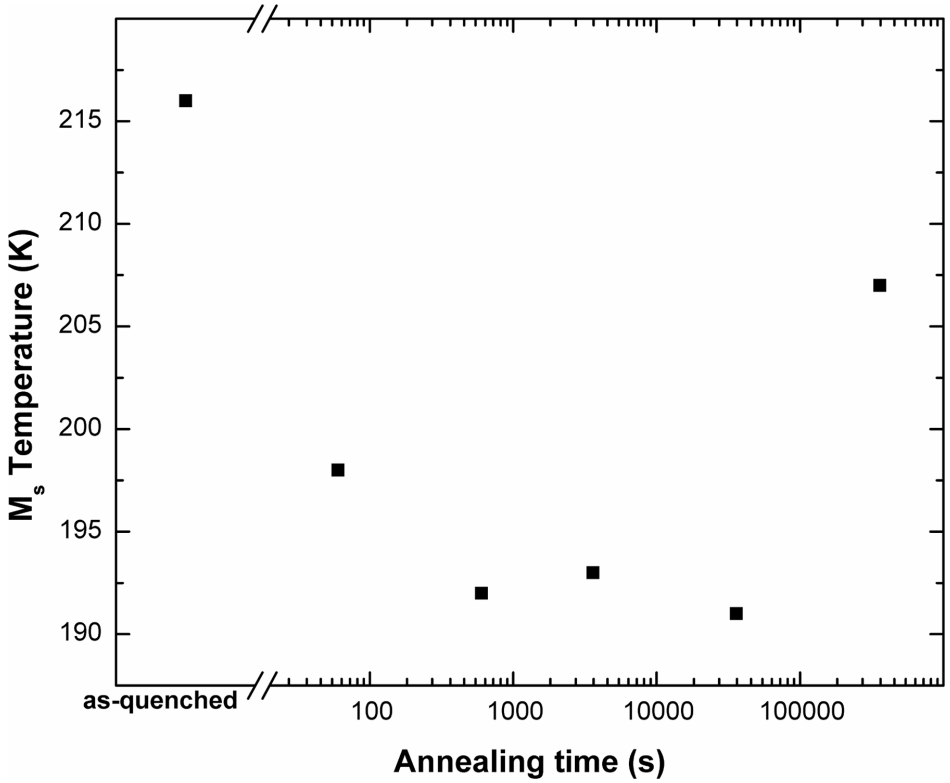

Figure 4.3: M_s temperature vs. annealing time for $Ni_{53}Fe_{19}Ga_{28}$ alloy annealed at 573 K.

Figure 4.4a and Figure 4.4b show thermomagnetization curves (H=500 Oe) during cooling for the specimen annealed at 573 K for 3600 s, and during heating and cooling for the specimen annealed at 1073 K for 3600 s, respectively. The specimen annealed at 1073 K (see Figure 4.4b) shows typical ferromagnetic behavior, i.e. it is paramagnetic at high temperatures, and ferromagnetically orders during cooling below T_c. For the specimen annealed at 573 K (see Figure 4.4a), ferromagnetic ordering begins to occur upon cooling at a temperature about 80 K degrees higher than the specimen annealed at 1073 K, since the austensite annealed at 573 K has $L2_1$ order. However, at about 280 K, the magnetization decreases during further cooling. The inset in Figure 4.4a shows magnetization curves (M vs. H) at 223 K and 278 K, indicating that it is more difficult to saturate the austenite at lower temperatures. Since the antiphase domain size is expected to be small when annealed at T_{anneal} = 573 K, magnetic domain walls should

remain pinned at antiphase boundaries in the austenite at the relatively low applied magnetic field of 500 Oe. The magnetocrystalline anisotropy constant, K, of the austenite in Ni-Fe-Ga alloys increases with decreasing temperature, making saturation more difficult [9]. During cooling, the magnetization vectors rotate away from the applied magnetic field direction and towards the randomly oriented easy axes in the austenite, resulting in a decrease in the overall magnetization in the material.

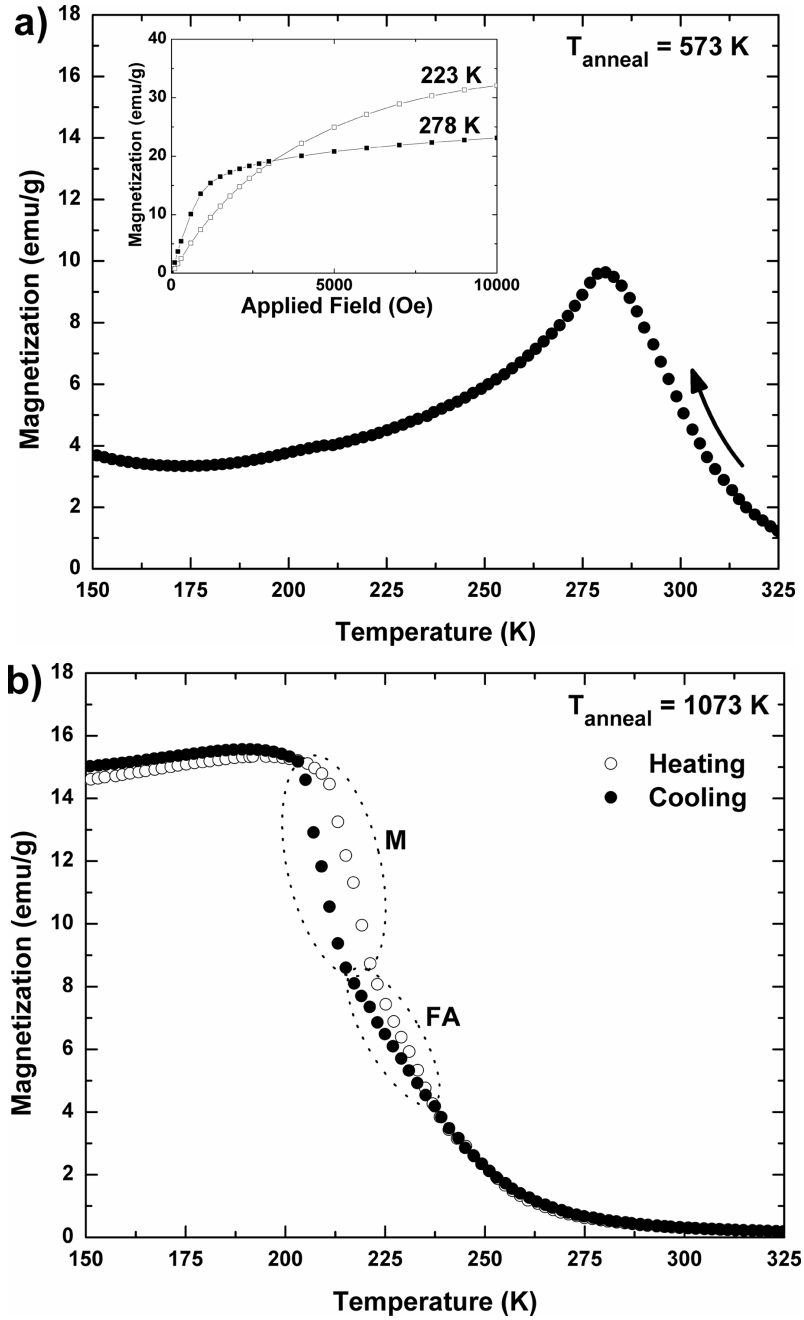

Figure 4.4: Thermomagnetization curves (H=500 Oe) for $Ni_{53}Fe_{19}Ga_{28}$ annealed at a) 573 K for 3600 s and b) 1073 for 3600 s. The inset in Figure 4.4a shows magnetization curves at 223 K and 278 K for $Ni_{53}Fe_{19}Ga_{28}$ annealed at 573 K for 3600 s.

In situ optical microscopy using a Nomarski interferometer was conducted on the specimen annealed at 1073 K for 3600 s during cooling to reveal the evolution of phases from surface relief on the specimen. The temperatures of the structural transformations determined by the calorimetry data and the optical microscopy data differ up to about 25

K degrees. It is expected that this discrepancy results from differences in temperature calibration and cooling rates used in the two instruments, i.e. 0.167 K/s for differential scanning calorimetry and 0.417 K/s for optical microscopy.

Figure 4.5 shows the microstructural evolution from room temperature to 191.5 K. A fine acicular structure with structural domain widths of a few microns appears at approximately 240 K and becomes more pronounced during cooling. The temperature at which the surface relief first appears is considerably higher than the martensite transformation revealed by the calorimetry data (see Figure 4.5). Figure 4.6 shows that when the specimen is further cooled, the martensite corresponding to the calorimetry peak appears as coarse plates that are tens of microns in width. The nucleation and growth progression of the martensite plates, as well as the peak in the calorimetry data, indicate that this is the common first order thermoelastic martensite transformation that occurs in shape memory alloys.

The thermomagnetization curves in Figure 4.4b can be divided into different regions that correlate to the progression of structural transformations. The region labeled FA (fine acicular) highlights splitting of the magnetization between heating and cooling, beginning at about 240 K on cooling and corresponding to the appearance of the fine acicular morphology. In the region labeled M (martensite), starting at about 215 K, the magnetization splitting no longer increases in magnitude, but rather the curves remain parallel. In this region, the parallel magnetization curves on heating and cooling correspond to the thermal hysteresis associated with the martensite transformation.

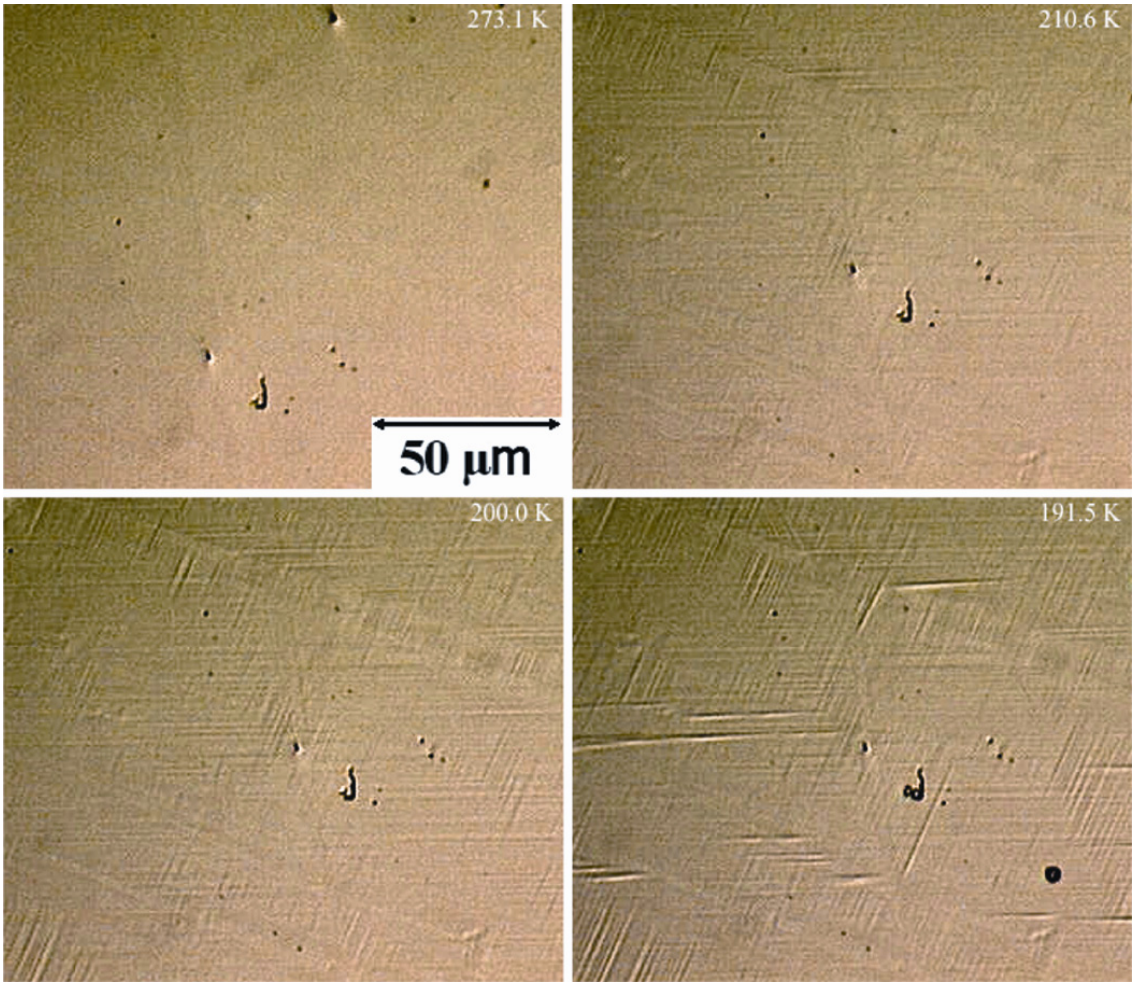

Figure 4.5: Optical micrographs of the fine acicular structure that appears during cooling in $Ni_{53}Fe_{19}Ga_{28}$ annealed at 1073 K for 3600 s.

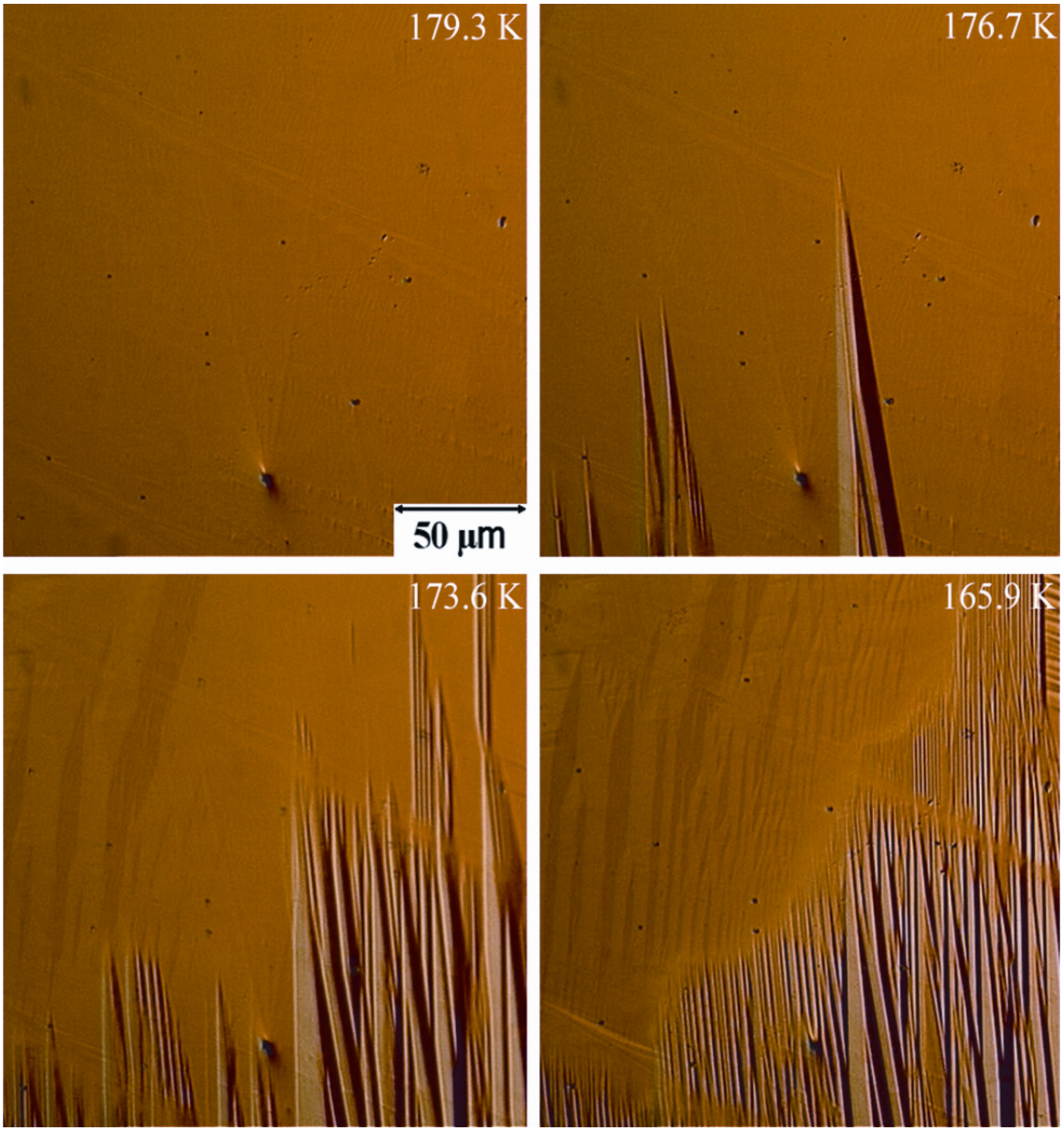

Figure 4.6: Optical micrographs of the coarse martensite that forms at temperatures below the fine acicular structure in $Ni_{53}Fe_{19}Ga_{28}$ annealed at 1073 K for 3600 s.

The precise nature of the fine acicular structure in Figure 4.5 is not clear. This apparent phase transformation does not manifest itself as a peak in the calorimetry data, and the surface relief gradually increases with decreasing temperature, rather than proceeding through a nucleation and growth mechanism. These traits imply that it may be a second order transformation. But the possibility remains that a peak is indeed present in the calorimetry data, but smeared out over a broad temperature range and hidden in the background. In a similar alloy, $Ni_{51}Fe_{22}Ga_{27}$, annealed at 773 K for 3600 s,

Omori et al. report a mixture of 10M and 14M martensite phases at low temperatures [8]. The fine acicular structure observed in our $Ni_{53}Fe_{19}Ga_{28}$ alloy may be the result of an intermartensitic transformation between these two kinds of martensite, though the lack of a peak in the calorimetry curve suggests otherwise. Also, Omori et al. observed a tweed-like premartensite phase in a $Ni_{51}Fe_{22}Ga_{27}$ alloy annealed at 1023 K for 3600 s [8]. The tweed, however, was much finer (nanometers in width) than the micron-sized structural domains we observed with optical microscopy. Khachaturyan has suggested that an adaptive martensite phase can form at higher temperatures than the normal martensite transformation in other ferromagnetic shape memory alloys, such as Fe-Pd [10]. But the adaptive phase that he reports occurs at a temperature only 8 K degrees greater than the normal martensite transformation. This temperature difference is considerably less than that of about 40 K degrees between the first appearance of the fine acicular structure and the normal martensite transformation in our alloy. The true nature of the fine acicular structure is not currently apparent, and further investigations with transmission electron microscopy are required to classify this structure.

4.4 Summary

Effects of annealing heat treatments on the martensite transformation in a $Ni_{53}Fe_{19}Ga_{28}$ ferromagnetic shape memory alloy were investigated. It was determined that annealing at temperatures below and above the $B2/L2_1$ ordering temperature for varying lengths of time shifts the martensite transformation temperature and Curie temperature by up to 70 K degrees. Our results suggest that $L2_1$ order in austenite with large antiphase domains raises the Curie temperature, and small antiphase domains in austenite lower the martensite transformation temperatures. Temperature dependent optical microscopy showed that a fine acicular structure formed during cooling about 40 K degrees above the traditional thermoelastic martensite transformation. This fine acicular structure may be evidence of an intermartensitic transformation, a premartensite phenomenon, or an adaptive martensite. Further investigations with transmission electron microscopy are necessary to uncover the nature of the fine acicular structure.

4.5 References

[1] V.A. Chernenko, E. Cesari, V.V. Kokorin, I.N. Vitenko, Acta Mat., **33**, 1239 (1995).

[2] K. Oikawa, T. Ota, Y. Sutuo, T. Ohmori, R. Kainuma, K. Ishida, Mat. Trans., **43**, 2360 (2002).

[3] K. Oikawa, T. Ota, T. Ohmori, Y. Tanaka, H. Morito, A. Fujita, R. Kainuma, K. Fukamichi, K. Ishida, App. Phys. Lett., **81**, 5201 (2002).

[4] K. Oikawa, T. Omori, R. Kainuma, K. Ishida, J. Magn. Magn. Mat., **272-276**, 2043 (2004).

[5] M.R. Sullivan, H.D. Chopra, Phys. Rev. B, **70**, 094427 (2004).

[6] R. Kainuma, F. Gejima, Y. Sutou, I. Ohnuma, K. Ishida, Mat. Trans. JIM, **41**, 943-949 (2000).

[7] Y. Murakami, D. Shindo, K. Oikawa, R. Kainuma, K. Ishida, App. Phys. Lett., **85**, 6170, (2004).

[8] T. Omori, N. Kayima, Y. Sutou, K. Oikawa, R. Kainuma, K. Ishida, Mat. Sci. Eng. A, **378**, 403 (2004).

[9] Z.H. Liu, H. Liu, X.X. Zhang, M. Zhang, X.F. Dai, H.N. Hu, J.L. Chen, G.H. Wu, Phys. Lett. A, **329**, 214-220 (2004).

[10] A.G. Khachaturyan, S.M. Shapiro, S. Semenovskaya, Phys. Rev. B, **43**, 10832 (1991).

Chapter 5 A two-dimensional phase-field computational model demonstrating the ferromagnetic shape memory effect in Ni_2MnGa

5.1 Introduction

Over the past ten years, a computational method for modeling microstructural evolution, called the phase-field method, has emerged as a useful tool for studying many different microstructural evolution processes. These processes include solidification, solid-state phase transformations, coarsening and grain growth, and dislocation dynamics. For a recent review of phase-field modeling efforts, see a paper by L.Q. Chen [1].

In conventional approaches to modeling microstructural evolution, the interfaces between regions in a microstructure are considered to be sharp interfaces. As the microstructure changes, the positions of the sharp interface must be tracked. This approach works well for simple one dimensional systems, but two and three dimensional microstructures with complex morphologies often times render it unfeasible. The phase-field method approximates these interfaces as diffuse interfaces, i.e. the change across them is steep but still continuous. As a result, a continuum equation can be used to describe the microstructural evolution, and the interfaces no longer must be tracked. There are three continuum equations commonly used in phase field models: the Cahn-Hilliard nonlinear diffusion equation, the time-dependent Ginzburg-Landau equation, and the magnetodynamic Landau-Lifshitz equation [1].

A phase-field model describes a microstructure, i.e. the structural, magnetic, or composition domains contained in it, as well as the interfaces between them, by using a set of field variables. The driving force for the microstructural evolution is defined using a free energy description based on the physical mechanisms assumed to be involved in the process. Then, the field variables are allowed to evolve to an equilibrium state that is governed by the mathematical free energy functional. Phase-field models assume that all the thermodynamic and kinetic coefficients can be related to microscopic parameters.

5.1.1 Martensite Phase Field Model

In 2002, Artemev, et al., developed a phase-field model to describe a proper cubic-to-tetragonal martensitic transformation in a polycrystalline Fe-31at% Ni alloy under an applied stress [2]. The free energy description of the martensitic transformation is based on the microelasticity theory developed by Khachaturyan [3]. The field variables in the model represent the three possible tetragonal martensite variants. The free energy description (called the free energy functional) they used to model the martensite transformation is:

$$G = G_{ch} + G_{interface} + G_{elastic} + G_{\sigma app} \tag{4.1}$$

where G is the total free energy of the system, G_{ch} is the chemical free energy, $G_{interface}$ is the twin boundary energy between martensite variants, $G_{elastic}$ is the elastic energy generated by the martensite variants, and $G_{\sigma app}$ is the free energy contribution from an applied stress. All of these free energy terms are functions of the field variables that describe the martensite variants.

Equation (4.1) describes the thermodynamic driving force of martensite evolution, while the time-dependent Ginzburg-Landau equation describes the time evolution of the transformation. The time-dependent Ginzburg-Landau equation is:

$$\frac{\partial \eta_p(r,t)}{\partial t} = L_{pq} \frac{\delta G}{\delta \eta_q(r,t)} + \xi(r,t) \tag{4.2}$$

where η_p are the field variables (one for each martensite variant), r and t are position and time, L_{pq} is a matrix of kinetic coefficients, $\frac{\delta G}{\delta \eta_q(r,t)}$ is the variational derivative of the free energy with respect to the field variables, and $\xi(r,t)$ is a Gaussian noise term. In essence, the time-dependent Ginzburg-Landau equation dictates that the microstructure will always evolve along the path of steepest descent of the total free energy. The morphology of Artemev's simulated microstructures is in good agreement with experimentally observed morphologies in Fe-31at% Ni alloys. Other similar phase-field models concerning the martensitic transformation in Au-Cd and Fe-Pd SMAs have been developed [4, 5].

5.1.2 Magnetic Phase-Field Model

A phase-field model examining the development of magnetic domains in a twinned, ferromagnetic microstructure was developed by Kazaryan, et al [6]. According to micromagnetic theory, the evolution of magnetic domains is described by the damping term of the time-dependent Landau-Lifshitz equation [7]:

$$\frac{\partial M(r,t)}{\partial t} = -\frac{\lambda}{M_s}[M(r)\times(M(r)\times H_{eff}(r))] \tag{4.3}$$

where $M(r)$ is the magnetization vector, M_s is the saturation magnetization, $H_{eff}(r)$ is the net magnetic field at point r, and λ is a positive constant that characterizes the damping of magnetization. The effective field, $H_{eff}(r)$, can be represented as the variational derivative of the total energy of the system with respect to magnetization, $\frac{-\delta E}{\delta M(r)}$. The total energy of the system can be described as:

$$E = E_{anis} + E_{exch} + E_{ms} + E_{app} \tag{4.4}$$

where E is the total energy, E_{anis} is the anisotropy energy of a twinned variant, E_{exch} is the exchange energy across the variant twin boundaries, E_{ms} is the magnetostatic energy, which is a measure of the long range interaction of magnetic moments in the system, and E_{app} is the energy due to an external applied magnetic field. A complex array of magnetic domain structures was observed in this model, which sheds light on the magnetic behavior of a twinned microstructure.

5.1.3 FSMA Phase-Field Model

The martensite and magnetic phase-field models outlined above lay a groundwork that can be extended to a phase-field model that describes the coupled evolution of structural and magnetic domains in FSMAs, i.e. the ferromagnetic shape memory effect. The first attempt to directly model FSMAs in this manner was done by Koyama and Onodera [8]. They developed a two-dimensional model of martensite evolution under applied stress and applied magnetic fields in Ni_2MnGa. However, the expression they used for the magnetic energy does not account for the exchange energy, the magnetostatic energy, or the energy due to the external applied magnetic field. The novel aspect of this

work is coupling the martensitic and magnetic evolution in Ni_2MnGa by utilizing a more comprehensive magnetic energy description. Ni_2MnGa was chosen as the ferromagnetic shape memory alloy for this simulation because it has been well characterized and the material parameters are readily available.

5.2 Model Parameters

The formulation and terminology used to develop the martensite free energy functional and the kinetic equation (time-dependent Ginzburg-Landau equation) in this model is based on the work by Jin, et al. [4]. Any reference to symbols for the material properties and dimensionless constants are the same as those found in her paper. The magnetic free energy functional is based on the description found in the paper by Kazaryan et al. [6]. The dimensionless constants for magnetic domain evolution are the same as those used in Jin et al. [9].

The field variables that track the martensite evolution are η_1 and η_2, which represent two correspondence variants of tetragonal martensite that are twin-related, or in our 2-dimensional case, two rectangular martensite variants. The magnitude of the strain generated during transformation from austenite to martensite is defined by the a-axis elongation and c-axis contraction reported for a Ni_2MnGa alloy: a_{aus}=0.5825 nm, a_{mart}=0.5920 nm, c_{mart}=5.566 nm [10]. The field variable η_1 has a contracted c-axis (compared to the lattice parameter of the austenite) along the x-direction, and the η_2 field variable has a contracted c-axis along the y-direction. The strain energy created from a transformation from austenite to martensite was determined using elastic constants measured for Ni_2MnGa: c_{11}=136 GPa and c_{12}=92 GPa [11].

The field variable used to describe the magnetic domain evolution is the vector M, which is a magnetization density vector for a small volume (or area) element. The M vector is resolved into Cartesian components, m_1 and m_2.

To couple the martensitic structural evolution to the magnetic domain evolution in ferromagnetic shape memory alloys, we have introduced a magnetic anisotropy energy term (E_{ani}), which contains field variables for both the martensite and the magnetization, into the martensite *and* magnetic free energy functionals. The E_{ani} energy contribution to

the total martensite free energy is particularly high in ferromagnetic shape memory alloys; it is a necessary condition for the ferromagnetic shape memory effect to occur. High magnetocrystalline anisotropy in the martensite orientation variants prevents the magnetization vectors from rotating in the direction of an applied magnetic field. This effect results in a high Zeeman energy difference across twin boundaries and exerts a sufficient pressure on the twin boundary to facilitate twin boundary motion. So, to capture the ferromagnetic shape memory effect in a phase-field model, the E_{ani} energy contribution must be present in both free energy functionals.

$$E_{ani} = \int K_1[1-(\eta_1^{\,2} m_1^{\,2} + \eta_2^{\,2} m_2^{\,2})]d^2 r \tag{4.5}$$

where K_1 is the magnetocrystalline anisotropy constant in the martensite, m_1 and m_2 are the field variables representing the unit magnetization vector Cartesian components and η_1 and η_2 are the field variables for the two martensite variants. This representation of the anisotropy energy contribution is based on the work done by Kazaryan et al. [6]; it is possible to express E_{ani} in this way because the martensite orientation variants can be considered uniaxial single crystals with the c-axis being the magnetic easy axis.

Since the E_{ani} expression (Equation 4.5) is incorporated into both the martensite free energy functional and the magnetic free energy functional, the martensite evolution under applied stress and applied magnetic field depends on the magnetic domain structure. Simultaneously, the magnetic domain structure depends on the martensite variant morphology.

All simulations were run on a 64 x 64 mesh with periodic boundary conditions using a finite difference numerical scheme. Dimensionless input parameters were used in both the martensite and magnetic free energy functionals. The dimensionless parameter ζ is the "strength" of the martensite transformation, incorporating the amount of undercooling below the martensite transformation temperature.

$$\zeta = \frac{G\varepsilon_o^2}{\Delta f} \tag{4.6}$$

where $G\varepsilon_o^2$ is the typical strain energy of martensite transformation and Δf is the difference between the free energy of the austenite and the martensite (which depends on undercooling). For the initial evolution from austenite to martensite, ζ was set to 100, a relatively large undercooling. For the subsequent simulations under an applied stress and applied magnetic field, ζ was set to 10 to allow for variant rearrangement, effectively simulating a temperature slightly below the martensite transformation temperature. The interfacial energy term, β^*, was set to 50 to create a martensite morphology with "thick" variants to aid in later visualization of the interaction between martensite variants and magnetic domains. Using a procedure outlined in a paper by Artemev, et al., the physical length and width of the computational area was determined to be 211 nm x 211 nm [12].

The magnetic dimensionless parameter, K^*, incorporates values for K_1, the magnetocrystalline anisotropy constant in the martensite, taken as $K_1=2.5 \times 10^6$ ergs/cm^3, and the saturation magnetization of the martensite, $M_{sat} = 250$ emu/cm^3 [13].

$$K^* = \frac{K_1}{2\pi M_{sat}} \tag{4.7}$$

The magnetic exchange interaction constant, A^*, was set to 10 to enable the visualization of the martensite and magnetic domains, while still capturing most pertinent features of the ferromagnetic shape memory effect. The periodic boundary conditions play a prominent role in the equilibrium magnetic domain structures with a relatively small computational mesh size of 64 x 64. The periodic boundary conditions prevent the magnetic domain structure from forming enough 180º magnetic domain walls to fully minimize the magnetostatic energy contribution. However, computational time increases quickly with increasing mesh size, and since these simulations were run on a personal computer, using a small mesh size was imperative. As a result of this compromise, the computational model can no longer be considered "quantitative," but it does represent qualitatively the effects of applied magnetic and stress fields on FSMAs.

5.3 Results and Discussion

Figure 5.1 is the equilibrium martensite structure after the evolution from austenite. Dark gray represents Variant 1 (η_1), which has the contracted c-axis in the x-direction, and the light gray region is Variant 2 (η_2), which has the contracted c-axis in

the y-direction. The twin boundaries between variants adopt a 45º angle relative to the x- and y-axes to minimize the elastic strain energy, and are straight to minimize the interfacial energy.

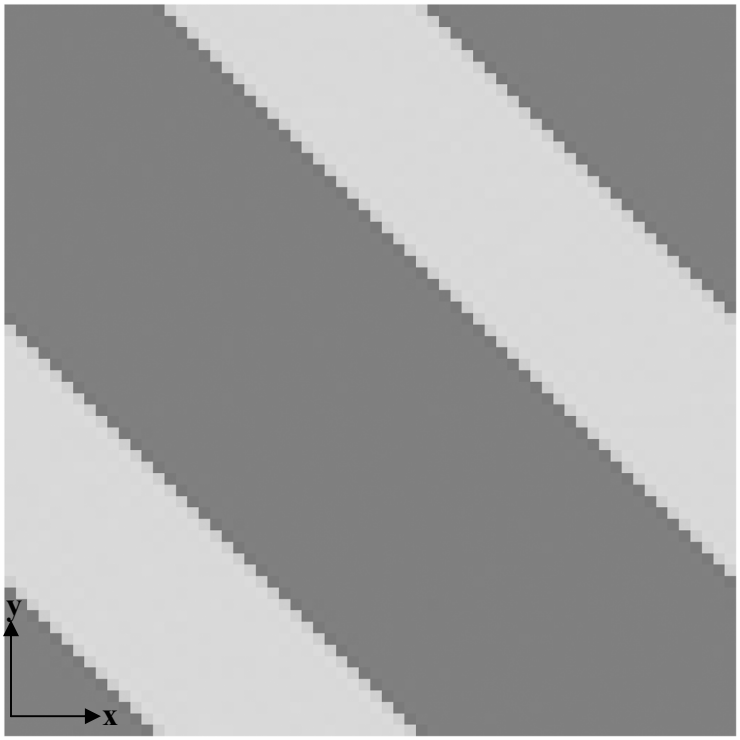

Figure 5.1: Equilibrium martensite microstructure, simulated without the magnetic energy contribution. Dark gray is Variant 1 and Light Gray is Variant 2.

Figure 5.2 shows the random initial configuration of the magnetization vectors before the coupled structural and magnetic evolution simulation was peformed. Figure 5.3 is a schematic diagram of an idealized magnetic domain structure that forms in a polydomain structure with uniaxial magnetic anisotropy [9]. Within structural variants, 180º magnetic domain walls are present, with 90º magnetic domains walls along the twin boundaries between variants. All magnetic domains have a magnetization direction such that no head-to-head or tail-to-tail interactions are present, which is a result of the magnetostatic energy contribution.

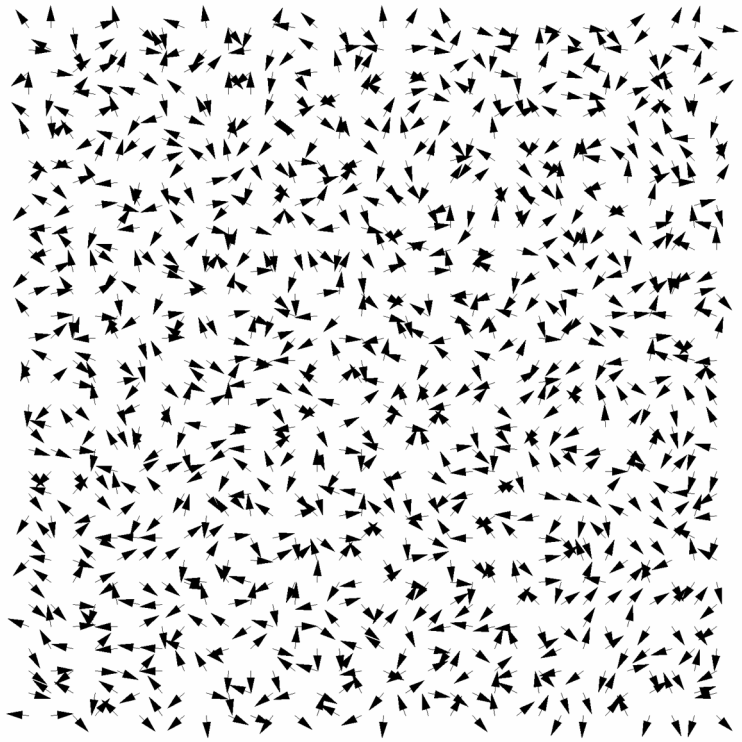

Figure 5.2: Initial configuration of magnetic domain structure. Magnetization vectors are in a random configuration.

Figure 5.4 is the equilibrium martensitic and magnetic configuration after the simulation was run for 30000 time steps of with a time step of dt*=0.01. The magnetic domain structure is similar to that in the schematic diagram, but there are some regions of head-to-head and tail-to-tail interactions between magnetization vectors, and the magnetic domain walls are wavy and not purely of the 90º and 180º types. The magnetic domains do align themselves with the magnetic easy axis of each variant (the contracted c-axis, in the case of Ni_2MnGa). This behavior of the magnetic domain walls is attributed to the prominence of the periodic boundary influence when using a small computational area.

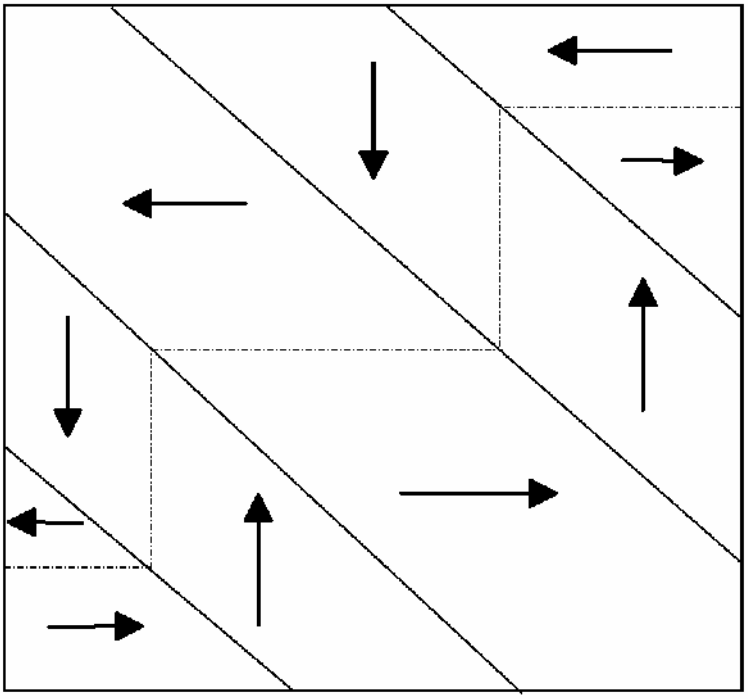

Figure 5.3: Schematic diagram of idealized magnetic domain structure in a polytwinned material.

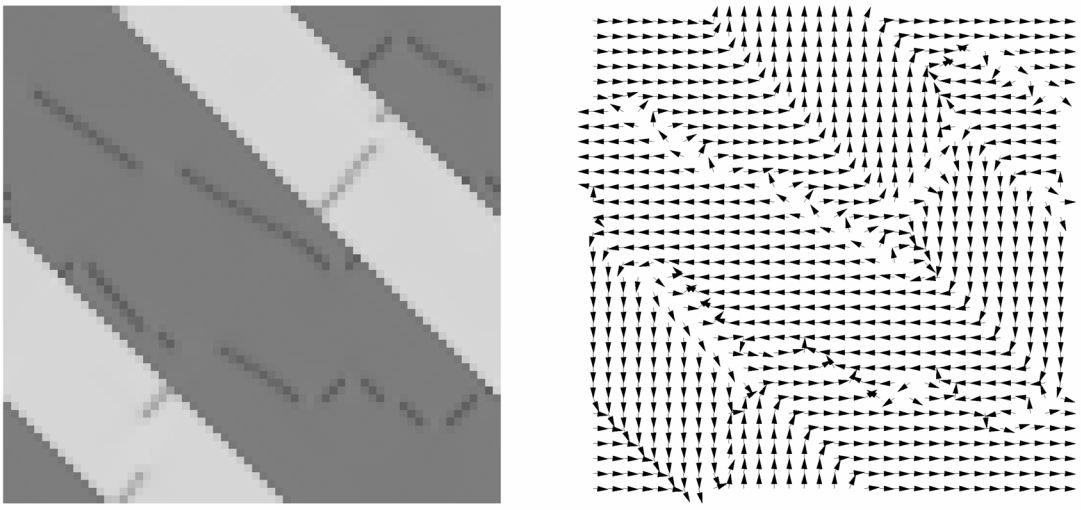

Figure 5.4: Equilibrium martensitic and magnetic structures, used as a starting point for simulations with applied stress and applied magnetic field.

A series of simulations with increasing compressive stress applied along the x-direction resulted in variant rearrangement and changes in the magnetic domain structure.

Simulations under applied stress were evaluated to determine if a net magnetization remains after full conversion from a polytwinned structure to a single variant of martensite. Figure 5.5 shows the area fraction of the martensite variants as a function of dimensionless compressive stress. After minor changes in the area fractions up to a critical reduced applied stress of 5, Variant 1 increases to an area fraction of 1 as Variant 2 decreases to an area fraction of 0. This variant rearrangement occurs to minimize the strain energy by increasing the area of the variant with the contracted c-axis parallel to the compressive stress. When the reduced applied stress is released, the martensite morphology does not revert back to a two-variant state, as the structure sits in a local free energy minimum. Figure 5.6 shows the effect of reduced applied stress on the dimensionless magnetization in the x-direction. The magnetization increases slightly in the x-direction as the area fraction of Variant 1 increases, because the magnetic easy axis of Variant 1 lies in the x-direction, but the effect is not large because the magnetostatic energy promotes magnetic domain arrangements that avoid any net stray magnetic fields. After the stress was released, there was a minor change in the magnetization from the motion of one region of a magnetic domain wall.

Figure 5.7, Figure 5.8, and Figure 5.9 show the martensite morphology and magnetic domain configuration at reduced applied stresses of 5, 6.25, and 7.5, respectively. Domain walls tend to either depress the field variable in that area, or provide low energy areas for one variant to grow into another. It is believed that the fingers of Variant 1 growing into Variant 2 (see Figure 5.7) is an artifact of periodic boundary conditions resulting from the small computational area, which creates artificially thick magnetic domain walls.

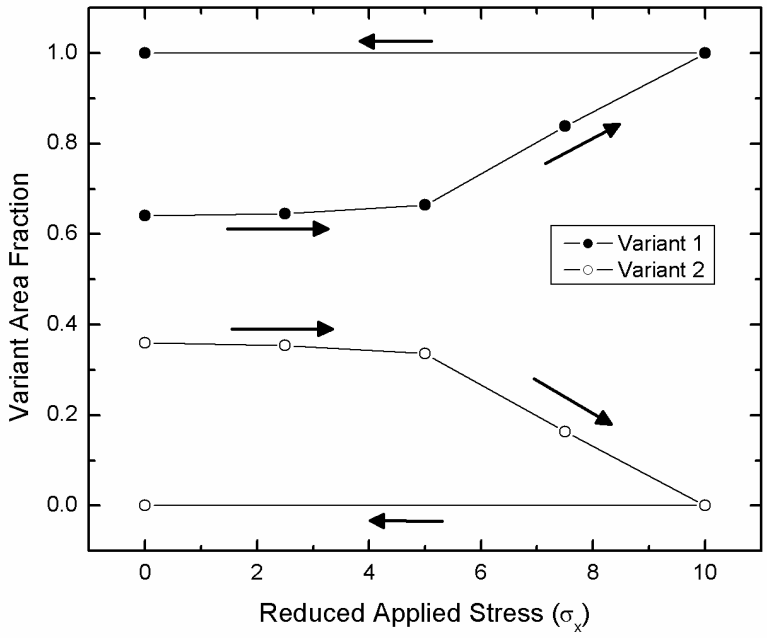

Figure 5.5: Martensite variant area fraction as a function of reduced applied compressive stress in the x-direction.

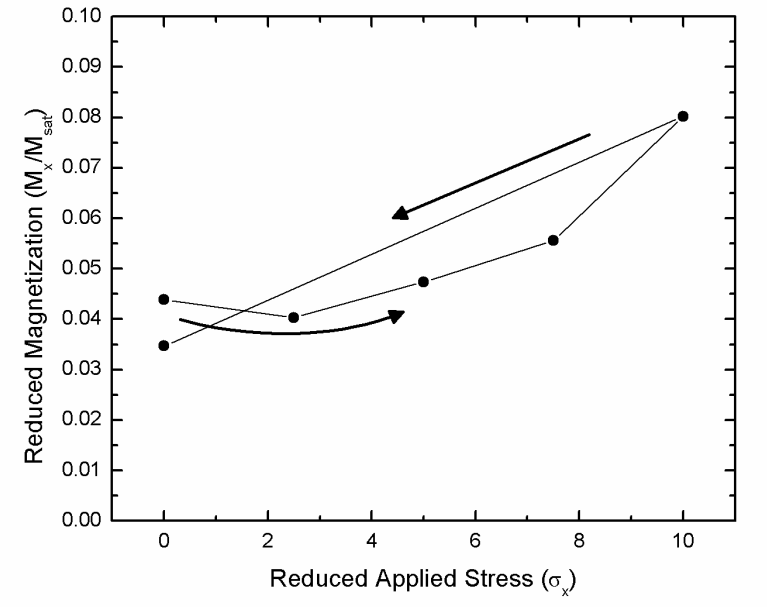

Figure 5.6: Reduced magnetization in the x-direction as a function of reduced applied compressive stress in the x-direction.

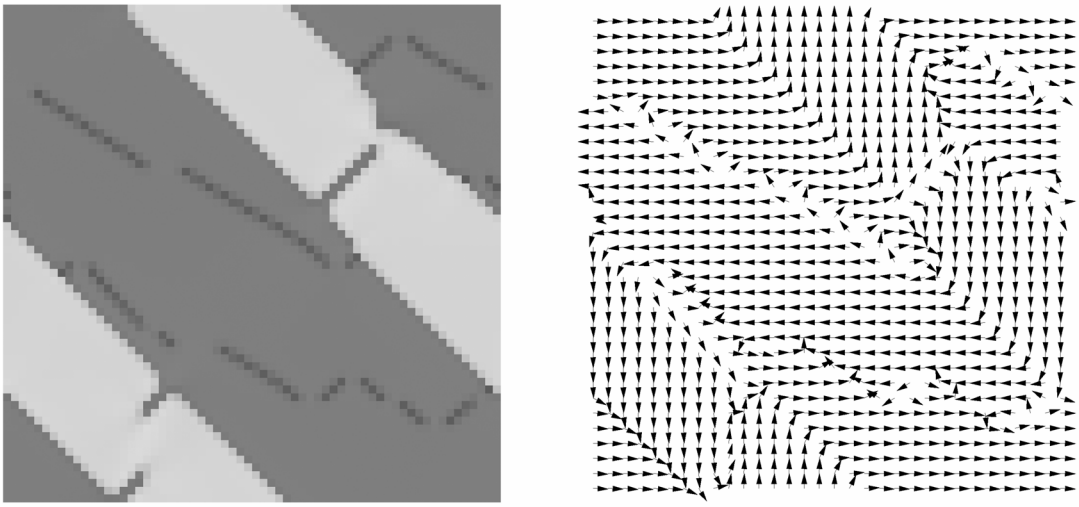

Figure 5.7: Martensite microstructure and magnetic domain structure under a reduced compressive stress in the x-direction (σ_x=5).

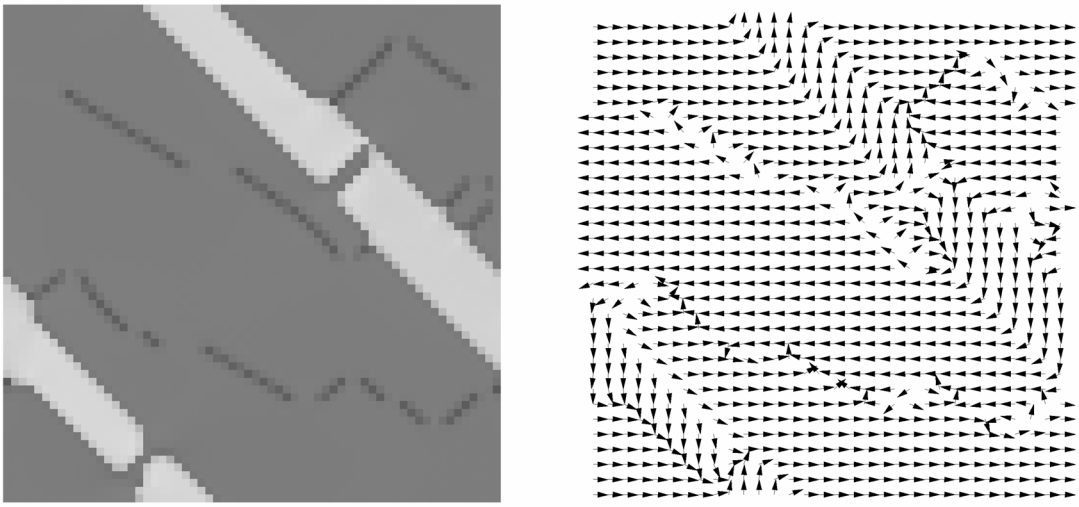

Figure 5.8: Martensite microstructure and magnetic domain structure under a reduced compressive stress in the x-direction (σ_x=6.25).

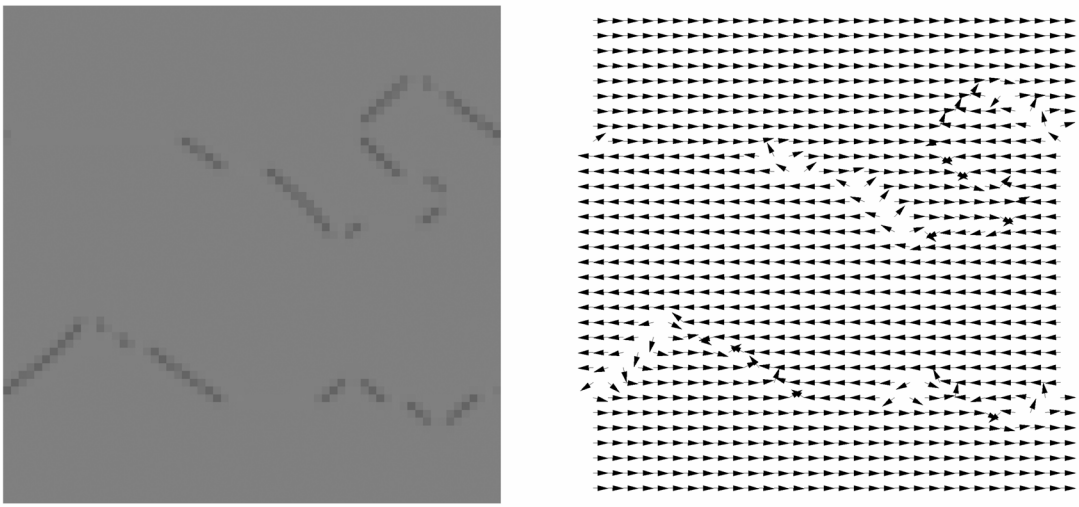

Figure 5.9: Martensite microstructure and magnetic domain structure under a reduced compressive stress in the x-direction (σ_x=7.5).

The effect applied magnetic fields on the martensite morphology and magnetic domain structure was studied by evaluating simulations with increasing reduced applied magnetic field in the x-direction. An increase in the area fraction of Variant 1 (magnetic easy axis parallel to the applied magnetic field direction), which is analogous to an elongation in the y-direction, is the primary indicator of the ferromagnetic shape memory effect. The progression of the magnetic domain rearrangement during the increase in magnetization with increasing reduced applied magnetic field is also evident.

Figure 5.10 shows the variant area fraction as a function of reduced applied magnetic field in the x-direction. At reduced applied magnetic fields less than 8, the area fraction of Variant 1 only slightly increases. But as the reduced applied magnetic field is further increased, the pressure exerted on the twin boundaries (from the Zeeman energy) becomes large enough that the twin boundaries migrate through the computational area, increasing the area fraction of Variant 1 while consuming Variant 2. When the reduced applied magnetic field is released, the morphology remains in a single-variant state because this martensite configuration is in a local free energy minimum.

In Figure 5.11, up to a reduced applied magnetic field of 2.5, the reduced magnetization increases rapidly with increasing applied magnetic field. Similar magnetization behavior with increasing applied magnetic field has been seen experimentally in a Ni_2MnGa single crystal [14]. Figure 5.12, Figure 5.13, Figure 5.14,

Figure 5.15, Figure 5.16, and Figure 5.17 show the structural and magnetic domain evolution at reduced applied magnetic fields of 2.5, 5, 7.5, 10, 10.5, and 11.75, respectively. Even at low reduced applied magnetic fields, magnetization vectors in Variant 1 rearrange to form a single domain aligned in the direction of the applied magnetic field. This elimination of the reverse magnetic domain in Variant 1 contributes mostly to the rapidly increasing magnetization in the x-direction at low fields. As the reduced applied magnetic field is increased up to 8, the 180º magnetic domain walls in Variant 2 migrate to minimize the area of head-to-head or tail-to-tail magnetization vector interactions, and thus minimize the magnetostatic energy contribution. When the reduced applied magnetic field is reduced to zero, the reduced magnetization in the x-direction remains at 1, i.e. a single magnetic domain with all magnetization vectors aligned parallel to the direction of the previously applied reduced magnetic field. The small computational area and periodic boundary conditions suppress the magnetostatic energy term so the formation of anti-parallel magnetic domains does not occur. This result does not represent the true behavior in ferromagnetic shape memory alloys, and is considered a limitation in using a small computational area in these simulations.

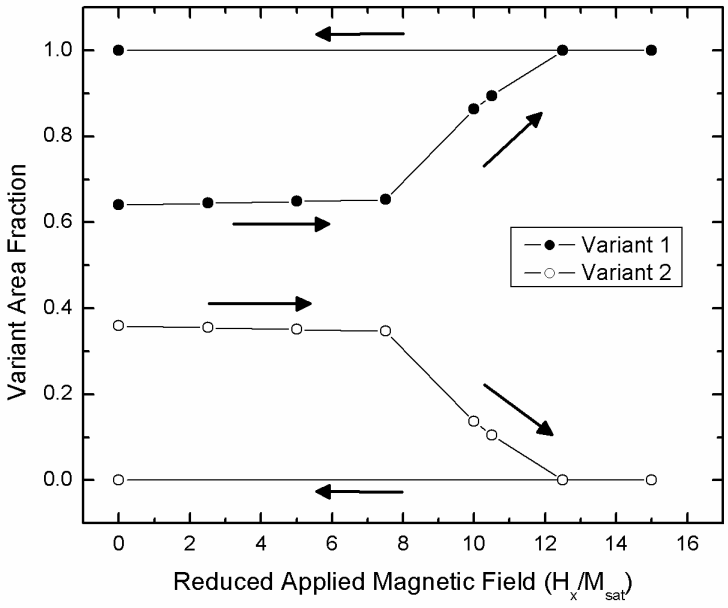

Figure 5.10: Martensite variant area fraction as a function of reduced applied magnetic field in the x-direction.

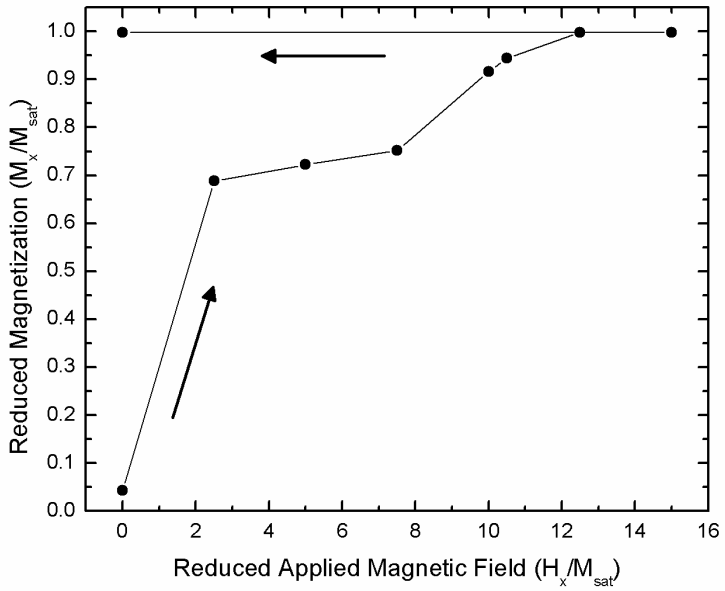

Figure 5.11: Reduced magnetization in the x-direction as a function of reduced applied magnetic field in the x-direction.

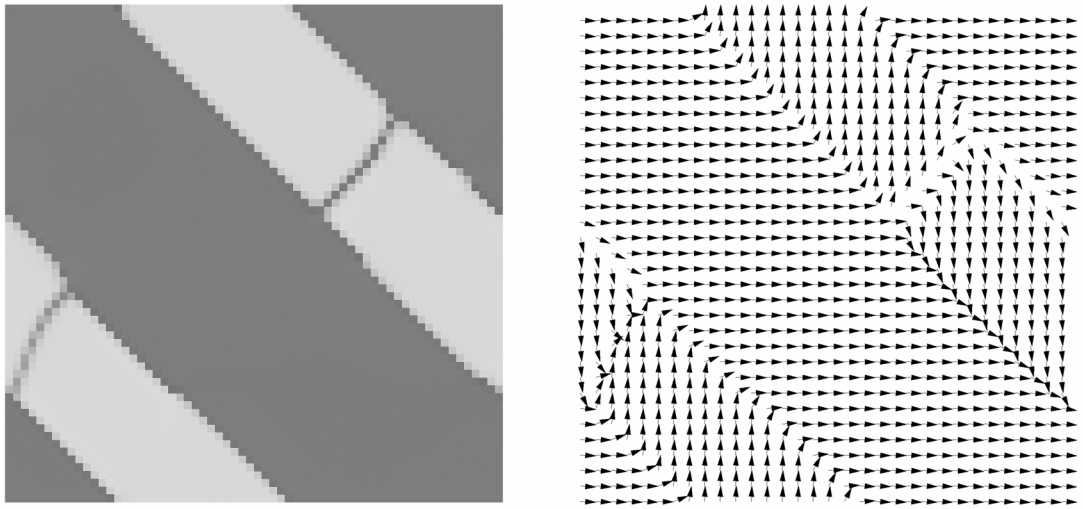

Figure 5.12: Martensite microstructure and magnetic domain structure under a reduced applied magnetic field in the x-direction (h_x=2.5).

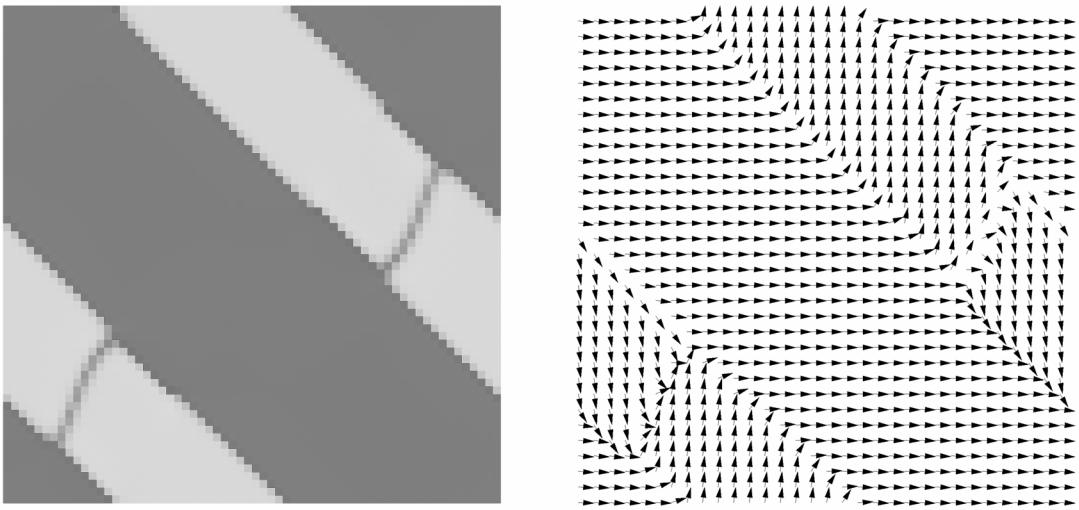

Figure 5.13: Martensite microstructure and magnetic domain structure under a reduced applied magnetic field in the x-direction (h_x=5).

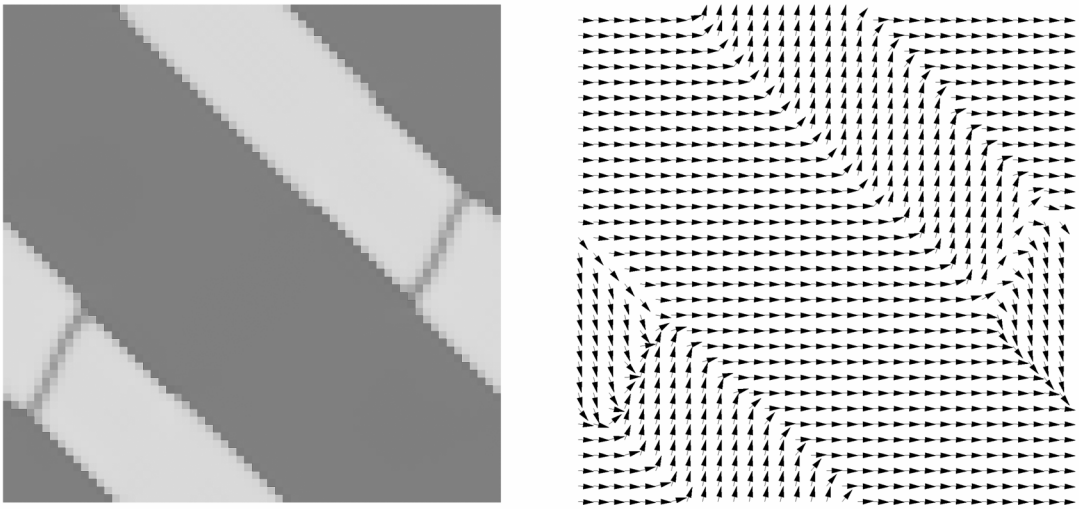

Figure 5.14: Martensite microstructure and magnetic domain structure under a reduced applied magnetic field in the x-direction (h_x=7.5).

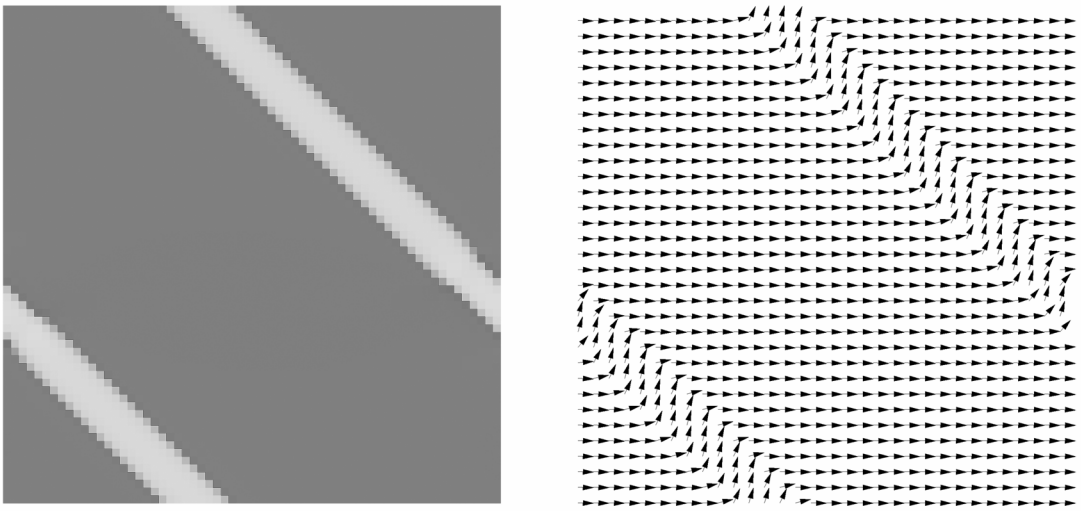

Figure 5.15: Martensite microstructure and magnetic domain structure under a reduced applied magnetic field in the x-direction (h_x=10).

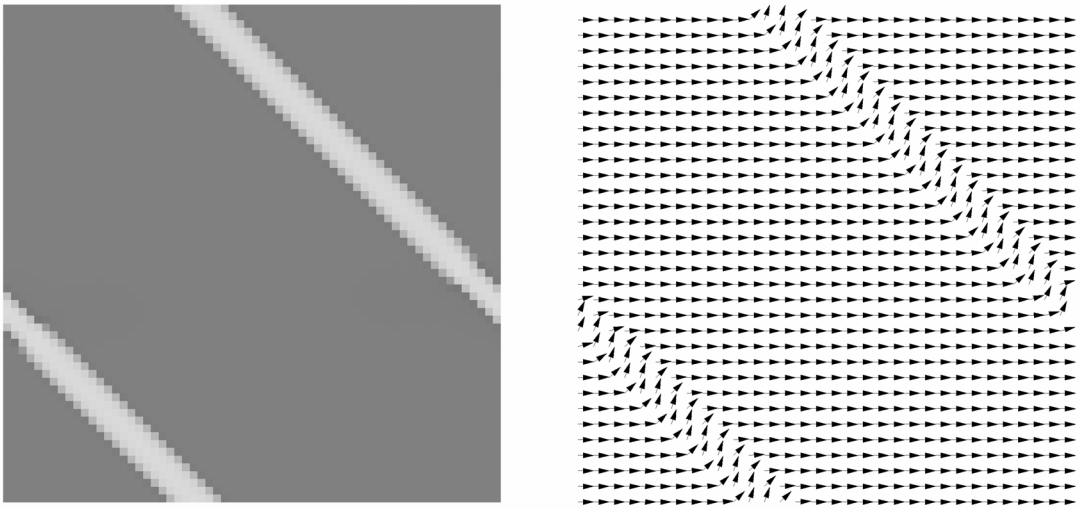

Figure 5.16: Martensite microstructure and magnetic domain structure under a reduced applied magnetic field in the x-direction (h_x=10.5).

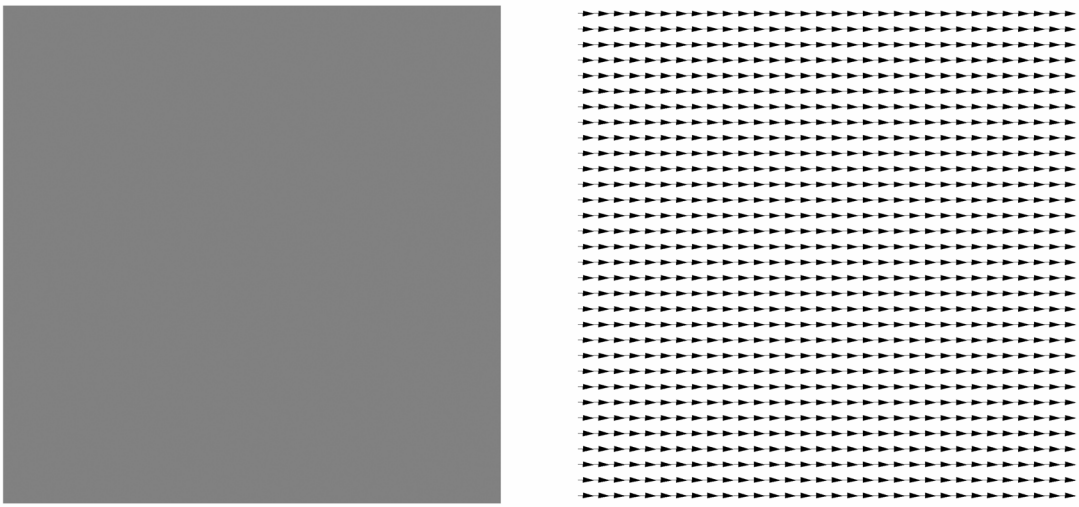

Figure 5.17: Martensite microstructure and magnetic domain structure under a reduced applied magnetic field in the x-direction (h_x=11.75).

5.4 Summary

A phase-field model has been developed that couples magnetic and martensitic domain evolution and effectively captures many of the qualitative behaviors of ferromagnetic shape memory alloys. Applied stress causes variant rearrangement that reduces elastic energy, while the material experiences only minor changes in the net magnetization. As applied magnetic field is increased, the magnetization response is similar to experimental curves. It is apparent that the initial magnetization increase with increasing reduced applied magnetic field is a result of the disappearance of reverse magnetic domains in the variant with its magnetic easy axis parallel to the reduced applied magnetic field. With increasing reduced applied magnetic fields, magnetic domain wall motion in the variant with the easy axis *perpendicular* to the applied field reduces the magnetostatic energy, until eventually enough magnetic pressure is exerted on the twin boundary to cause significant variant rearrangement. The small computational area used in these simulations introduces periodic boundary conditions that suppress the magnetostatic energy term, and thus the formation of 180º magnetic domain walls. Increasing the computational area is a necessary requirement for the

advancement of this model towards making quantitative predictions of the ferromagnetic shape memory effect in Ni_2MnGa.

5.5 References

[1] L.Q. Chen, Annu. Rev. Mater. Res., **32**, 113 (2002).

[2] A. Artemev, Y. Jin and A.G. Khachaturyan, Phil. Mag. A, **82**, 1249 (2002).

[3] A.G. Khachaturyan, *Theory of Structural Transformations in Solids* (John Wiley and Sons, New York, 1983).

[4] Y.M. Jin, A. Artemev and A.G. Khachaturyan, Acta Mater., **49**, 2309 (2001).

[5] R. Ahluwalia, T. Lookman, A. Saxena and R.C. Albers, Acta Mater., **52**, 209 (2004).

[6] A. Kazaryan, Y. Wang, Y.M. Jin, Y.U. Wang, A.G. Khachaturyan, L. Wang and D.E. Laughlin, J. Appl. Phys., **92**, 7408 (2002).

[7] W.F. Brown, *Micromagnetics* (Interscience Publishers, New York, 1963).

[8] T. Koyama and H. Onodera, Mat. Trans., **44**, 2503 (2003).

[9] Y.M. Jin, Y.U. Wang, A. Kazaryan, Y. Wang, D. Laughlin and A.G. Khachaturyan, J. App. Phys., **92**, 6172 (2002).

[10] P.J. Webster, K.R.A. Ziebeck, and S.L. Town, Phil. Mag. B, **49**, 295 (1984).

[11] L. Manosa, A. Gonzalez-Gomez, E. Obrado, A. Planes, V.A. Chernenko, V.V. Kokorin, and E. Cesari, Phys. Rev. B., **55**, 11068 (1997).

[12] A. Artemev, Y.M. Jin, and A.G. Khachaturyan, Phil. Mag. A, **82**, 1249 (2002).

[13] Q. Pan and R.D. James, J. App. Phys., **87**, 4702 (2000).

[14] K. Ullakko, J.K. Huang, C. Kantner and R.C. O'Handley, Appl. Phys. Lett., **69**, 1966 (1996).

Appendix 1 Ferromagnetic shape memory effect phase-field code written in and executed using *Mathematica 5.2* software

Initial Setup

```
(* Turns off annoying spelling error messages *)
Off[General::"spell1"];
Off[General::"spell"];

(* Shares memory before starting calculations *)
Share[]

(* Sets the directory for saving data files and/or pictures *)
SetDirectory["C:\\Documents and Settings\\Todd Heil\\Desktop\\"]

(* output file names are determined by a user selected prefix ("outprefix", defined below
by the user) and the program execution time *)
rundate=Date[];
year=ToString[rundate[[1]]];
mo=ToString[PaddedForm[rundate[[2]],
    2,NumberPadding->{"0","0"},NumberSigns->{"",""}]];
day=ToString[PaddedForm[rundate[[3]],
    2,NumberPadding->{"0","0"},NumberSigns->{"",""}]];
hour=ToString[PaddedForm[rundate[[4]],
    2,NumberPadding->{"0","0"},NumberSigns->{"",""}]];
min=ToString[PaddedForm[rundate[[5]],
    2,NumberPadding->{"0","0"},NumberSigns->{"",""}]];
startTime=StringJoin[year, "_", mo,"_", day,".", hour,min];
```

Constants Defined By The User

```
(*
```

outprefix = the first part of the file names of exported data;

ϕ = interfacial energy between structural variants;

a, b, c = coefficients in the chemical free energy equation (Gch);

ζ = strength of the martensite transformation: $1/\triangle f$, where $\triangle f$ is the chemical driving force for the martensite transformation (depends on undercooling);

c11, c12 = Elastic constants (Pa) (Ni2MnGa constants used below from L. Manosa, A. Gonzalez-Gomez, E. Obrado, A. Planes, V.A. Chernenko, V.V. Kokorin, and E. Cesari, Phys. Rev. B., **55**, 11068 (1997).);

$\in 1$, $\in 2$ = Defines the tetragonal (or rectangular in the case of 2-D) strain resulting from austenite to martensite transformation, i.e. $\in 1 = (a_{tetragonal} - a_{cubic})/a_{cubic}$ and $\in 2 = (c_{tetragonal} - a_{cubic})/a_{cubic}$ (Ni2MnGa values are taken from P.J. Webster, K.R.A. Ziebeck, and S.L. Town, Phil. Mag. B, **49**, 295 (1984).)

Betastarmart= Exchange energy term for magnetic free energy functional;

Kstarmart=Magnetocrystalline anisotropy term;

hextmart=reduced applied magnetic field term;

nx,ny = x and y cell (pixel) dimensions of the computational volume (or computational area in 2-D);

dx,dy = individual cell sizes;

sig = standard deviation of gaussian thermal noise term to be applied to order parameter (s1 and s2) fields;

dt = time step;

totaltime = total time of the simulation;

ChkPct = percentages of the total simulation for which plots should be generated and/or data saved to files;

*)

```
outprefix=single_xtal_MT ;
  φ=50.;
  a=0.14;
  b=3*a+12;
  c=2*a+12;
  ζ= 10.;
```

```
c11=1.36*10^11;
c12=0.92*10^11;
∈1=-0.044;
∈2=0.016;
Betastarmart= 10.;
Kstarmart=6.37;
hextmart={0.,0.};
nx=64;
ny=64;
dx=1.;
dy=1.;
sig = 0.001;
dt=0.01
totaltime=10000*dt;
ChkPct=2.5;
```

Initial Calculations

```
(* Defines the chemical free energy expression that describes austenite transforming to
Variant 1(s1), Variant 2 (s2) *)
fa=1/2*a*(#1^2+#2^2)-1/3*b*(#1^3+#2^3)+1/4*c*(#1^2+#2^2)^2&;

(* Finds the derivative of the fa function w.r.t. the s1 variable *)
D[fa[var1,var2],var1]

(* Define the dfa/ds function based on the result from the above cell *)
dfads=(a*#1-b*#1^2+c*#1*(#1^2+#2^2))&;

(* Plots fa and dfa/ds functions vs. s1 *)
Plot[fa[s1,0],{s1,-1,2},PlotStyle→{RGBColor[1,0,0]},PlotRange→{-
1,1},Frame→True,FrameLabel→{"Order Parameter (s1)","Energy (dimensionless)"}];
```

```
Plot[dfads[s1,0],{s1,-1,1},PlotRange→{-10,10},Frame→True,FrameLabel→{"Order
Parameter (s1)","d(Energy)/d(s1)"}];

(* c44 elastic constant determined from user defined c11 and c12 constants *)
c44=(c11-c12)/2;

(* Defines Lame's Constants for calculating the Ωij matrix below *)
λ=c12;
μ=(c11-c12)/2;
ν=λ/(2*(λ+μ));

(* creates the stiffness tensor in matrix notation *)
cij={{c11,c12,c12,0,0,0},{c12,c11,c12,0,0,0},{c12,c12,c11,0,0,0},{0,0,0,c44,0,0},{0,0,0
,0,c44,0},{0,0,0,0,0,c44}};

(* expands the stiffness tensor from matrix notation *)
cmatrixtotensor[cij_]:=Module[{Cijkl},Cijkl=Table[Which[i+j==2,Which[k+l==2,cij[[1,1]
],k+l==3,cij[[1,6]],k+l==4&&k==l,cij[[1,2]],k+l==4,cij[[1,5]],k+l==5,cij[[1,4]],k+l==6,cij[[1,
3]]],i+j==3,Which[k+l==2,cij[[6,1]],k+l==3,cij[[6,6]],k+l==4&&k==l,cij[[6,2]],k+l==4,cij[[6
,5]],k+l==5,cij[[6,4]],k+l==6,cij[[6,3]]],i+j==4&&i==j,Which[k+l==2,cij[[2,1]],k+l==3,cij[[2
,6]],k+l==4&&k==l,cij[[2,2]],k+l==4,cij[[2,5]],k+l==5,cij[[2,4]],k+l==6,cij[[2,3]]],i+j==4,W
hich[k+l==2,cij[[5,1]],k+l==3,cij[[5,6]],k+l==4&&k==l,cij[[5,2]],k+l==4,cij[[5,5]],k+l==5,ci
j[[5,4]],k+l==6,cij[[5,3]]],i+j==5,Which[k+l==2,cij[[4,1]],k+l==3,cij[[4,6]],k+l==4&&k==l,c
ij[[4,2]],k+l==4,cij[[4,5]],k+l==5,cij[[4,4]],k+l==6,cij[[4,3]]],i+j==6,Which[k+l==2,cij[[3,1]
],k+l==3,cij[[3,6]],k+l==4&&k==l,cij[[3,2]],k+l==4,cij[[3,5]],k+l==5,cij[[3,4]],k+l==6,cij[[3,
3]]]],{i,1,3},{j,1,3},{k,1,3},{l,1,3}];
    Cijkl];

Cijkl=cmatrixtotensor[cij];

(* loads "ContinuousDistributions" package for the gaussian thermal noise term*)
```

```
<<Statistics`ContinuousDistributions`

(* Creates the phase-fields of order parameters s1 and s2 (martensite variants 1 and 2)
with initial gaussian thermal noise *)
ndist=NormalDistribution[0,sig];
s1=RandomArray[ndist,{nx,ny}];
s2=RandomArray[ndist,{nx,ny}];

(* Determines the size of the computational area *)
V=nx*ny*dx*dy;

(*Creates random array of magnetization vectors on a nx x ny computational area, then
divides into arrays of x- and y-components only (m1 and m2)*)
m=Developer`ToPackedArray[Table[{Random[Real,{-1,1}],Random[Real,{-
1,1}]},{i,nx},{j,ny}]];
normm=Developer`ToPackedArray[Table[m[[i,j]]/Norm[m[[i,j]]],{i,nx},{j,ny}]];
m1=Developer`ToPackedArray[Table[normm[[i,j,1]],{i,nx},{j,ny}]];
m2=Developer`ToPackedArray[Table[normm[[i,j,2]],{i,nx},{j,ny}]];

(* Define functions to describe the components of the real space vectors in the
computational volume and the components of the k-space vectors in the 1st Brillouin
zone *)
rcompx[i_]:=If[i<=nx/2+1,N[(i-1)*dx],N[(i-(nx+1))*dx]]
rcompy[j_]:=If[j<=ny/2+1,N[(j-1)*dy],N[(j-(ny+1))*dy]]
kcompx[i_]:=Which[i≤nx/2+1,N[2*Pi*(i-1)/(nx*dx)],i>nx/2+1,N[2*Pi*(i-
(nx+1))/(nx*dx)]]
kcompy[j_]:=Which[j≤ny/2+1,N[2*Pi*(j-1)/(ny*dy)],j>ny/2+1,N[2*Pi*(j-
(ny+1))/(ny*dy)]]

(* Defines matrix of real space position vectors (rvectors), matrix of k-space vectors in
the first Brillouin zone (kvectors), and matrix of k unit vectors (evectors) *)
```

```
Timing[
  rvectors=Table[{rcompx[i],rcompy[j]},{i,1,nx},{j,1,ny}] ;
  kvectors=Table[{kcompx[i],kcompy[j]},{i,1,nx},{j,1,ny}] ;

evectors=N[Table[If[kvectors[[i,j]]=={0,0},{0,0},kvectors[[i,j]]/Norm[kvectors[[i,j]]]],{i,
1,nx},{j,1,ny}]];
  ]

(* Isolates arrays of the x and y components of the real space vectors (r1 and r2) and
isolates arrays of the x and y components of the k unit vectors (e1 and e2) *)
e1=evectors[[All,All,1]];
e2=evectors[[All,All,2]];
r1=rvectors[[All,All,1]];
r2=rvectors[[All,All,2]];

(* determines the length of the kvector at each pixel in the computational area (k), and
the squared length of kvector at each pixel in the computational area (ksquared) *)
Timing[
  k=Table[Norm[kvectors[[i,j]]],{i,1,nx},{j,1,ny}];
  ksquared=k^2;
  ]

(* ToPackedArray[expr] will change the internal representation of the array and in some
cases it will enhance the speed of execution and reduce the memory usage. *)
Cijkl=Developer`ToPackedArray[Cijkl];
s1=Developer`ToPackedArray[s1];
s2=Developer`ToPackedArray[s2];
rvectors=Developer`ToPackedArray[rvectors];
kvectors=Developer`ToPackedArray[kvectors];
evectors=Developer`ToPackedArray[evectors];
e1=Developer`ToPackedArray[e1];
```

```
e2=Developer`ToPackedArray[e2];
r1=Developer`ToPackedArray[r1];
r2=Developer`ToPackedArray[r2];
k=Developer`ToPackedArray[k];
ksquared=Developer`ToPackedArray[ksquared];

(* Defines Ωij, the Green tensor that is inverse to Cijkl*ej*ek *)
Timing[
 Ωij=Table[Table[KroneckerDelta[i,j]/μ-evectors[[x,y,i]]*evectors[[x,y,j]]/(2*μ(1-
ν)),{i,1,2},{j,1,2}],{x,nx},{y,ny}];
 Ωij=Developer`ToPackedArray[Ωij];
 ]

(* Defines the stress-free transformation strain for Variant 1 and 2 *)
ϵij00[p_]:=Which[p==1,{{ϵ2,0},{0,ϵ1}},p==2,{{ϵ1,0},{0,ϵ2}}]
ϵij00var1=Developer`ToPackedArray[ϵij00[1]];
ϵij00var2=Developer`ToPackedArray[ϵij00[2]];

(* Calculates the transformation strain constants that will appear in the interfacial energy
term of the free energy functional *)
C11=Sum[ϵij00var1[[m,n]]*ϵij00var1[[m,n]],{m,2},{n,2}];
C12=Sum[ϵij00var1[[m,n]]*ϵij00var2[[m,n]],{m,2},{n,2}];
C21=Sum[ϵij00var2[[m,n]]*ϵij00var1[[m,n]],{m,2},{n,2}];
C22=Sum[ϵij00var2[[m,n]]*ϵij00var2[[m,n]],{m,2},{n,2}];

(* Defines the transformation fictitious stress *)
σijvar1=Table[Sum[Cijkl[[i,j,k,l]]*ϵij00var1[[k,l]],{k,1,2},{l,1,2}],{i,1,2},{j,1,2}];
σijvar2=Table[Sum[Cijkl[[i,j,k,l]]*ϵij00var2[[k,l]],{k,1,2},{l,1,2}],{i,1,2},{j,1,2}];
σijvar1=Developer`ToPackedArray[σijvar1];
σijvar2=Developer`ToPackedArray[σijvar2];
```

```
(* Defines the stress-free reference state *)
E11=Sum[Cijkl[[i,j,k,l]]*ϵij00var1[[i,j]]*ϵij00var1[[k,l]],{i,1,2},{j,1,2},{k,1,2},{l,1,2}];
E12=Sum[Cijkl[[i,j,k,l]]*ϵij00var1[[i,j]]*ϵij00var2[[k,l]],{i,1,2},{j,1,2},{k,1,2},{l,1,2}];
E21=Sum[Cijkl[[i,j,k,l]]*ϵij00var2[[i,j]]*ϵij00var1[[k,l]],{i,1,2},{j,1,2},{k,1,2},{l,1,2}];
E22=Sum[Cijkl[[i,j,k,l]]*ϵij00var2[[i,j]]*ϵij00var2[[k,l]],{i,1,2},{j,1,2},{k,1,2},{l,1,2}];

(* Defines the typical strain energy, Eel0, for nondimensionalizing; in this case the
Variant 1 stress-free transformation strain is used, but Variant 2 could be used as well *)
Eel0=Sum[Cijkl[[i,j,k,l]]*ϵij00[1][[i,j]]*ϵij00[1][[k,l]],{i,1,2},{j,1,2},{k,1,2},{l,1,2}];

(* Determines deltaf (driving force of the martensite transformation) based on Eel0 and ζ
*)
deltaf=Eel0/ζ;

(* Nondimensionalizes the stress-free reference state *)
E11star=E11/Eel0;
E12star=E12/Eel0;
E21star=E21/Eel0;
E22star=E22/Eel0;

(* Defines the function to calculate the matrix, Bpq, to be used in the heterogeneous
relaxation of displacements term in the free energy functional *)
Bpq[p_,q_]:=
  Which[
    p==1&&q==1,
Table[Sum[evectors[[x,y,i]]*σijvar1[[i,j]]*Ωij[[x,y,j,k]]*σijvar1[[k,l]]*evectors[[x,y,l]],
{i,2},{j,2},{k,2},{l,2}],{x,nx},{y,ny}],
    p==1&&q==2,
Table[Sum[evectors[[x,y,i]]*σijvar1[[i,j]]*Ωij[[x,y,j,k]]*σijvar2[[k,l]]*evectors[[x,y,l]],
{i,2},{j,2},{k,2},{l,2}],{x,nx},{y,ny}],
```

```
   p==2&&q==1,
Table[Sum[evectors[[x,y,i]]*σijvar2[[i,j]]*Ωij[[x,y,j,k]]*σijvar1[[k,l]]*evectors[[x,y,l]],
{i,2},{j,2},{k,2},{l,2}],{x,nx},{y,ny}],
   p==2&&q==2,
Table[Sum[evectors[[x,y,i]]*σijvar2[[i,j]]*Ωij[[x,y,j,k]]*σijvar2[[k,l]]*evectors[[x,y,l]],
{i,2},{j,2},{k,2},{l,2}],{x,nx},{y,ny}]
   ]

(* Creates matrices of the Bpq interactions for all pairwise variant combinations *)
Timing[
 B11=Bpq[1,1];
 B12=Bpq[1,2];
 B21=Bpq[2,1];
 B22=Bpq[2,2];
 ]

(* Nondimensionalizes the Bpq terms *)
B11star=Developer`ToPackedArray[B11/Eel0];
B12star=Developer`ToPackedArray[B12/Eel0];
B21star=Developer`ToPackedArray[B21/Eel0];
B22star=Developer`ToPackedArray[B22/Eel0];

(* Plots the B11 interaction matrix *)
ListDensityPlot[RotateRight[B11star,{nx/2,ny/2}],Mesh→False,Frame→False];

(* Defines functions for Fast Fourier Transform (fft) and Inverse Fast Fourier Transform
(invfft) *)
fft=Fourier[#,FourierParameters->{0,-1}]&;
invfft=Re[InverseFourier[#,FourierParameters->{0,-1}]]&;
```

Numerical method to run martensite evolution without magnetic terms

```
(* Runs program; this program uses the 1st order finite difference numerical method *)
time1= Timing[
    t = 0;
    iterations=Floor[totaltime/dt];

    (* Determines total energy of the initial configuration, and starts a list (Elist) of the
energy data to be appended at each ChkPct *)

    Elist=h[];
    s1fourier=fft[s1];
    s2fourier=fft[s2];
    s1avg=Re[s1fourier[[1,1]]/nx];
    s2avg=Re[s2fourier[[1,1]]/nx];
    s1volpercent=s1avg*100;
    s2volpercent=s2avg*100;

    (* Etotalstar expression was taken from Artemev, Jin, and Khachaturyan, Acta Mat.,
49, 1165-1177 (2001) *)
Etotalstar=(Echemmatrix=V*ϕ/2*invfft[ksquared*(s1fourier+s2fourier)]+V*fa[s1,s2])+(
Eelasticmatrix=V/2*(s1avg^2+s2avg^2)-
V/2*(E11star*s1avg^2+E12star*s1avg*s2avg+E21star*s2avg*s1avg+E22star*s2avg^2)-
1/(2*V)*(invfft[B11star*s1fourier*Map[Conjugate[#1]&,s1fourier]]+invfft[B12star*s1fo
urier*Map[Conjugate[#1]&,s2fourier]]+invfft[B21star*s2fourier*Map[Conjugate[#1]&,s
1fourier]]+invfft[B22star*s2fourier*Map[Conjugate[#1]&,s2fourier]]));
    Estar=Total[Etotalstar,2]/V;
    Echem=Total[Echemmatrix,2]/V;
    Eelastic=Total[Eelasticmatrix,2]/V;
    Elist=h[{t,Estar,Echem,Eelastic,s1volpercent,s2volpercent},Elist];

    (* Prints pertinent info of initial configuration *)
    Print["Initial Configuration, Simulation time: ", t ] ;
```

```
Print["Initial Configuration Martensite Energy: ", Estar ] ;
Print["s1 vol percent = ",s1volpercent ,"%"];
Print["s2 vol percent = ",s2volpercent, "%"];

(* Generates a plot of the initial configuration *)
min1=Min[s1];
max1=Max[s1];
denom1=max1-min1;
min2=Min[s2];
max2=Max[s2];
denom2=max2-min2;

(* Creates a list of RGBColor commands with the scaled values for Variant 1 and
Variant 2,  appearing in the first and second position in the RGBColor command *)
CombinedVariants =Reverse[ Table[RGBColor[
      (s1[[i,j]]-min1)/denom1,
      (s2[[i,j]]-min2)/denom2,
      0],{i,1,nx},{j,1,ny}]];
cubelist=Flatten[Table[{CombinedVariants[[j,i]],Rectangle[{i-1,j-
1},{i,j}]},{i,nx},{j,ny}]];
martplot2d=Show[Graphics[cubelist],AspectRatio→1];

Do[{  (* loop to print and save data to file at intermediate steps *)

   Do[{     (* loop for numerical method *)

      s1fourier=fft[s1];
      s2fourier=fft[s2];

      s1plus1=
```

```
        s1+dt*(-ϕ*invfft[ksquared*(C11*s1fourier+C12*s2fourier)]-dfads[s1,s2]-
ζ*(E11star*s1+E12star*s2)+ζ*(E11star*Re[s1fourier[[1,1]]/nx]+E12star*Re[s2fourier[[1
,1]]]/nx)+ζ*invfft[B11star*s1fourier+B12star*s2fourier]);

        s2plus1=
          s2+dt*(-ϕ*invfft[ksquared*(C21*s1fourier+C22*s2fourier)]-dfads[s2,s1]-
ζ*(E21star*s1+E22star*s2)+ζ*(E21star*Re[s1fourier[[1,1]]/nx]+E22star*Re[s2fourier[[1
,1]]/nx])+ζ*invfft[B21star*s1fourier+B22star*s2fourier]);

        s1=s1plus1+RandomArray[ndist,{nx,ny}];
        s2=s2plus1+RandomArray[ndist,{nx,ny}];

        t=t+dt;
        },
       {i, Floor[ChkPct/100*iterations]}
       ];  (* end of loop for numerical method *)

     (* Creates intermediate data files at intervals selected by value of ChkPct, and
calculates intermediate energy and plots *)
      {
       (* append execution time and simulation time to
          the output filename prefix *)
       (* COMMENTED OUT HERE UNTIL YOU ARE READY TO SAVE TO DISK
            outfile = StringJoin[{outprefix,startTime,"_",ToString[t],"s"}];
        Save[outfile,t,dt,Elist,s1,s2];
        *)

      (* Determines total energy of the current configuration, and appends the energy
data to Elist *)
       s1fourier=fft[s1];
       s2fourier=fft[s2];
```

```
s1avg=Re[s1fourier[[1,1]]/nx];
s2avg=Re[s2fourier[[1,1]]/nx];
s1volpercent=s1avg*100;
s2volpercent=s2avg*100;
Etotalstar=(Echemmatrix=V*ϕ/2*invfft[ksquared*(s1fourier+s2fourier)]+V*fa[s1,s2])+(
Eelasticmatrix=V/2*(s1avg^2+s2avg^2)-
V/2*(E11star*s1avg^2+E12star*s1avg*s2avg+E21star*s2avg*s1avg+E22star*s2avg^2)-
1/(2*V)*(invfft[B11star*s1fourier*Map[Conjugate[#1]&,s1fourier]]+invfft[B12star*s1fo
urier*Map[Conjugate[#1]&,s2fourier]]+invfft[B21star*s2fourier*Map[Conjugate[#1]&,s
1fourier]]+invfft[B22star*s2fourier*Map[Conjugate[#1]&,s2fourier]]));
Estar=Total[Etotalstar,2]/V;
Echem=Total[Echemmatrix,2]/V;
Eelastic=Total[Eelasticmatrix,2]/V;
Elist=h[{t,Estar,Echem,Eelastic,s1volpercent,s2volpercent},Elist];

(* Prints pertinent info of current configuration *)
Print[(j)*ChkPct," Percent Complete,   Simulation time: ", t ] ;
Print["Current Configuration Martensite Energy: ", Estar ] ;
Print["s1 vol percent = ",s1volpercent ,"%"];
Print["s2 vol percent = ",s2volpercent, "%"];

(* Generates a plot of the current configuration *)
min1=Min[s1];
max1=Max[s1](*1.2*);
denom1=max1-min1;
min2=Min[s2];
max2=Max[s2](*1.2*);
denom2=max2-min2;

(* Creates a list of RGBColor commands with the scaled values for Variant 1 and
Variant 2,  appearing in the first and second position in the RGBColor command *)
```

```
        CombinedVariants = Reverse[Table[RGBColor[
              (s1[[i,j]]-min1)/denom1,
              (s2[[i,j]]-min2)/denom2,
              0],{i,1,nx},{j,1,ny}]];
        cubelist=Flatten[Table[{CombinedVariants[[j,i]],Rectangle[{i-1,j-
1},{i,j}]},{i,nx},{j,ny}]];
        martplot2d=Show[Graphics[cubelist],AspectRatio→1];
         };
       },{j, Floor[100/ChkPct]}]; (* end of Do loop to print and save intermediate steps *)
    ]; (* end of Timing function *)
```

Numerical method to run coupled magnetic and martensitic domain evolution

```
(* Runs program; this program uses the 1st order finite difference numerical method *)
time1= Timing[
   t = 0;
   iterations=Floor[totaltime/dt];

   (* Determines total energy of the initial configuration, and starts a list (Elist) of the
energy data to be appended at each ChkPct *)
   Elist=h[];
   s1fourier=fft[s1];
   s2fourier=fft[s2];
   s1avg=Re[s1fourier[[1,1]]/nx];
   s2avg=Re[s2fourier[[1,1]]/nx];
   s1volpercent=s1avg*100;
   s2volpercent=s2avg*100;
   (* Etotalstar expression was taken from Artemev, Jin, and Khachaturyan, Acta Mat.,
49, 1165-1177 (2001) *)
Etotalstar=(Echemmatrix=V*ϕ/2*invfft[ksquared*(s1fourier+s2fourier)]+V*fa[s1,s2])+(
Eelasticmatrix=V/2*(s1avg^2+s2avg^2)-
V/2*(E11star*s1avg^2+E12star*s1avg*s2avg+E21star*s2avg*s1avg+E22star*s2avg^2)-
```

```
1/(2*V)*(invfft[B11star*s1fourier*Map[Conjugate[#1]&,s1fourier]]+invfft[B12star*s1fo
urier*Map[Conjugate[#1]&,s2fourier]]+invfft[B21star*s2fourier*Map[Conjugate[#1]&,s
1fourier]]+invfft[B22star*s2fourier*Map[Conjugate[#1]&,s2fourier]]));
   Estar=Total[Etotalstar,2]/V;
   Echem=Total[Echemmatrix,2]/V;
   Eelastic=Total[Eelasticmatrix,2]/V;
   Elist=h[{t,Estar,Echem,Eelastic,s1volpercent,s2volpercent},Elist];

   (* Prints pertinent info of initial configuration *)
   Print["Initial Configuration, Simulation time: ", t ] ;
   Print["Initial Configuration Martensite Energy: ", Estar ] ;
   Print["s1 vol percent = ",s1volpercent ,"%"];
   Print["s2 vol percent = ",s2volpercent, "%"];

   (* Generates a plot of the initial configuration *)
   min1=Min[s1];
   max1=Max[s1](*1.2*);
   denom1=max1-min1;
   min2=Min[s2];
   max2=Max[s2](*1.2*);
   denom2=max2-min2;
   (* Creates a list of RGBColor commands with the scaled values for Variant 1 and
Variant 2,  appearing in the first and second position in the RGBColor command *)
   CombinedVariants =Reverse[ Table[RGBColor[
         (s1[[i,j]]-min1)/denom1,
         (s2[[i,j]]-min2)/denom2,
         0],{i,1,nx},{j,1,ny}]];
   cubelist=Flatten[Table[{CombinedVariants[[j,i]],Rectangle[{i-1,j-
1},{i,j}]},{i,nx},{j,ny}]];

   (* display and save initial magnetic configuration and total magnetic energy*)
```

```
   Emaglist=h[];
   fourierm1=fft[m1];
   fourierm2=fft[m2];
   Etotalmag=Kstaraus*m1^2*m2^2+Kstarmart*(1-
(m1^2*s1^2+m2^2*s2^2))+invfft[Betastaraus*ksquared*(fourierm1+fourierm2)]+invfft[
(e1*fourierm1+e2*fourierm2)^2]-1/(3*nx*ny)-
1/(2*3.14159)*(hextaus[[1]]*m1+hextaus[[2]]*m2);
   Emag=Total[Etotalmag,2];
   Emaglist=h[{t,Emag},Emaglist];

   Print["Initial Configuration, Magnetic Energy: ", Emag] ;
   Print["M magnitude = ", Norm[{Total[m1,2],Total[m2,2]}]] ;

mplot2d=ListPlotVectorField[Table[normm[[i,j]],{i,1,nx,2},{j,1,ny,2}],ScaleFunction→(
1.2&),DisplayFunction→Identity];
   microstructure=pics[];
   microstructure=pics[
      {mplot2d},
      microstructure];
   martplot2d=Show[Graphics[cubelist],AspectRatio→1,DisplayFunction→Identity];
   mtmag=Show[GraphicsArray[{martplot2d,mplot2d}]];

   Do[{  (* loop to print and save data to file at intermediate steps *)

      Do[{     (* loop for numerical method *)

         (*martensite evolution*)
         s1fourier=fft[s1];
         s2fourier=fft[s2];

         s1plus1=
```

```
        s1+dt*(2*Kstarmart*m1^2*s1-
ϕ*invfft[ksquared*(C11*s1fourier+C12*s2fourier)]-dfads[s1,s2]-
ζ*(E11star*s1+E12star*s2)+ζ*(E11star*Re[s1fourier[[1,1]]/nx]+E12star*Re[s2fourier[[1
,1]]]/nx)+ζ*invfft[B11star*s1fourier+B12star*s2fourier]);

      s2plus1=
        s2+dt*(2*Kstarmart*m2^2*s2-
ϕ*invfft[ksquared*(C21*s1fourier+C22*s2fourier)]-dfads[s2,s1]-
ζ*(E21star*s1+E22star*s2)+ζ*(E21star*Re[s1fourier[[1,1]]/nx]+E22star*Re[s2fourier[[1
,1]]/nx])+ζ*invfft[B21star*s1fourier+B22star*s2fourier]);

      s1=s1plus1+RandomArray[ndist,{nx,ny}];
      s2=s2plus1+RandomArray[ndist,{nx,ny}];

      (*magnetic domain evolution*)
      fourierm1=fft[m1];
      fourierm2=fft[m2];

      heff1=2*Kstarmart*s1^2*m1-
invfft[Betastarmart*ksquared*fourierm1]+2*invfft[(e1*fourierm1+e2*fourierm2)*e1]+h
extmart[[1]];
      heff2=2*Kstarmart*s2^2*m2-
invfft[Betastarmart*ksquared*fourierm2]+2*invfft[(e1*fourierm1+e2*fourierm2)*e2]+h
extmart[[2]];

      m1plus1=
        m1-dt*(heff2*m1*m2-heff1*m2^2);

      m2plus1=
        m2-dt*(heff1*m1*m2-heff2*m1^2);
```

```
    normm=MapThread[{#1,#2}/Norm[{#1,#2}]&,{m1plus1,m2plus1},2];

    m1=normm[[All,All,1]];
    m2=normm[[All,All,2]];

    t=t+dt;
    },
   {i, Floor[ChkPct/100*iterations]}
   ];  (* end of loop for numerical method *)

  (* Creates intermediate data files at intervals selected by value of ChkPct, and
calculates intermediate energy and plots *)
  {
   (* append execution time and simulation time to
      the output filename prefix *)
   (* COMMENTED OUT HERE UNTIL YOU ARE READY TO SAVE TO DISK
       outfile = StringJoin[{outprefix,startTime,"_",ToString[t],"s"}];
    Save[outfile,t,dt,Elist,s1,s2];
    *)

   (* Determines total energy of the current configuration, and appends the energy
data to Elist *)
    s1fourier=fft[s1];
    s2fourier=fft[s2];
    s1avg=Re[s1fourier[[1,1]]/nx];
    s2avg=Re[s2fourier[[1,1]]/nx];
    s1volpercent=s1avg*100;
    s2volpercent=s2avg*100;
Etotalstar=(Echemmatrix=V*ϕ/2*invfft[ksquared*(s1fourier+s2fourier)]+V*fa[s1,s2])+(
Eelasticmatrix=V/2*(s1avg^2+s2avg^2)-
V/2*(E11star*s1avg^2+E12star*s1avg*s2avg+E21star*s2avg*s1avg+E22star*s2avg^2)-
```

```
1/(2*V)*(invfft[B11star*s1fourier*Map[Conjugate[#1]&,s1fourier]]+invfft[B12star*s1fo
urier*Map[Conjugate[#1]&,s2fourier]]+invfft[B21star*s2fourier*Map[Conjugate[#1]&,s
1fourier]]+invfft[B22star*s2fourier*Map[Conjugate[#1]&,s2fourier]]));
        Estar=Total[Etotalstar,2]/V;
        Echem=Total[Echemmatrix,2]/V;
        Eelastic=Total[Eelasticmatrix,2]/V;
        Elist=h[{t,Estar,Echem,Eelastic,s1volpercent,s2volpercent},Elist];

        (* Prints pertinent info of current configuration *)
        Print[(j)*ChkPct," Percent Complete,   Simulation time: ", t ] ;
        Print["Current Configuration Martensite Energy: ", Estar ] ;
        Print["s1 vol percent = ",s1volpercent ,"%"];
        Print["s2 vol percent = ",s2volpercent, "%"];

        (* Generates a plot of the current configuration *)
        min1=Min[s1];
        max1=Max[s1](*1.2*);
        denom1=max1-min1;
        min2=Min[s2];
        max2=Max[s2](*1.2*);
        denom2=max2-min2;

        (* Creates a list of RGBColor commands with the scaled values for Variant 1 and
Variant 2,  appearing in the first and second position in the RGBColor command *)
        CombinedVariants = Reverse[Table[RGBColor[
                (s1[[i,j]]-min1)/denom1,
                (s2[[i,j]]-min2)/denom2,
                0],{i,1,nx},{j,1,ny}]];
        cubelist=Flatten[Table[{CombinedVariants[[j,i]],Rectangle[{i-1,j-
1},{i,j}]},{i,nx},{j,ny}]];
```

```
        (*Determines total magnetic energy at the ChkPt and generates a plot*)
        Etotalmag=Kstaraus*m1^2*m2^2+Kstarmart*(1-
(m1^2*s1^2+m2^2*s2^2))+invfft[Betastaraus*ksquared*(fourierm1+fourierm2)]+invfft[
(e1*fourierm1+e2*fourierm2)^2]-1/(3*nx*ny)-
1/(2*3.14159)*(hextaus[[1]]*m1+hextaus[[2]]*m2);
        Emag=Total[Etotalmag,2];
        Emaglist=h[{t,Emag},Emaglist];

        Print[(j)*ChkPct," Percent Complete,   Simulation time: ", t ] ;
        Print["Current Configuration, Magnetic Energy: ", Emag] ;
        Print["M magnitude = ", Norm[{Total[m1,2],Total[m2,2]}]] ;
        (* append execution time and simulation time to
           the output filename prefix *)
        (*COMMENTED OUT UNTIL READY TO SAVE INTERMEDIATE DATA
          outfile = StringJoin[{outprefix,startTime,"_",ToString[t],"s"}];
          Save[outfile,startTime,t, totaltime, dt, iterations,ChkPct,s1,s2];
          *)

mplot2d=ListPlotVectorField[Table[normm[[i,j]],{i,1,nx,2},{j,1,ny,2}],ScaleFunction→(
1.2&),DisplayFunction→Identity];
        microstructure=pics[
           {mplot2d},
           microstructure];
        martplot2d=Show[Graphics[cubelist],AspectRatio→1,DisplayFunction→Identity];
        mtmag=Show[GraphicsArray[{martplot2d,mplot2d}]];

         };

      },{j, Floor[100/ChkPct]}]; (* end of Do loop to print and save intermediate steps *)

   ]; (* end of Timing function *)
```

```
(* Total time to run the simulation *)
time1


(* Gets rid of all the extra brackets in the list of energy data (Elist) that was collected
during the simulation, and plots the Total Energy vs. time *)
Elistfinal=Flatten[Elist]/.h→List;
ListPlot[MapThread[{#1,#2}&,{Elistfinal[[All,1]],Elistfinal[[All,2]]}],PlotRange→{Min
[Elistfinal[[All,2]]],Max[Elistfinal[[All,2]]]},Frame→True,PlotJoined→True,FrameLabel
→{"time","Total Energy"}];
```

Appendix 2: Optical micrographs, differential scanning calorimetry data, and vibrating sample magnetometry data for Ni-Fe-Ga alloys

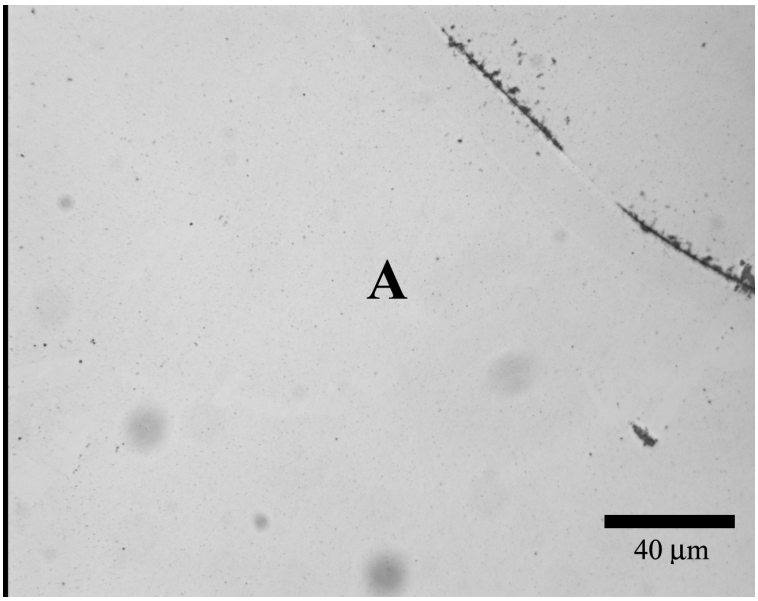

Figure A.1: Optical micrograph of $Ni_{54}Fe_{18}Ga_{28}$ at room temperature. "A" indicates the austenite phase.

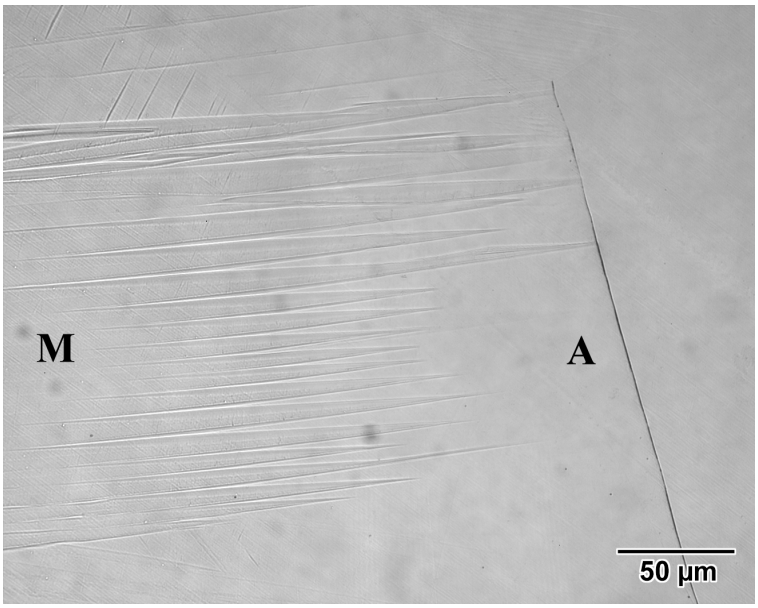

Figure A.2: Optical micrograph of $Ni_{53.5}Fe_{19.5}Ga_{27}$ at room temperature. "A" indicates austenite and "M" indicates martensite.

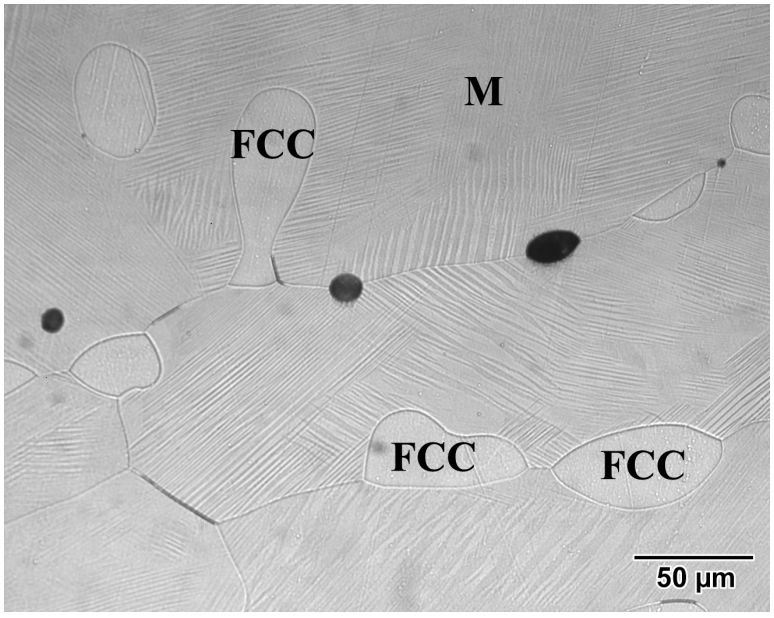

Figure A.3: Optical micrograph of $Ni_{56}Fe_{18}Ga_{26}$ at room temperature. "M" indicates martensite, "FCC" indicates the γ face-centered cubic phase. The black circular regions are pores.

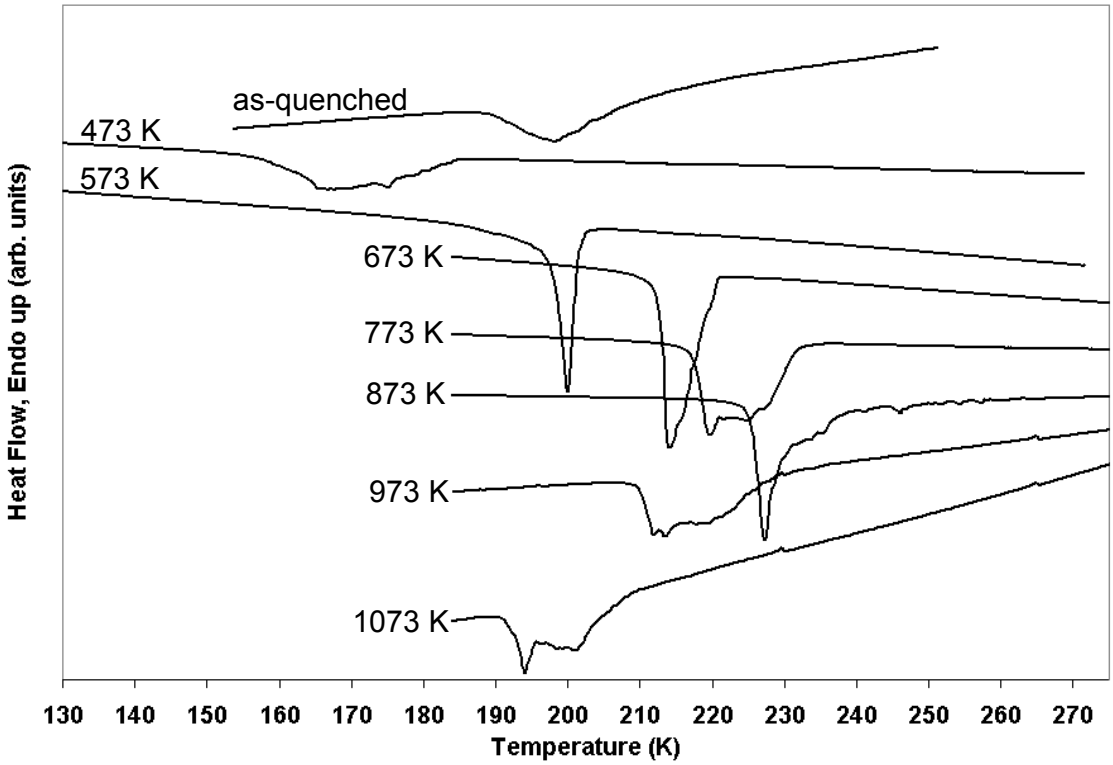

Figure A.4: Differential scanning calorimetry curves on cooling (at 0.167 K/s) for $Ni_{53}Fe_{19}Ga_{28}$ annealed at different temperatures.

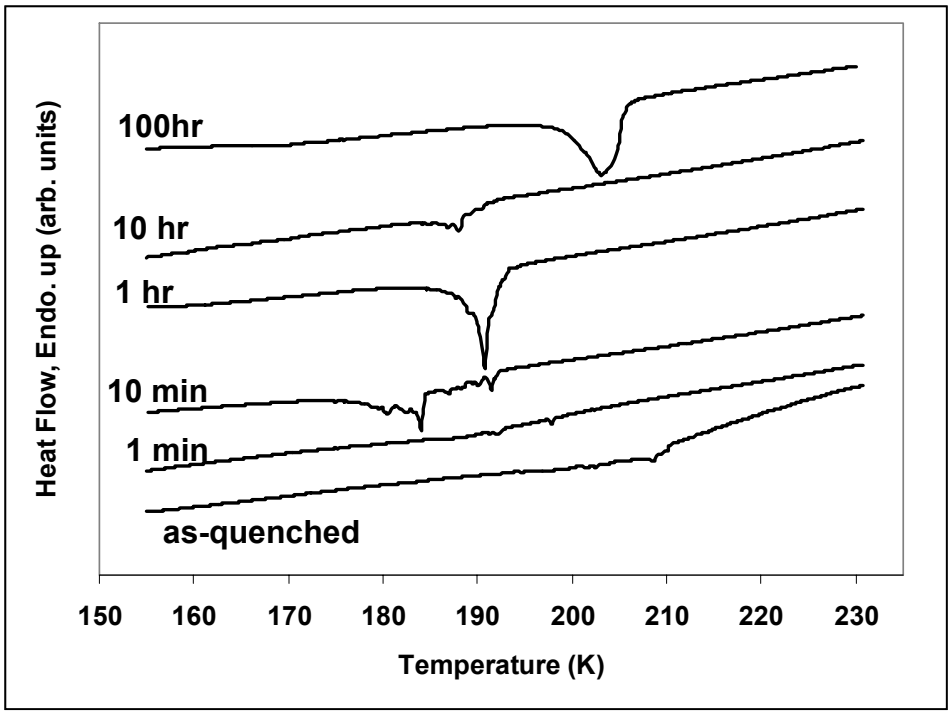

Figure A.5: Differential scanning calorimetry curves on cooling (at 0.167 K/s) for $Ni_{53}Fe_{19}Ga_{28}$ annealed at 573 K for different times.

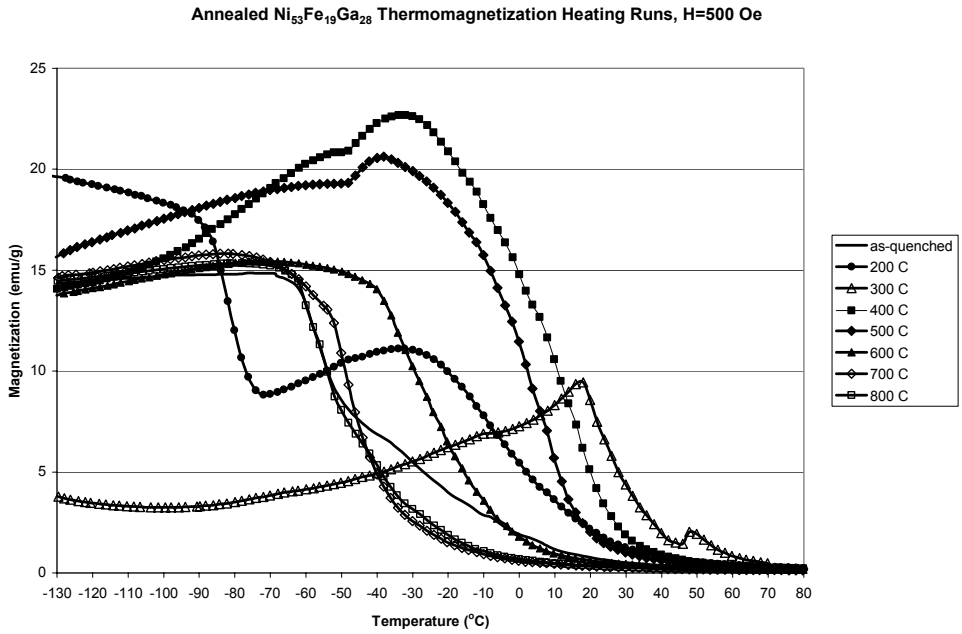

Figure A.6: Thermomagnetization curves during heating (H=500 Oe) for $Ni_{53}Fe_{19}Ga_{28}$ annealed at different temperatures.

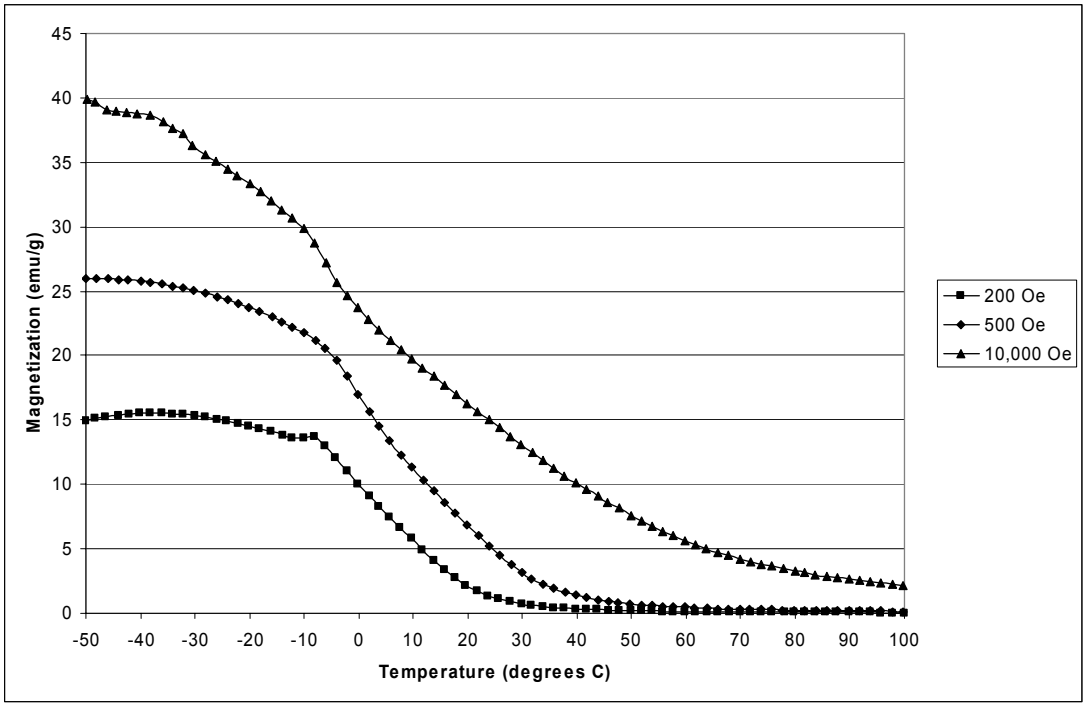

Figure A.7: Thermomagnetization curves during heating for $Ni_{53.5}Fe_{19.5}Ga_{27}$ at applied magnetic fields of H=200 Oe, H=500 Oe, H=10,000 Oe.

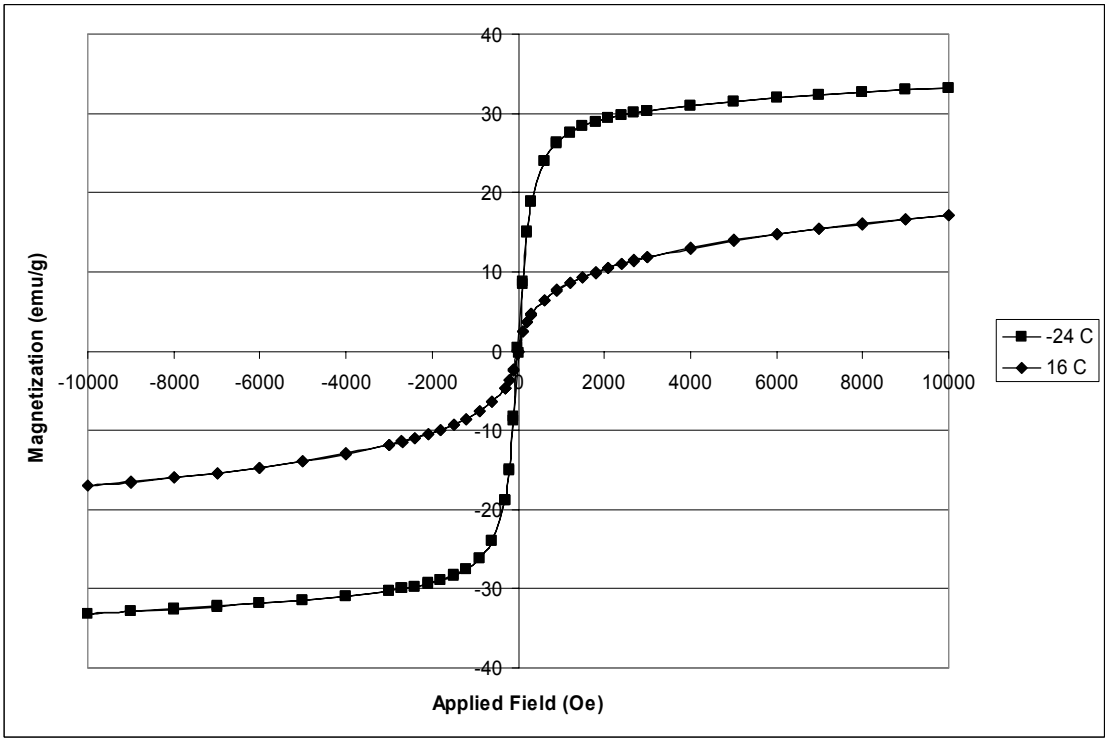

Figure A.8: Hysteresis loops for $Ni_{53.5}Fe_{19.5}Ga_{27}$ at -24ºC and 16ºC.

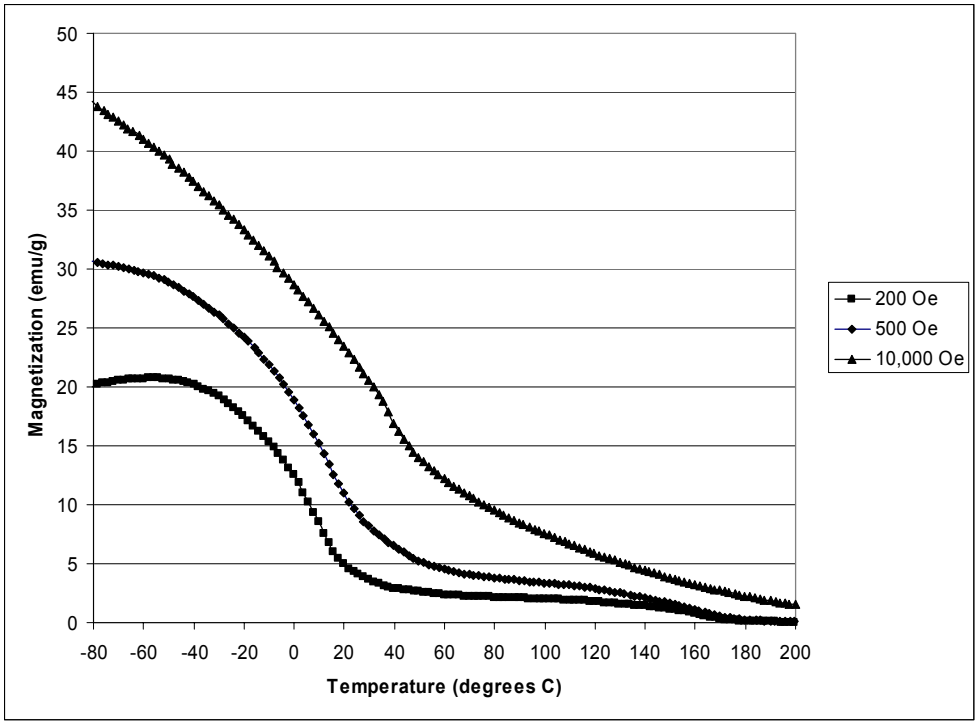

Figure A.9: Thermomagnetization curves during heating for $Ni_{55}Fe_{19}Ga_{26}$ at applied magnetic fields of H=200 Oe, H=500 Oe, H=10,000 Oe.

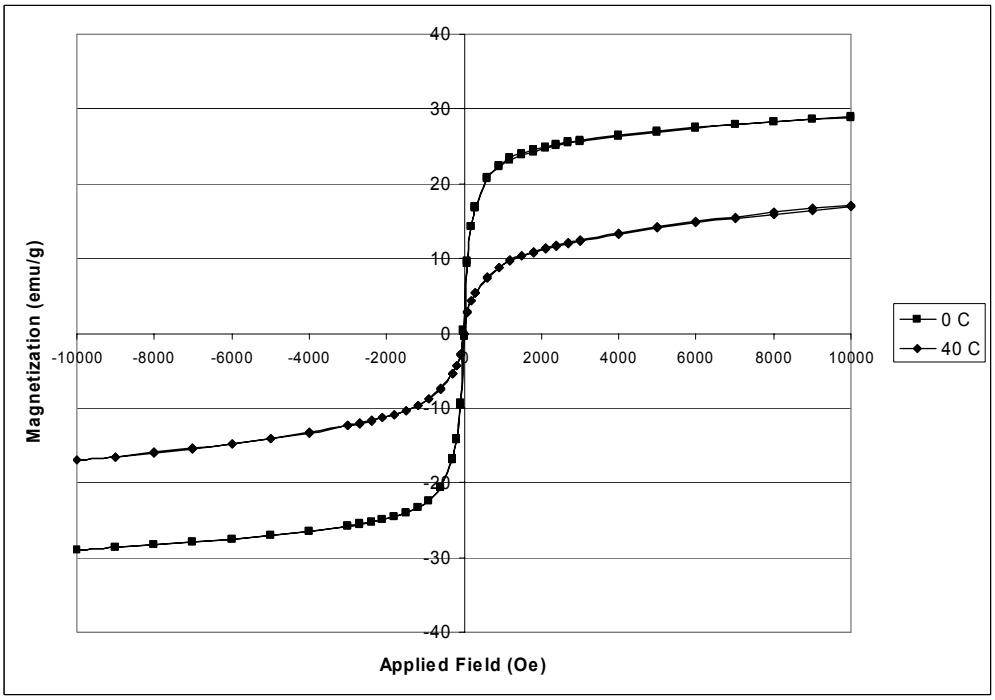

Figure A.10: Hysteresis loops for $Ni_{55}Fe_{19}Ga_{26}$ at 0ºC and 40ºC.

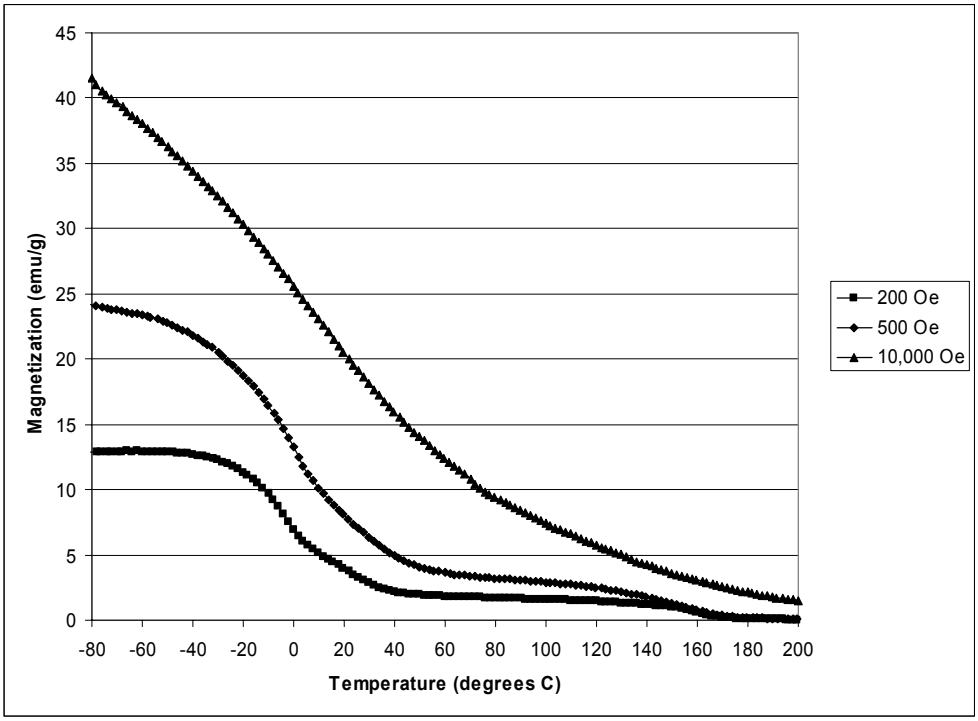

Figure A.11: Thermomagnetization curves during heating for $Ni_{56}Fe_{18}Ga_{26}$ at applied magnetic fields of H=200 Oe, H=500 Oe, H=10,000 Oe.

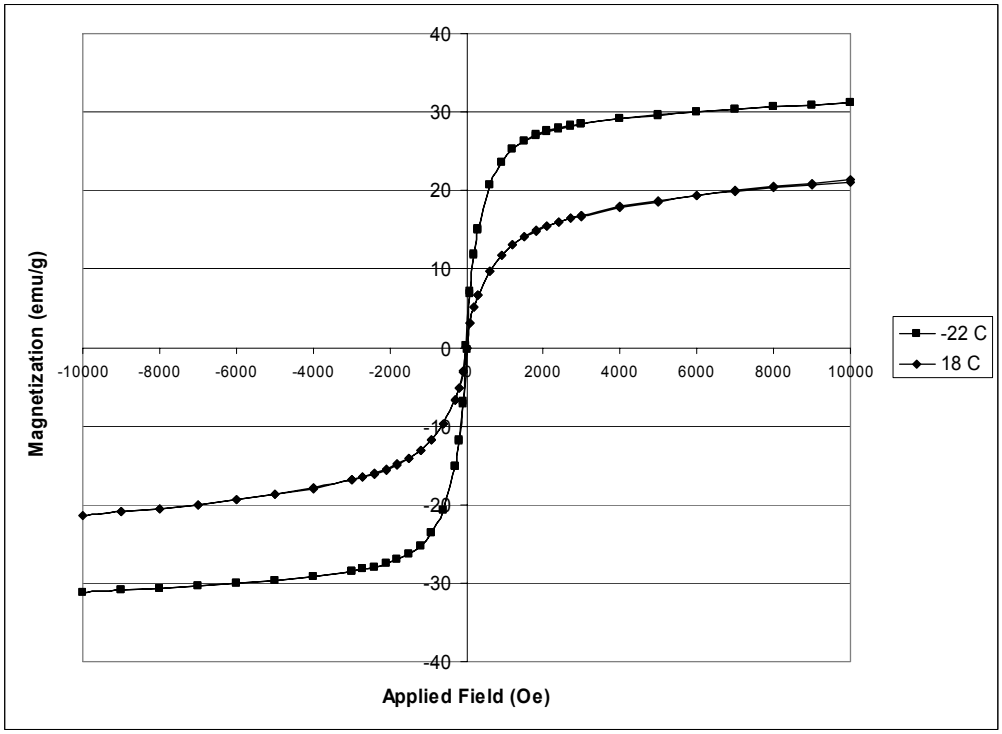

Figure A.12: Hysteresis loops for $Ni_{56}Fe_{18}Ga_{26}$ at -22ºC and 18ºC.

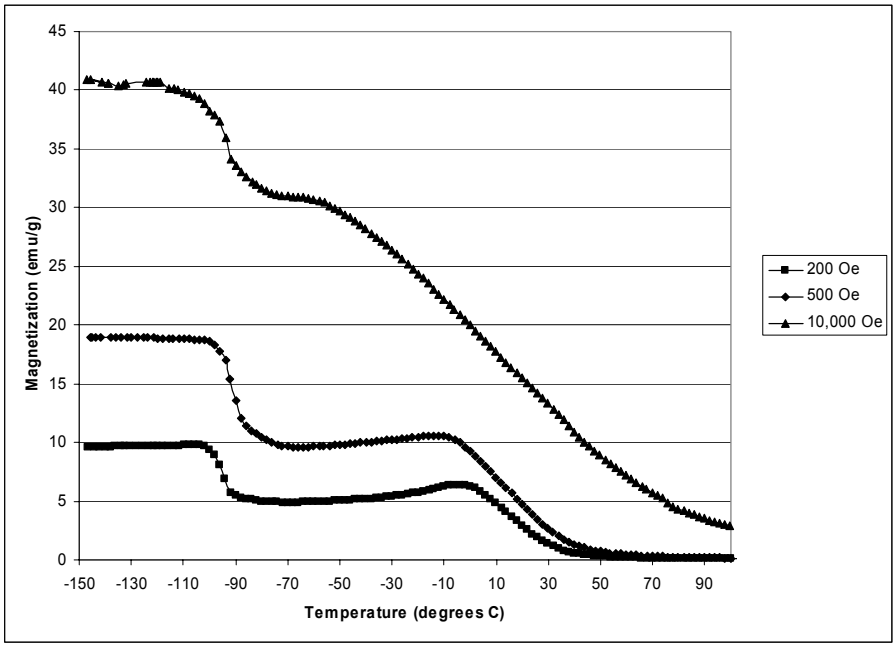

Figure A.13: Thermomagnetization curves during heating for $Ni_{52}Fe_{20}Ga_{28}$ at applied magnetic fields of H=200 Oe, H=500 Oe, H=10,000 Oe.

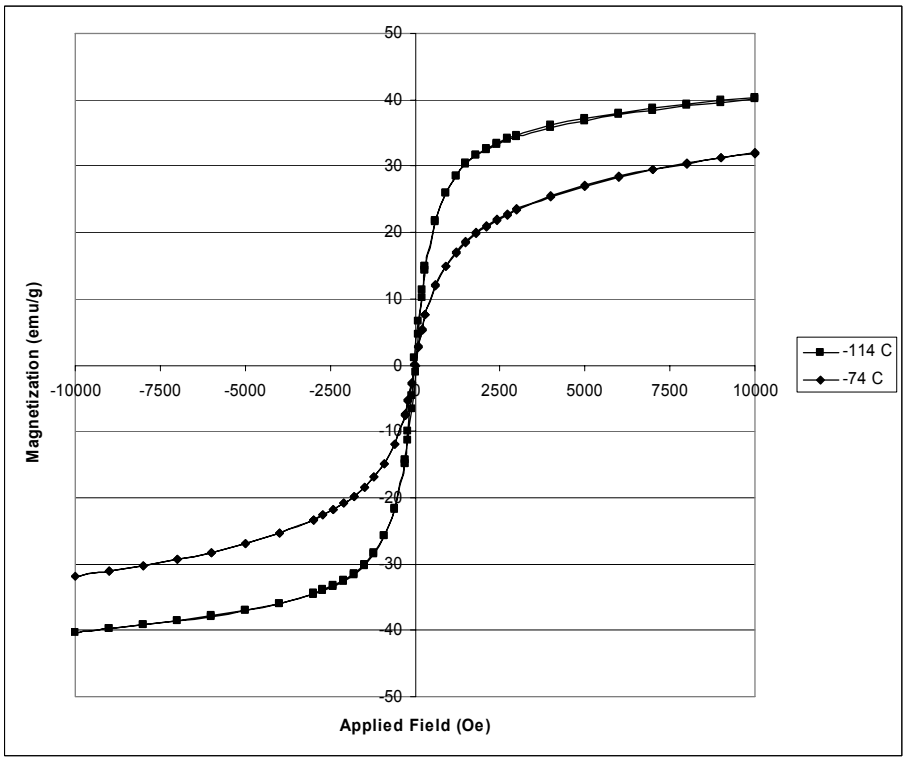

Figure A.14: Hysteresis loops for $Ni_{56}Fe_{18}Ga_{26}$ at -114ºC and -74ºC.

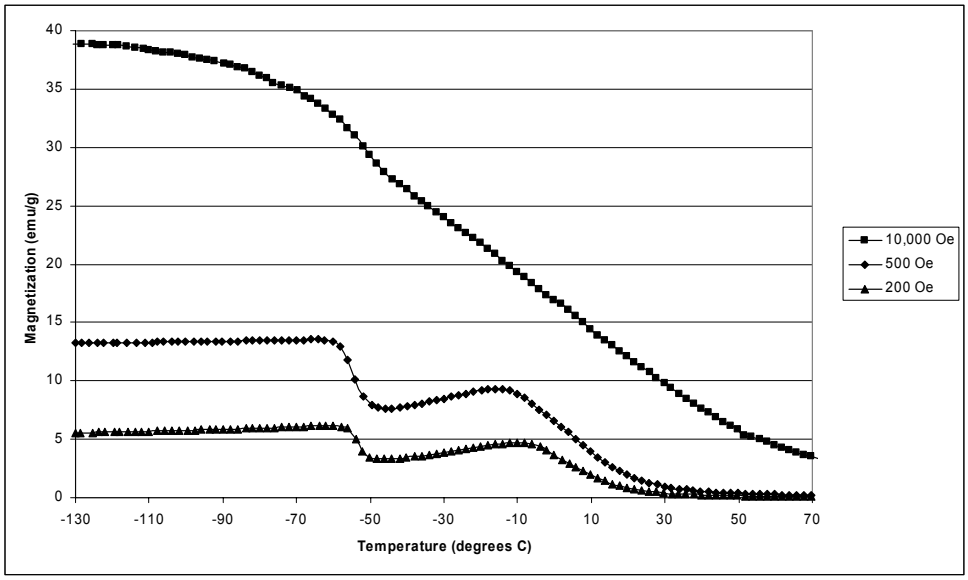

Figure A.15: Thermomagnetization curves during heating for $Ni_{53}Fe_{19}Ga_{28}$ at applied magnetic fields of H=200 Oe, H=500 Oe, H=10,000 Oe.

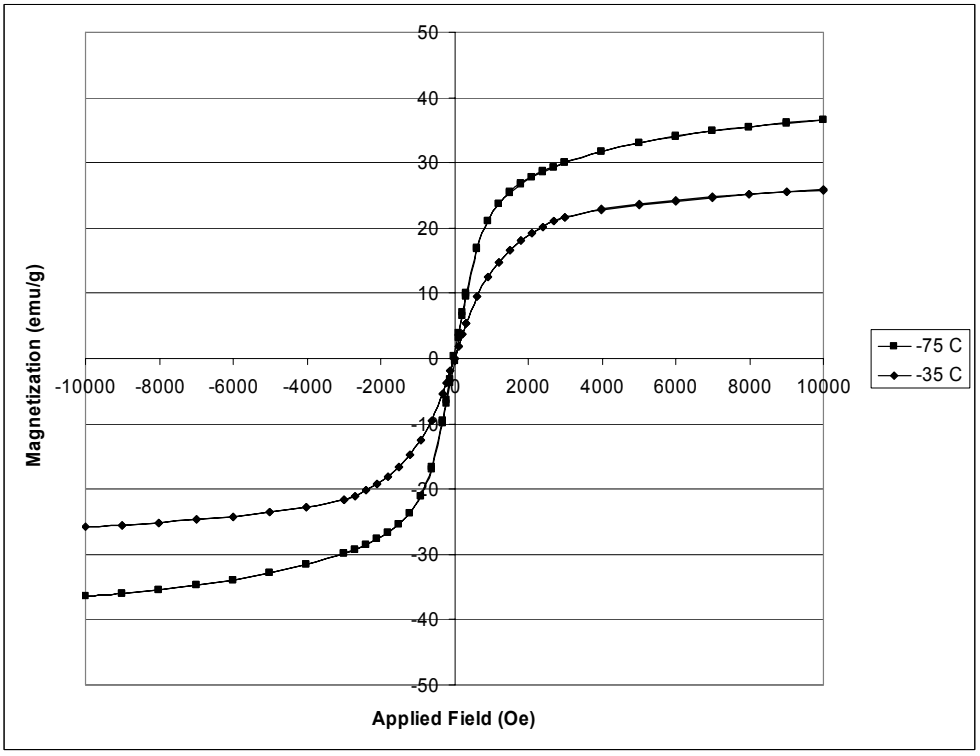

Figure A.16: Hysteresis loops for $Ni_{53}Fe_{19}Ga_{28}$ at -75ºC and -35ºC.

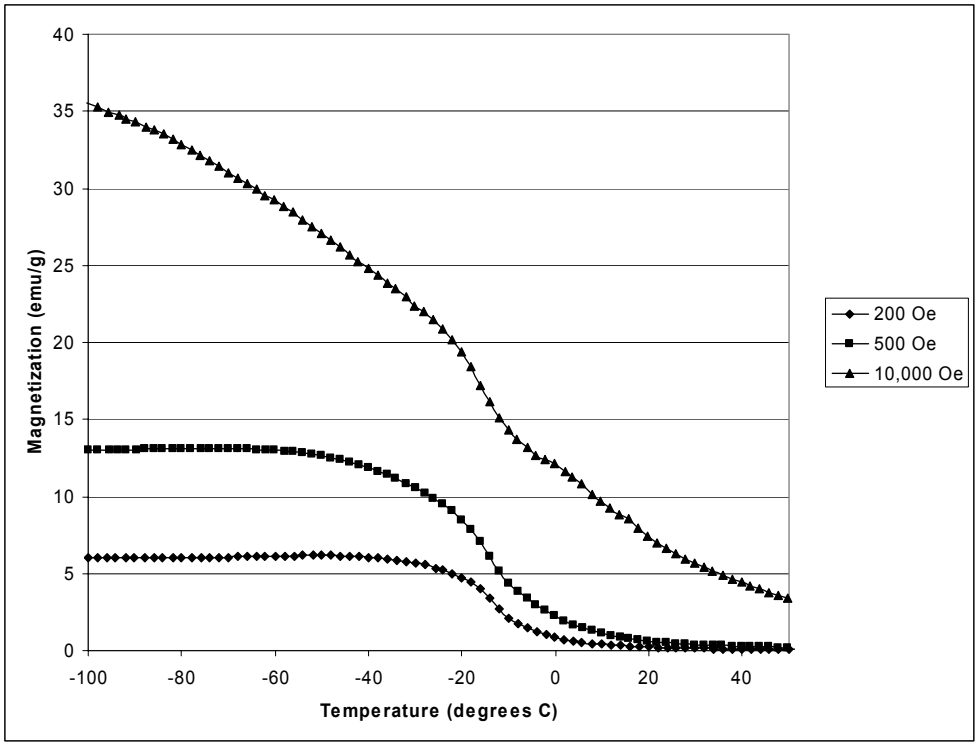

Figure A.17: Thermomagnetization curves during heating for $Ni_{54}Fe_{18}Ga_{28}$ at applied magnetic fields of H=200 Oe, H=500 Oe, H=10,000 Oe.

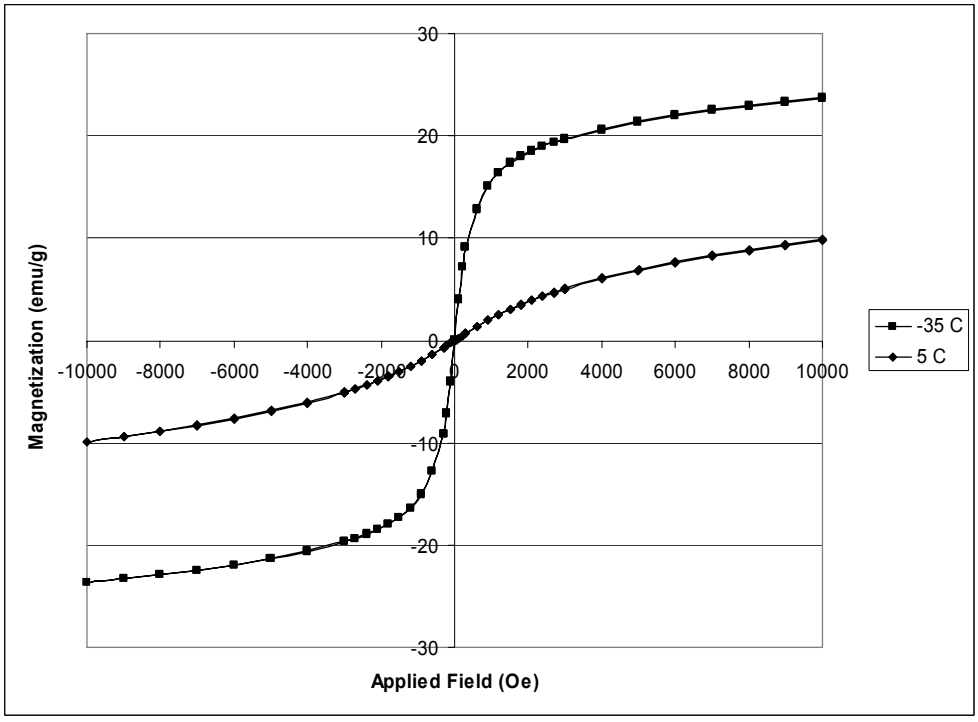

Figure A.18: Hysteresis loops for $Ni_{54}Fe_{18}Ga_{28}$ at -35ºC and 5ºC.

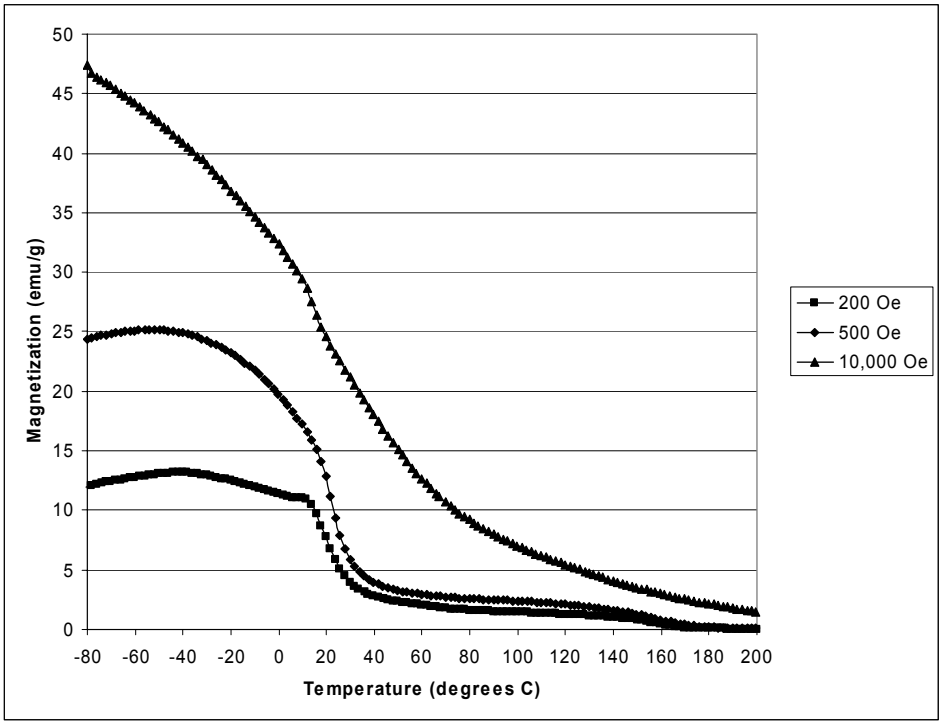

Figure A.19: Thermomagnetization curves during heating for $Ni_{54}Fe_{20}Ga_{26}$ at applied magnetic fields of H=200 Oe, H=500 Oe, H=10,000 Oe.

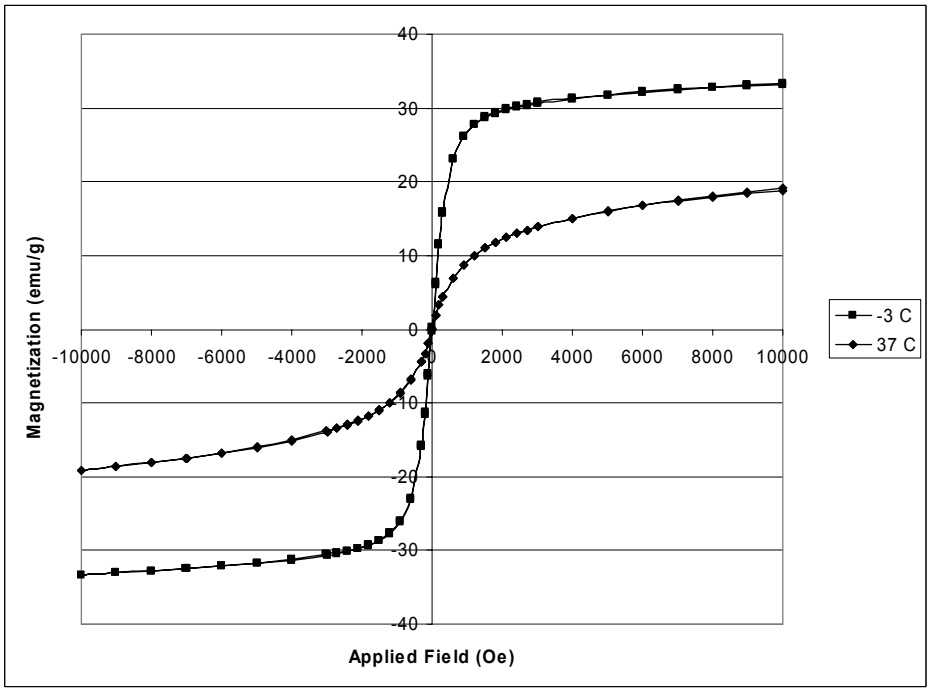

Figure A.20: Hysteresis loops for $Ni_{54}Fe_{20}Ga_{26}$ at -3ºC and 37ºC.

Vita

Todd M. Heil was born in Jarrettsville, Maryland and began his undergraduate studies at Virginia Tech in August, 1996. He graduated with a Bachelor of Science in Materials Science and Engineering in May, 2001. He began his graduate studies in August, 2001 at Virginia Tech, and received a Masters of Engineering in Materials Science and Engineering in May, 2005. After the completion of his doctoral work at Virginia Tech, he will begin postdoctoral research at the Naval Research Laboratory in Washington, D.C. He currently resides with his wife, Tara, in Crofton, Maryland.